

Design and Construction of a Device for Light Scattering Studies on Airborne Particles

Dissertation zur Erlangung des
naturwissenschaftlichen Doktorgrades
der Bayerischen Julius-Maximilians Universität Würzburg

vorgelegt von

Claudiu Dorin Dem

aus Oradea, Rumänien

Würzburg 2003

Eingereicht am:.....
bei der Fakultät für Chemie und Pharmazie

1. Gutachter:.....
2. Gutachter:.....
der Dissertation.

1. Prüfer:.....
2. Prüfer:.....
3. Prüfer:.....
des Öffentlichen Promotionskolloquiums

Tag des Öffentlichen Promotionskolloquiums:.....

Doktorurkunde ausgehändigt am:.....

To my family

Content

Notation

Chapter 1	Introduction	1
1.1.	General introduction and motivation.....	1
1.2.	Goals and structure of the thesis.....	3
Chapter 2	Particle dynamics in air flows and force fields	5
2.1.	Physical parameters of the particle.....	5
2.2.	Basic principles of particle and fluid mechanics: equation of motion for small particles in air flows.....	6
2.3.	Particle, air flows and forced oscillations.....	10
2.3.1.	Particle motion and external forces.....	10
2.3.2.	Flow – induce particle motion and rotation.....	12
Chapter 3	Particle in electric field: charging and containment	13
3.1.	Particle charging mechanisms.....	13
3.2.	Electrical measurement of particle charge.....	17
3.3.	Electrical containment of charged particles.....	20
3.3.1	The electrodynamic balance.....	21
3.3.2	The quadrupole trap.....	24
Chapter 4	Light scattering phenomena	27
4.1.	Elastic light scattering.....	27
4.2.	Inelastic light scattering.....	28
Chapter 5	Design and construction	31
5.1.	Materials and particle generation.....	31
5.2.	Charging devices.....	34
5.2.1.	Diffusion charger.....	34

5.2.2. Field charger.....	39
5.2.3. AC charger: - bidirectional, uni-polar-charging.....	44
5.3. Charged particle containment.....	46
5.3.1. The electrodynamic balance.....	46
5.3.2. Quadrupole system.....	63
Chapter 6 Results and discussion.....	71
6.1. Single particle investigation.....	71
6.2. Many particle investigation.....	77
6.3. Discussion.....	84
Chapter 7 Final discussion and conclusions.....	87
7.1 Summary.....	87
7.2 Zusammenfassung.....	91
Appendix Charging devices.....	95
Trapping systems.....	99
Part_Scan – program.....	105
References.....	133

Notation

Abbreviations

AC	alternating current
CCD	<i>Charge Coupled Device</i>
DC	continuous current
DOP	dioctylphthalate
FT	Fourier Transform
FWHM	Full-width at half-maximum
IR	infrared
MF-F	Monodisperse Fluoreszenzmarkierte Forschungspartikeln
UV	ultraviolet
PMT	Photomultiplier tube
TE	Transverse electric
TEM	Transverse electromagnetic
V	Volts
W	Watts
μm	micrometer, 10^{-6} m

Latin Symbols

			Chapter
a_m	Characteristic number	(-)	5
A	Surface area	(m ²)	
A	System coefficient	(-)	3
$A_{p,z}$	Amplitude of oscillation	(m)	2
A_n	Coefficients	(-)	5
b_m	Characteristic number	(-)	5
\bar{c}_i	Mean speed	(m/s)	3
C	Capacitance	(F)	3
C_C	Cunningham factor	(-)	2,5
C_0, C_1	Balance geometric constant	(-)	5
C_D, K_D	Drag coefficient	(-)	2
d_p	Particle diameter	(m)	2
d_e	Particle equivalent diameter	(m)	2
d_w	Corona wire diameter	(μ m)	3
D	Eddy diffusion coefficient	(m ² /s)	2
D_0	Power density	(W/molecule)	4
e	Unit charge	(C)	3
E	Elliptic integral of the second kind		5
E	Electric field intensity	(V/m)	
E_b	Field strength breakdown	(V/m)	3
E_m	Alternating electric field amplitude	(V/m)	3
f	Frequency	(Hz)	
f_E	AC field frequency	(Hz)	2
$f(\mathbf{q})$	Function of time	(s)	2
F	Force	(N)	
F_D	Drag force	(N)	2
F_e	Electric force	(N)	5
F_G	Body force	(N)	5
$F(t)$	Time-varying function	(s)	2
g	Gravity	(m ² /s)	5
h	Separation between rings	(m)	5
I	Moment of inertia	(kg m)	5

Notation

I_i	Ion current	(A)	5
k	Boltzmann-constant	(J/K)	3
k	Wavenumber	(m^{-1})	4
k_i	Dimensionless parameter	(-)	5
k_1, k_2, k_3	Coefficients	(-)	2
K	Elliptic integral of the first kind		5
K_E	Coulomb constant	($\text{N m}^2/\text{C}^2$)	3
Kn	Knudsen number	(-)	5
l	Length	(m)	5
L	Length scale	(m)	2
L_0	Characteristic length	(m)	2
m_p	Particle mass	(kg)	2
n	Number of elementary charges		3
n_s	Number of elementary charges at saturation		3
N_i	Ions number/concentration	(m^{-3})	3
p	Static pressure	(N/m^2)	2
\bar{p}	Dipole moment	(As/m)	4
$P_{n-\frac{1}{2}}, Q_{n-\frac{1}{2}}$	Legendre functions		5
	even or odd		
r_p	Particle radius	(m)	5
R	Resistance	(Ω)	3
R	Ring radius	(m)	5
q	Charge	(C)	
q	Parameter in Mathieu equation	(-)	5
q_i	Charge of the ring	(C)	5
q_p	Particle charge	(C)	2
q_s	Saturation charge	(C)	3
r	Unit vector, radial coordinate	(m)	4,5
r	Particle displacement	(m)	5
r_i	Radial coordinate of the ring	(m)	5
Re_F	flow Reynolds number	(-)	2
Re_p	particle Reynolds number	(-)	2
t	Time	(s)	
t	Ring thickness	(m)	5
T	Temperature	(K)	3
T	Electric torque	(VC)	5
u	Velocity	(m/s)	2
U	Induced or applied potential	(V)	3
V	Alternating electric potential	(V)	3
V_p	Particle volume	(kg/m^3)	2

Notation

x, y, z	Coordinates	(m)	2,5
Z_i	Ion mobility	(m ² / Vs)	3

Greek Symbols

			Chapter
\mathbf{a}	Polarisability tensor of rank 2	(-)	4
\mathbf{a}_i	parameter used in the charge simulation technique	(m)	5
\mathbf{b}	Polarisability tensor of rank 3	(-)	4
\mathbf{b}_i	parameter used in the charge simulation technique	(m)	5
\mathbf{g}	Polarisability tensor of rank 4	(-)	4
\mathbf{d}	Drag parameter for the bihyperboloidal configuration	(-)	5
∇	Gradient vector	(m ⁻¹)	2
Δ	Difference		
\mathbf{h}_F	Dynamic fluid viscosity	(kg/m/s)	2
l	Gas mean free path	(m)	5
\mathbf{n}_F	Kinematic fluid viscosity	(kg/m/s)	2
l, s, g	Weighting constants	(-)	5
\mathbf{m}	Magnetic permeability	(H/m)	3
q	Dimensionless time		2
q	Spherical coordinate		5
t	Relaxation time	(s)	2,5
t_p	Mechanical relaxation time	(s)	2
Φ	Light flux	(J/s)	4
Φ	Electric potential	(V)	5
Φ_p	Particle phase lag	(°)	2
Ω	Solid angle	(ster)	4
Ω	Rotation	(Hz)	5
\mathbf{r}_F	Fluid density	(kg/m ³)	2
\mathbf{r}_p	Particle density	(kg/m ³)	2
\mathbf{w}	Angular frequency	(Hz)	
\mathbf{w}_B	Frequency in periodic Basset integral	(Hz)	2
\mathbf{w}_E	Angular frequency of the AC field	(Hz)	2
\mathbf{e}	Relative permittivity	(F/m)	3
\mathbf{e}_0	Vacuum permittivity	(F/m)	3
\mathbf{e}_r	Particle permittivity	(F/m)	3

Notation

Ξ	Periodic solutions of the Mathieu eq.	(-)	5
\mathbf{z}_k	Displacement or toroidal coordinates	(m)	4,5
$\mathbf{j}, \Psi, \mathbf{z}_{1,2}$	geometric parameter	(-)	5

Indices

e, E	Electric field
F	Fluid, flow
i	Ion
i, k	Number index
p	particle
x, y, z	Coordinates
\mathbf{q}	Angular, tangential
0	Initial conditions

Chapter 1

Introduction

1.1 General introduction and motivation

Microscopic particles that float in the air are created in many ways through different processes: resuspended soil particles, smoke, photochemically formed particles, atmospheric clouds of water or ice particles. These airborne particles are all examples of aerosols. An aerosol is defined as a collection of solid or liquid particles suspended in a gas and they are usually stable for at least a few seconds. Aerosols are two-phase systems, consisting of the particles and the gas in which they are suspended. Aerosols are one of the types of particulate suspensions listed in Table 1.1 [1]. Correspondingly all systems consist of at least two components having special properties that depend on the size of the particles and concentration in the suspending medium.

The study of aerosols is important for a great number of reasons. It enables us to understand the process of cloud formation in the atmosphere, the production and transport of atmospheric pollutants. It is thought that aerosols do play an important role in global warming [2] which will tend to cool down the Earth – by reflecting the incoming solar radiation and by modifying the cloud properties. Aerosol technology can be found in a lot of applications in the manufacture of spray-dried products, fibre optics, carbon black and the production of pesticides. The toxicity of the inhaled particles depends on the different physical and chemical parameters, an understanding of these

properties is required to evaluate airborne hazards. This knowledge is used in the administration of therapeutic aerosols for the treatment of respiratory and other diseases [1].

Suspending Medium	Type of suspended particles		
	Gas	Liquid	Solid
Gas	-	Fog, mist, spray	Fume, dust
Liquid	Foam	Emulsion	Colloid, slurry
Solid	Sponge	Gel	Alloy

Table 1.1. Several types of particulate suspensions.

The chemical composition of these aerosols indicates environmental impacts [2, 3]. Until recently, the chemical composition of airborne particulate matter was almost exclusively determined from bulk samples. From the point of view of chemical analysis, this is very convenient in that respect that the sample is large enough to develop analytical methods with high sensitivity [4, 5]. The disadvantage of bulk sample characterisation arises from the inability to characterise the particle variations in compositions and the influence of the substrate or wall. Current methods for the chemical investigation of aerosols consist of collecting the particles on a filter and determining the composition of the deposited material. In this case, a period of time elapses between collection and analysis of the aerosols. During this time, transformations can occur so that the investigated material will not correspond to the collected material anymore.

An on-line in-situ system would avoid all these complications by making the chemical characterisation without removing the aerosol from the gas improving also the state-of-the-art in aerosol monitoring [6]. Up to now there does not exist any established technology for on-line, in-situ measurement of the chemical composition of aerosols. This thesis describes the principle and the most important features of a system which allows an on-line measurements of aerosols using Raman spectroscopy as diagnostic technique. Using these results it is possible to design and construct a commercial instrument for on-line aerosol investigation. Applications include experiments with a single particle or with many particles.

1.2 Goals and structure of the thesis

The goal of this work is to monitor and identify aerosol particles. In order to do so two requirements have to be fulfilled:

- The design and construction of a system which allows the investigation of just a single aerosol particle by means of Raman spectroscopy;
- The design and construction of a system for the simultaneous investigation of many particles.

These objectives cannot be achieved without considering some fundamental aspects in particle dynamics in fluids or electric fields, particle charging and particle electrodynamic containment or levitation.

An analysis of the air flow on the particle dynamics is presented in **Chapter 2**. The most important physical parameters for a particle are presented. A review of the particle / air interaction in laminar flows and the response of particles to an imposed flow is given.

Chapter 3 concerns with the particle behaviour under different external conditions (forces) like the influence of an electric field. The presented themes can be divided into two parts: (i) particle charging and (ii) particle levitation.

- In the first part, after a brief introduction, the classical diffusion and field charging theories will be presented. The effect of particles properties on field charging and particle rotation are discussed. Alternative to these mechanisms (regarding the further exposed disadvantages) a method of particle charging in an alternating electric field will be presented. Finally, a method for the measurement of the acquired charge on the particle will be discussed.
- In the second part of Chapter 3 another kind of interaction between the electric field and the charged particle is discussed in order to realise the particle levitation. A short history of the trapping systems is given as well.

The feasibility of using scattered light to investigate the chemical and physical properties of a single levitated particle will be discussed in **Chapter 4**. As an investigation method that provides chemical bond information Raman spectroscopy has

been chosen. Raman spectroscopy is an inelastic light scattering process that is generated by the distortion of the electron clouds of a molecular bond. For the application to single particle studies it has been proved that it is, apart from fluorescence, the only method providing chemical bond information and therefore allows the investigation of chemical reactions.

In **Chapter 5** the instrumental parts are presented in detail. An overview of the materials and particle generation methods used within this thesis are presented. The constructed charging devices are described in detail and compared among each other considering the measured charge of the particles. Different types of axially symmetric electrodynamic balances are studied using analytic and numerical techniques in terms of Mathieu equations. The influence of the gas flow, radiation pressure associated with the laser beam and the modified electric field due to the electrode imperfection is also discussed.

Chapter 6 consists of two parts describing: (i) the system for single particle and (ii) for many particles investigations. The individual devices presented in Chapter 5 have been assembled together. The time diagram and the selection criteria governing the entire process of retaining just one particle from a particle cloud will be presented and discussed. Finally the Raman results are presented for both cases.

The final conclusions of the thesis are given in **Chapter 7**.

Chapter 2

Particle dynamics in air flows and force fields

In this chapter an analysis of the behaviour of particles in an air flow is presented, starting with the simple case of a spherical particle moving in a stagnant flow. The motion of the particle and the assumption regarding the stagnant flow are discussed. The response of a particle to different forces, induced either by the flow or electric fields, is explained. The final goal is to obtain a general equation of motion for the particle considering the influence of the flow and electric fields. The response of particles to externally applied alternating electric fields is also discussed.

2.1 Physical parameters of the particles

Aerosols can be subdivided according to the physical form of the particle and their method of generation. There is no strict scientific classification of aerosols. As mentioned in Chapter 1, aerosols are suspensions of solid or liquid particles in a gas. The term aerosol includes both the particles and the suspending gas, which is usually air.

One of the most important parameters for characterising the behaviour of aerosols is the *particle size*, noted d_p [1]. All properties of aerosols depend on the particle size. An estimation of how the aerosol properties vary with the particle size is

fundamental to understand their properties. Solid particles have normally a complex shape while liquid particles are always nearly spherical.

Another important parameter is the *equivalent diameter* d_e which is the diameter of a sphere that has the same value of a particular physical property as that of an irregular particle (used for solid particles which have usually complex shapes).

In a first approximation, the *shape* can usually be ignored, as it seldom produces more than a twofold change in any properties [2]. Particles with extreme shapes, such as long, thin fibres, are treated as simplified non-spherical shapes with different orientations.

Another physical property of interest is the *particle density* ρ_p , usually expressed in kg/m^3 . Particle densities refer to the mass per unit volume of the particle itself.

The aerosol property mostly measured, and the most important one for health and environmental effects, is the *mass concentration*, the mass of particulate matter in a unit volume of aerosol. Common units are g/m^3 , mg/m^3 and $\mu\text{g/m}^3$. The mass concentration is equivalent to the density of an ensemble of aerosol particles in air.

2.2 Basic principles of particle and fluid mechanics: equation of motion for small particles in air flows

The motion of a discrete spherical particle in a fluid is determined by the interactions between the particle and the flow field. These interactions are governed almost exclusively by the particle inertia. Considering the flow, the Navier-Sokes [1, 4] equation describes the force balance in the flow. For an isothermal, incompressible flow (flow for which $\nabla \cdot \underline{u} = 0$, where \underline{u} is the three-dimensional velocity vector of the fluid at a fixed point in space), the velocity vector \underline{u} is given by:

$$\rho_F \left(\frac{\partial \underline{u}}{\partial t} + \underline{u} \cdot \nabla \underline{u} \right) = -\nabla p + \mathbf{h}_F \nabla^2 \underline{u} + \Sigma \underline{F} \quad (2.1)$$

considering a constant density ρ_F , a dynamic viscosity \mathbf{h}_F , and a linear relation between shear stress and velocity gradient, while p is the static pressure and $\Sigma \underline{F}$ is the sum of external forces [1,2]. The term $\underline{u} \cdot \nabla \underline{u}$ is the inertial acceleration term and it

represents the resistance to flows caused by the inertia of the gas that has to be accelerated around the particle. For a fluid flow with a characteristic length scale L_0 and characteristic velocity u_0 , equation 2.1 can be rewritten as [3]:

$$-\frac{\partial \underline{u}^*}{\partial t^*} = \underline{u}^* \cdot \nabla^* \underline{u}^* - \nabla^* p^* + \frac{1}{\text{Re}_F} \nabla^{*2} \underline{u}^* + \frac{L_0}{\mathbf{r}_F u_0^2} \sum \underline{F} \quad (2.2)$$

with the dimensionless variables

$$\underline{u}^* = \frac{\underline{u}}{u_0} \quad t^* = \frac{t \cdot u_0}{L_0} \quad p^* = \frac{p}{\mathbf{r}_F u_0^2} \quad \nabla^* = L_0 \nabla, \quad (2.3)$$

and the flow Reynolds number Re_F , where the kinematic viscosity \mathbf{n}_F is defined as:

$$\text{Re}_F = \frac{\mathbf{r}_F u_0 L_0}{\mathbf{h}_0} = \frac{u_0 L_0}{\mathbf{n}_F} \quad (2.4)$$

The Reynolds number, Re_F gives the ratio between the inertial and viscous forces in the flow. The inertial effects can be neglected for a small Reynolds number while the viscous flow effects can be neglected when Re_F is very large [4]. In this case a simplified (linear) form of the Navier-Stokes equation is obtained:

$$\nabla p = \mathbf{h}_F \nabla^2 \underline{u}. \quad (2.5)$$

The analytical solutions of this equation, giving the flow field around an assumed spherical particle has been found [4, 5]. For a simplified situation where a single spherical particle of diameter d_p moves with velocity \underline{u}_p into a stagnant flow ($\underline{u}_F = 0$) under negligible inertial forces an equation was derived by Stokes. Thus, when the Reynolds number for the particle:

$$\text{Re}_p = \frac{\mathbf{r}_F d_p \|\underline{u}_F - \underline{u}_p\|}{\mathbf{h}_F} \ll 1 \quad (2.6)$$

the drag force F_D exerted on the sphere by the fluid is given by:

$$F_D = 3\mathbf{p}\mathbf{h}_F \underline{u}_p d_p. \quad (2.7)$$

A more general relation can be found for the drag force considering Bernoulli's equation [4]:

$$F_D = C_D \cdot A_{p,\perp} \cdot \mathbf{r}_F (\underline{u}_F - \underline{u}_p) \cdot \|\underline{u}_F - \underline{u}_p\| \quad (2.8)$$

where $A_{p,\perp}$ is the area of the object perpendicular to the flow and C_D is the drag coefficient which is a function of the Reynolds number, particle shape, and, for a fluid droplet, the particle viscosity. For solid spherical particles the following relationships for expressing C_D as a function of Re_p are widely used [6, 7]:

$$\begin{aligned} C_D &= \frac{24}{Re_p} & Re_p < 0.2 & \quad \text{Stokes,} \\ C_D &= \frac{24}{Re_p} \left(1 + \frac{3}{16 Re_p} \right) & 0.2 < Re_p < 2 & \quad \text{Oseen,} \\ C_D &= \frac{24}{Re_p} \left(1 + \frac{1}{6} Re_p^{2/3} \right) & 2 < Re_p < 800 & \quad \text{Klyachko,} \\ C_D &= 0.44 & 800 < Re_p < 10^5. & \end{aligned} \quad (2.9)$$

The motion of a solid particle in a viscous flow was first derived by Oseen [8], based upon the works of Boussinesq [9] and Basset[10]. Several forms of the equation of motion for a small particle moving in unsteady flows have been studied (Tchen [11], Maxey & Riley [12]). For a spherical particle large enough to neglect the Brownian motion, but small enough to follow every motion of the flow, the motion in an unsteady flow was derived from a force balance where the drag forces consist of Stokes drag, virtual mass effects and a Basset force due to the unsteady flow field. Since in a creeping flow the Navier-Stokes equation is linearised, the forces can be superimposed, yielding the following expressions [3]:

$$m_p \frac{d\underline{u}_p}{dt} = 3\mathbf{p}\mathbf{h}_F d_p (\underline{u}_F - \underline{u}_p) + \frac{1}{2} V_p \mathbf{r}_p \frac{d(\underline{u}_F - \underline{u}_p)}{dt} + \frac{3}{2} d_p^2 \sqrt{\mathbf{p}\mathbf{r}_F \mathbf{h}_F} \int_{t_0}^t \left(\frac{d(\underline{u}_F - \underline{u}_p)}{\sqrt{t - \tau}} \right) d\tau + \Sigma \underline{F} \quad (2.10)$$

$$\frac{d\underline{u}_p}{dt} + k_1 \underline{u}_p = k_1 \underline{u}_F + k_2 \frac{d\underline{u}_F}{dt} + k_3 \int_{t_0}^t \left(\frac{d(\underline{u}_F - \underline{u}_p)}{\sqrt{t - \tau}} \right) d\tau + \frac{\Sigma \underline{F}}{m_p}, \quad (2.10a)$$

for a particle with mass m_p , volume V_p and a non-zero starting velocity starting from $t = t_0$. The coefficients k_1 , k_2 and k_3 are given by:

$$k_1 = \frac{36\mathbf{h}_F}{(2\mathbf{r}_p + \mathbf{r}_F)d_p^2}; \quad k_2 = \frac{3\mathbf{h}_F}{2\mathbf{r}_p + \mathbf{r}_F}; \quad (2.11a, b, c)$$

$$k_3 = \frac{18}{(2\mathbf{r}_p + \mathbf{r}_F)d_p} \sqrt{\frac{\mathbf{r}_F \mathbf{h}_F}{\mathbf{p}}}.$$

The second right-hand term of eqn. 2.10 quantifies the force which accelerates the 'virtual' mass of the particle relative to the surrounding fluid, while the third term is the Basset term which describes the forces arising from deviations of the flow from steady state and the resistance due to acceleration. For the Basset integral term in eqn. 2.10, Tchen [11] assumed a periodic slip velocity $\Delta \underline{u} : \underline{u}_F - \underline{u}_p = \Delta \underline{u} \sin(\mathbf{w}_B t)$ and has shown that the Basset integral, assuming steady state ($t_0 = -\infty$), gives

$$k_3 \int_{t_0}^t \left(\frac{d(\underline{u}_F - \underline{u}_p)}{\sqrt{t - \mathbf{t}}} \right) d\mathbf{t} = k_3 \sqrt{\frac{\mathbf{w}_B t}{2}} \Delta \underline{u} (\cos(\mathbf{w}_B t) + \sin(\mathbf{w}_B t)) \quad (2.12)$$

These results show that the Basset integral is of the order $O(k_3 \sqrt{\mathbf{w}})$ with respect to $\Delta \underline{u}$, which is negligible for small \mathbf{w} values. Considering solid particles in a gas stream, the density ration $\mathbf{r}_p / \mathbf{r}_F$ is generally of the order $O(10^3)$, which allows the assumption that k_2 and k_3 are small compared to k_1 . In this case eqn. 2.10 becomes a first order differential equation:

$$\frac{1}{k_1} \frac{d(\underline{u}_p - \underline{u}_F)}{dt} = \underline{u}_p - \underline{u}_F + \Sigma \underline{F}. \quad (2.13)$$

Eqn. 2.13 indicates that the response of a dispersed particle to a change in the fluid velocity is characterised by a single time constant, $\mathbf{t}_p = 1/k_1$, which is the mechanical relaxation time of the particle. Using this time constant, the motion of a

particle relative to the fluid velocity in which it is dispersed can be analysed. In this work, it was assumed that $k_1 = k_3$ and $k_1 = k_2$, and we considered small values for \mathbf{t}_p , which implies that only Stokes drag forces are present.

2.3 Particle, air flows and forced oscillations

2.3.1 Particle motion and external forces, charged particles in electric fields

The response of a charged particle to an external, time-varying electric field has been studied by Turubarov [7] for $\text{Re}_p \leq 0.2$ and $\text{Re}_p \geq 0.2$. The force balance for the motion \underline{u}_p of a spherical particle with the mass m_p , density \mathbf{r}_p , diameter d_p and charge q_p through a stagnant fluid with the density \mathbf{r}_F , influenced by an external time-varying uniform electric field $F(t)$ with an amplitude \underline{E}_0 , is given by:

$$m_p \frac{d\underline{u}_p}{dt} + \frac{1}{8} C_D \rho d_p^2 \mathbf{r}_F \|\underline{u}_p\| \underline{u}_p = q_p \underline{E}_0 F(t), \quad (2.14)$$

where the drag coefficient C_D (eqn. 2.9) is given as a function of Re_p . Considering an one-dimensional electric field $(0,0,E_z)$ with a frequency $f_E = \omega_E/2\pi$ and $F(t) = \sin(\omega_E t)$ the solution for $u_{p,z}$ for a region where the Stokes law is valid is:

$$u_{p,z} = \frac{q_p E_{0,z} \mathbf{t}_p}{m_p \sqrt{1 + \omega_E^2 \mathbf{t}_p^2}} \cos(\omega_E t - \arctan(\omega_E \mathbf{t}_p)) = A_{u,z} \cos(\omega_E t - \Phi_p), \quad (2.15)$$

where \mathbf{t}_p is the mechanical relaxation time and Φ_p is the phase lag between the driving oscillations and the oscillations of the particle [13, 14]. The amplitude of the oscillatory motion can be obtained by integrating eqn. (2.15):

$$z_p = \frac{q_p E_{0,z} \mathbf{t}_p}{m_p \omega \sqrt{1 + \omega^2 \mathbf{t}_p^2}} \sin(\omega t - \arctan(\omega \mathbf{t}_p)) + z_p(0) = A_{p,z} \sin(\omega t - \Phi_p) + z_p(0). \quad (2.16)$$

The maximum values for the amplitudes are given by $f = \mathbf{w}/2\mathbf{p} = \mathbf{t}_p^{-1}$.

For an arbitrary alternating field with a period T , $F(t) = F(t+T)$, it was shown by Surovtsova [7] that the periodic particle motion in the Stokes region, based on eq. 2.15 is given by:

$$u_{p,z} = \frac{q_p \mathbf{t}_p E_{0,z}}{m_p} f(\mathbf{q}) \quad (2.17)$$

$$\text{where } f(\mathbf{q}) = e^{-q_r} \left(\frac{\int_0^h e^y F(y) dy}{e^{-h} + 1} + \int_0^{q_r} e^y F(y) dy \right), \quad (2.18)$$

$$\text{and } \mathbf{q} = \frac{t}{\mathbf{t}_p}, \quad h = \frac{T}{\mathbf{t}_p}, \quad \mathbf{q}_r = \frac{1}{\mathbf{t}_p} \left(t - T \text{int} \left(\frac{t}{T} \right) \right)$$

For a non-uniform (periodic) electric field ($\nabla E \neq 0$) the velocity $u_{p,z}$ has two components: one is directed along the field lines of the electric field \underline{E} and a second 'drift' velocity directed along $\underline{E} \cdot \nabla \underline{E}$. When $\underline{E} \cdot \nabla \underline{E} \ll \underline{E}$, the Coulomb force acting on the particle, can be approximated for small values of t and by considering $\underline{x} = \underline{u} \cdot t$:

$$\underline{F}_E = q_p \left(\underline{E} + \int_0^x \nabla \underline{E} \cdot d\underline{x} \right) \approx q_p \left(\underline{E} + \int_0^t \underline{u} \cdot \nabla \underline{E} \cdot dt \right). \quad (2.19)$$

If the value $\underline{u}_{p,z}$ for the uniform field is used it was shown [15] that the drift velocity which is the direction of decreasing $\underline{E} \cdot \nabla \underline{E}$ is:

$$\underline{u}_{p,z,drift} = -\frac{q_p^2 \mathbf{t}_p^3}{m_p^2} \cdot \frac{\int_0^h f^2(\mathbf{q}) d\mathbf{q}}{h} \underline{E} \cdot \nabla \underline{E}. \quad (2.20)$$

For a single harmonic function $F(t) = \sin(\mathbf{w}t)$ this drift velocity changes to:

$$\underline{u}_{p,z,drift} = -1/4 \frac{q_p^2 \mathbf{t}_p^2 \underline{E} \cdot \nabla \underline{E}}{m_p^2 (1 + \mathbf{w}^2 \mathbf{t}_p^2)} \quad (2.21)$$

Comparing this equation with eqn. (2.15) one can see that the effect of the non-uniform electric field on the drift velocity is directly related to the ratio $\underline{E}/(\underline{E} \cdot \nabla \underline{E})$.

2.3.2 Flow induced particle motion and external electric fields

If we consider a homogeneous isotropic flow field $\underline{u}_F(x, y, z) = (U_F, u_F', 0, u_F', 0, u_F')$ and an external electric field $\underline{E}(x, t) = (0, 0, E_z(z, t))$, the force equilibrium for a particle in this field yields an expression for the particle motion in z-direction. For a symmetrical AC-field, $E_z(z, t) = E_{0,z}(\sin(\mathbf{w}_E t))$, the motion of the particle perpendicular to the main flow presents an induced dispersion motion and induced oscillation, giving the following expression for $z_p(t)$ [3]:

$$z_p(t) = \sqrt{D_{T,p}t} + A_{p,z} \sin(\mathbf{w}_E t - \Phi_p) + z_p(0). \quad (2.22)$$

For a DC electric field equation (2.22) is reduced to:

$$z_p(t) = \sqrt{D_{T,p}t} + \frac{q_p E_{0,z} t_p}{m_p} \cdot t + z_p(0) \quad (2.23)$$

from which the relative effect on the particle of the externally induced motion can be determined. Thus, the motion of the particle is determined by the electrically induced oscillation if $A_{p,z} \geq \sqrt{D_{T,p} \cdot t}$ (from eq. 2.22) is satisfied. Then, the effect on the particle motion of a DC field will exceed the effect of an AC field if the following condition is fulfilled (see eq. 2.16 and 2.22)

$$t \geq \frac{1}{\mathbf{w}_E \sqrt{1 + \mathbf{w}_E^2 t_p^2}} \approx \frac{1}{\mathbf{w}_E} \quad \text{for} \quad \mathbf{w}_E t_p \ll 1. \quad (2.26)$$

Discussion

The response of a particle dispersed in a flow to an imposed oscillation is determined by the mechanical relaxation time (see eq. 2.13, 2.15) of the particle if the Stokes regime is considered. The disadvantages generated by the presence of flows with high Reynolds numbers can be predicted (eq. 2.5). The particle motion in uniform electric field such as those that are present inside a quadrupole system and a non-uniform field which characterising different electrodynamic balance geometries is analysed. The Coulomb forces dominate over other electrostatic forces if the particle charges are very small and the electric field gradients are large (eq. 2.14, 2.21). The results obtained in different parts of the chapter have been used to design and construct the entire system described in the following.

Chapter 3

Particle in a electric field

In this chapter the charging process of particles by ions of one polarity is discussed. An overview regarding the classical theories of diffusion and field charging mechanisms as well as the corona discharge is presented. Different methods of particle charge measurements are reviewed. Finally, the electrical containment of a charged particle will be described.

3.1 Particle charging mechanisms

In aerosol mechanics, the most important electrostatic effect is the force acting on a charged particle in an electrostatic field. Most aerosol particles carry some electric charge, and some may be even highly charged. For highly charged particles, the electric force can be thousand times greater than the gravitational force. The motion induced by the electrostatic forces forms the basis for important types of air-cleaning equipment, aerosol sampling and measuring instruments.

The most important mechanisms by which aerosol particles acquire charge are *flame charging*, *static electrification*, *diffusion* and *field charging*. The last two charging mechanisms require the presence of unipolar ions, usually produced by corona discharge. These ions are used to produce highly charged aerosols.

Flame charging occurs when particles are formed in/or pass through a flame. At high flame temperatures, direct ionisation of gas molecules creates high concentrations

of positive and negative ions. The net charge acquired by the particles depends on the material and is usually symmetric with respect to the polarity.

Static electrification charges particles by mechanical action as they are separated from the bulk material or other surfaces. This mechanism can produce highly charged particles under the right circumstances, but it is not reliable for aerosol charging because during the contact impurities can stick on to the particle.

Another class of charging mechanisms is represented by the collision processes between the particles and ions, so that ions stick on the particles and therefore charge them. Particles mixed with unipolar ions become charged by random collisions between ions and the particles. This process is called *diffusion charging* because the collisions result from the Brownian motion of the ions and particles. This mechanism does not require an external electric field and, to a first approximation, does not depend on the particle material. As the charge on the particles increases, fewer and fewer ions have sufficient velocity (the velocity follows the Boltzmann distribution) to overcome the repulsive force, and the charging rate slowly approaches zero. An approximate expression for the number of charges $n(t)$ acquired by a particle of a diameter d_p by diffusion charging during the time t is given by [1]:

$$n(t) = \frac{d_p kT}{2K_E e^2} \ln \left[1 + \frac{\rho K_E d_p \bar{c}_i e^2 N_i t}{2kT} \right], \quad (3.1)$$

where \bar{c}_i is the mean velocity of the ions ($\bar{c}_i = 240 \text{ m/s}$ at standard conditions), N_i is the concentration of ions, e is the elementary charge, K_E is the electrostatic constant and T is the temperature. A more accurate, but less convenient expression requiring numerical integration is given by Lawless [15]. A process similar to diffusion charging, but utilizing bipolar ions is used to discharge highly charged aerosols.

Charging by unipolar ions in the presence of a strong electric field is called field charging. The rapid motion of the ions in an electric field results in frequent collisions between ions and particles. When an uncharged particle is placed in a uniform electric field, it distorts the field. The field lines represent the trajectories of the ions. Then, the extent of distortion of the field lines depends on the relative permittivity (dielectric constant) ϵ of the particle material and the acquired charge on the particle (ions in this electric field traveling along the field lines and colliding with the particle where the

lines intersect the particle). In this case diffusion charging can be neglected, the number of charges, n acquired by a particle during a time t in an electric field E with an ion number concentration N_i is given by:

$$n(t) = \left(\frac{3\epsilon}{\epsilon + 2} \right) \left(\frac{Ed_p^2}{4K_E e} \right) \left(\frac{\rho K_E e Z_i N_i t}{1 + \rho K_E e Z_i N_i t} \right), \quad (3.2)$$

where ϵ is the relative permittivity of the particle and Z_i is the mobility of the ions, approximately $0.00015 \text{ m}^2/\text{V} \cdot \text{s}$. In equation (3.2), the first two factors represent the saturation charge n_s reached after a sufficient time for a given charging condition.

$$n_s(t) = \left(\frac{3\epsilon}{\epsilon + 2} \right) \left(\frac{Ed_p^2}{4K_E e} \right). \quad (3.3)$$

The first factor (eqn. 3.3) depends only on the material of the particles and ranges between 1.0 for $\epsilon = 1$ to 3.0 for $\epsilon \rightarrow \infty$. The relative permittivity reflects the strength of the electrostatic field produced in different materials by a fixed potential relative to that produced in vacuum under the same conditions. The second factor indicates that the charge is proportional to the surface area of the particle and to the electric field strength. The final factor is a time-dependent term that reaches a value of 1 when $\rho K_E e Z_i N_i t \gg 1.0$. When particles are intentionally charged by field charging, the ion concentration is usually $10^{13} / \text{m}^3$ or greater, so charging will be 95% in 3 s or less.

Field- and diffusion charging requires high concentrations of unipolar ions. Because of the mutual repulsion and high mobilities of those ions, their lifetimes are short. Consequently, ions must be continuously produced in order to apply these charging methods. Ions can be created in air by radioactive discharge, ultraviolet radiation, flames and corona discharge. Only the *corona discharge* can produce unipolar ions at a high enough concentration useful for aerosol charging. To produce a corona discharge, one must establish a nonuniform electric field, such as that between a needle and a plate or between a concentric wire and a tube. Air and other gases are normally very good insulators, but in a region of sufficiently high field strength, air undergoes an electrical breakdown and becomes conductive. Depending on the geometry of the field, this breakdown can be an arc or a corona discharge. For a wire-and-tube geometry the

only region with sufficient field strength for a breakdown is a thin layer at the surface of the wire. The field strength required for a breakdown depends on the wire diameter d_w and is given by the empirical equation derived by White [16]:

$$E_b = 3000 + 127 \cdot d_w^{-1/2} \text{ kV/m}. \quad (3.4)$$

In the corona region electrons are accelerated to a velocity high enough to remove an electron from an air molecule upon collision and thereby create a positive ion and a free electron. Within the corona region, this process takes place in a self-sustaining avalanche producing a dense cloud of free electrons and positive ions called *corona discharge*. This process is initiated by electrons or ions created by natural radiation.

Positive and negative coronas show quite different properties and appearances. For a positive corona, the entire region around the wire has a stable, glowing sheath with a characteristic bluish-green colour, while for a negative corona, the glow exists in tufts or brushes that appear as a dancing motion having enough energy to produce ozone from oxygen. Gas temperature, pressure and composition affects the corona generation.

The introduction of aerosol particles into the free space between the wire and the tube will result in field charging of the particles having the same polarity as the wire.

There are fundamental limits on the maximum amount of charge that can be acquired by an aerosol particle of a given size. In the presence of strong external fields, aerosol particles can exhibit the corona discharge. The loss of charge by this mechanism sets an upper limit on the charge for a given particle size that is in the order of the magnitude of the corona onset voltage for a sphere of that size. In order to compensate such processes, methods allowing to maximize the charge imparted to the particles and to minimise their losses are still required. One of the methods which could solve this problem is charging the particles in an ionic current and alternating electric field.

Two types of chargers utilizing this concept were proposed in the literature. The idea of an alternating field was proposed by Masuda et al. [17] and theoretically modelled by Zevenhoven [18], while a second type of model using a similar idea was implemented by Jaworek et al. [19]. The ions were emitted by a corona discharge from

needle electrodes, and the electric field was generated by two additional grids. The change of charge imparted to the particle is given by the following differential equation:

$$\frac{\partial q}{\partial t} = \frac{3}{4} \mathbf{p} N(t) \mathbf{m} E(t) d_p^2 \frac{\mathbf{e}_r}{\mathbf{e}_r + 2} \left[1 - \frac{q(t)(\mathbf{e}_r + 2)}{3 \mathbf{p} e_0 E(t) \mathbf{e}_r} \right] \quad (3.5)$$

where the symbols have the same signification as the ones used to explain the other charging methods. The saturation charge of the particle is given by the Pauthenier equation [20, 21]:

$$q_s = 3 \mathbf{p} e_0 d_p^2 E_m \frac{\mathbf{e}_r}{\mathbf{e}_r + 2} \quad (3.6)$$

where E_m is the amplitude of the alternating electric field. The particles flowing through the charger oscillate following the alternating field, and their trajectories depend on the electric field, gravitational force and drag coefficient.

3.2 Electrical measurement of particle charge

Both in fundamental research and in many applications in particle technology scientists have tried to determine simultaneously [22] different particle properties. An overview of possibilities to measure charge and size of particles simultaneously is given by Brown [23]. He concludes that a true separation of various particle properties is often not possible, especially when the measurement method is based on the electric mobility (like for an electric aerosol analyser or the differential mobility analyser DMA) of the particle.

This part presents a measuring technique allowing a non-contact and in situ real time determination of charge and velocity of individual aerosol particles. The simultaneous measurement of dynamic and static particle properties was employed for a deeper understanding of the behaviour of particles in complex force fields [24]. The technique is based on a combination of light scattering, measuring charge induced potentials and time of flight measurements. The particles are aerodynamically focused to pass a first ring electrode, a light scattering volume and a second electrode. The sequence of signals is schematically shown in Fig. 3.1. If a particle carrying a charge q approaches the first ring on the central axis with the velocity v the potential U on the ring rises till it reaches a maximum value of:

$$U_{\max} = A \cdot q \cdot v \quad (3.7)$$

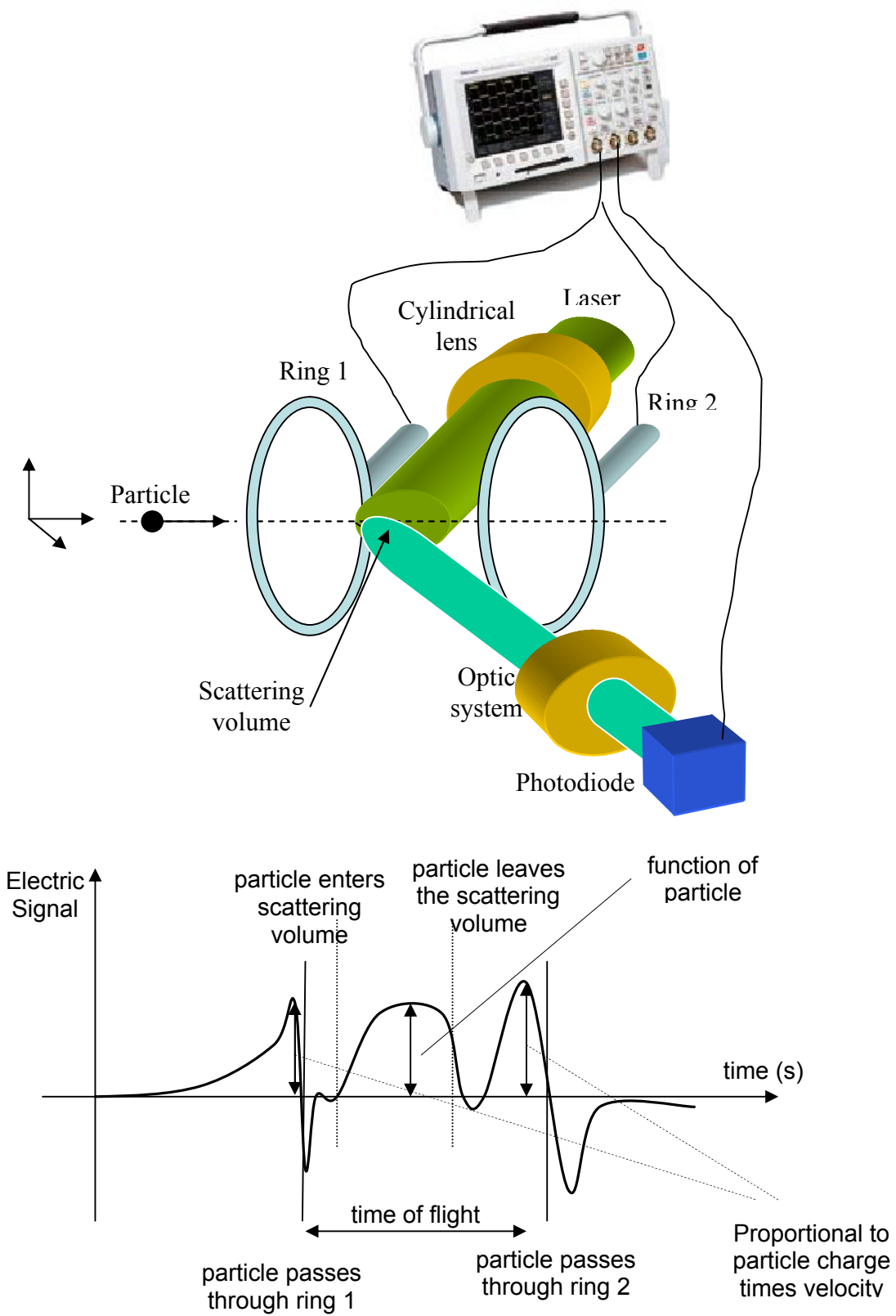


Fig. 3.1. Schematic diagram of the setup (upper part without the detection system) and the pulse sequence (the pulses obtained from rings and photodiode were added together) for a particle passing through the rings (Weber *et al.* [24]).

where A is a coefficient depending on the system parameters such as resistance R and capacitance C of the measuring circuit, the capacitance of the ring C_r and on the ring radius r [25].

This technique has been employed by Vencoulen [26] to measure the charge of individual aerosol particles. For a given set-up A is a constant and the particle charge can be determined from measuring U_{\max} and the particle velocity v , which is determined from the time difference between the ring signals (knowing the separation distance between them).

In between the two electrical signals from the ring electrodes the particle passes through an optically defined light scattering volume. A laser beam focused through a cylindrical lens generates the scattering volume. The scattered light was collected in a 90° degree geometry by an appropriate collection system (formed by two equiconvex lenses) and focused on a photodiode (see Fig. 3.1). The photodiode output and the rings were connected with a two channel oscilloscope (Tektronix TDS 200). A typical signal curve is presented in Fig. 3.2.

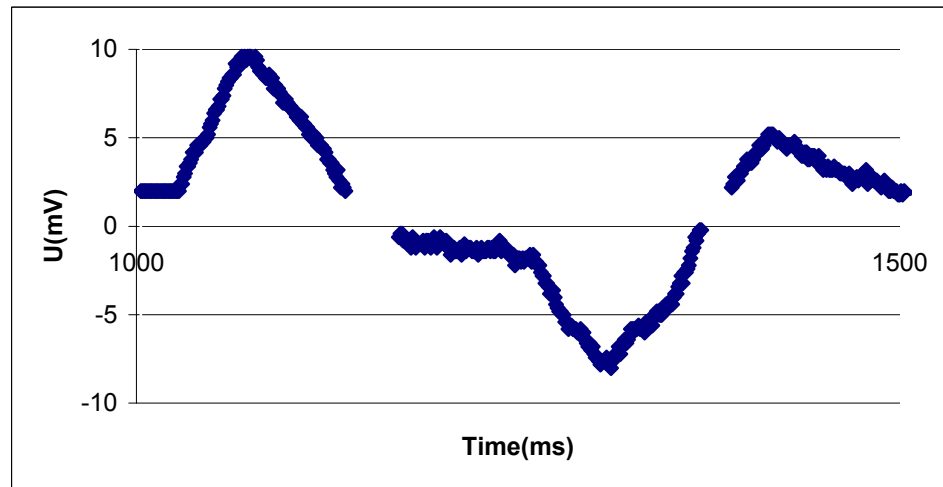


Fig. 3.2. Detected electrical signal profile for the induced potential generated by a particle flow through one ring.

When the particles enter the scattering volume, the signal on the photodiode increases and reaches a constant value giving the total particle cross section for light scattering which can be used to get a light scattering equivalent particle diameter [24]. Only particles creating this signal pattern are accepted for further evaluation, i.e. particles that are not passing through the centre of the rings will not be recorded.

3.3 Electrical containment of charged particles

The levitation of single particles has been accomplished by a variety of techniques but the most pertinent method for this study is the electrodynamic levitation. Electrostatic and electrodynamic levitation applies electric fields to balance vertical forces and require that the particle is charged.

The optical levitation technique has been introduced by Ashkin [28]. He noted that if a high intensity laser beam is operating in the gaussian or TEM_{00} (transverse electric and magnetic) mode, it produces a net force which focuses the particle in the centre of the beam. He trapped latex particles by radiation directed horizontally with either a single beam or two opposite beams. Later, Ashkin and Dziedzic [29] used the TEM_{01} or donut mode of an argon ion laser oriented vertically to trap solid dielectric particles. A review of particle trapping in laser light traps is given by Kiefer [30, 31]. The difficulty in applying optical levitation to this study is twofold. First, the trap does not provide strong radial and axial stability. When a gas flow passes the particle, the imposed drag force will create an imbalance of forces on the particle displacing it from the beam. As mentioned in the previous chapters, a gas flow should bring the particles inside the system. Second, this technique relies on the incident radiation having a gaussian or donut intensity distribution, and small fluctuations in the profile will induce instability. Therefore, optical levitation was not employed.

The development of the electrostatic balance is based on Milikan's classic oil drop experiment in 1910. Milikan measured the electron charge by placing an oil droplet between two charged plates and determining the particle settling's velocity with and without an applied electric field. The DC potential is balancing the vertical forces acting on the particle like gravity and aerodynamic drag. Particles caught in Milikan's electrostatic balance are inherently unstable. Despite this limitation, several research groups have exploited the electrostatic device to investigate evaporation processes [32, 33, 34]. Fletcher [35] recognised these limitations and improved the stability characteristics by inserting a small insulate disk in the top plate of the chamber. When the droplet is drifting off the centre, the two plates are get it grounded and the disk is electrified, restoring the particle to the centre. Then, the electric field was switched on and the droplet is rebalanced. Gucker and Egan [36] were the first which used the Milikan chamber to measure light scattering from aerosol droplets. They incorporated a

rotating photomultiplier tube *PMT* to measure the scattered light as a function of the angle in the horizontal plane of the apparatus (and after that they compared the results with theoretical predictions derived from Mie theory). Wyatt and Philips [37] improved the device presented in reference [36] by incorporation an electro-optical system which provide a better vertical positioning of the particle in the electrodynamic chamber. Davis and Ray [38, 39] measured diffusion coefficients, vapour pressures and Lennard-Jones constants of relatively non-volatile organic aerosols.

The electrostatic balance has been demonstrated to be a useful device. However considering the exposed disadvantages another system, namely the electrodynamic balance is the preferred device for the experiments presented in this work, because it uses electric field gradients to focus a charged particle into the centre of the system.

3.3.1 The electrodynamic balance

The electrodynamic trap superimposes the AC and DC electric fields on the particle to provide radial stability and balance vertical forces. The AC field forms a saddle-shaped potential which provides radial restoring forces, while the DC field balances vertical forces. Paul and Raether [40] were the first that introduced the electrodynamic concept with an electric mass filter. From this point, the evolution of the electrodynamic balance developed along two paths: Paul [41] pursued a radiofrequency quadrupole for trapping small particles such as atomic ions and Wuerker

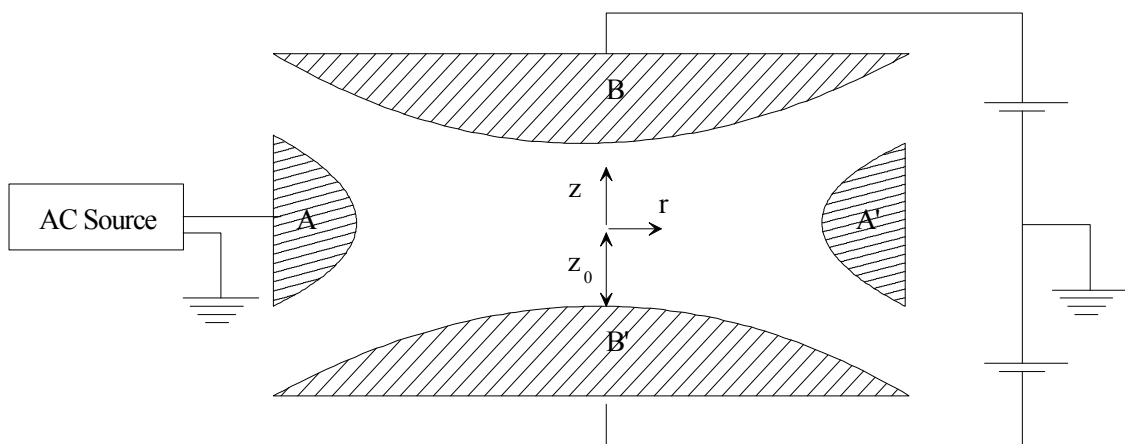


Fig. 3.3. Cross section of the bihyperboloidal electrodynamic balance used by Wuerker *et al.* (A-A' is connected to the AC potential while B and B' are connected to a continuous potential).

et al. [42] introduced a device to investigate micrometer-sized particles. Wuerker used an electrodynamic balance with a hyperboloidal electrode configuration.

A DC field was applied between the top and bottom electrodes and the AC field was applied to the centre electrode. For trapping the particle, the DC field was adjusted so that the particle was focused in the centre of the balance.

Straubel [43 - 46] simplified the electrode geometry by using a washer-type ring geometry. This design limits the ability to perform light scattering measurements, because the ring blocks the scattered light radially.

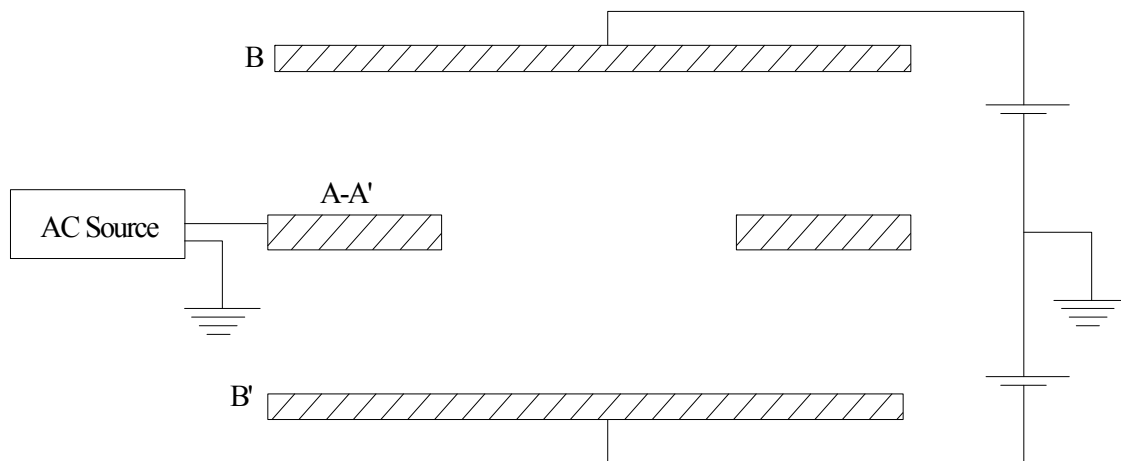


Fig. 3.4. Cross section of the single ring electrodynamic balance configuration used by Straubel *et al.* (A-A', B and B' have the same signification as in the Fig. 3.1).

Berg et al. [47] used a configuration with opposite spherical AC electrodes oriented vertically inside a grounded cylindrical electrode. Richardson and Spann [70] introduced a balance with a cylindrical AC electrode and hemispherical DC endcap electrodes formed from nickel mesh for the investigation of the addition and removal of water vapor from ammonium sulfate droplets.

The bihyperboloidal electrode configuration has been preferred by many investigators for the study of physical and chemical processes of single microparticles. Blau et al. [48] measured light scattering from droplets of dioctylphthalate (DOP), Davis [49] monitored evaporation rates of dibutylsebacate particles and Rubel [50, 51] investigated multicomponent oil droplets. In addition, the electrodynamic balance was used to measure the radioactivity of a single particle by Ward [52]. This geometry allows adequate measurements of strong scattered light. For weakly scattered light

Arnold [53] introduced a spherical void electrodynamic balance (the system presents a large solid angle) which acted as an integrating sphere to obtain an overall scattering efficiency of the particle.

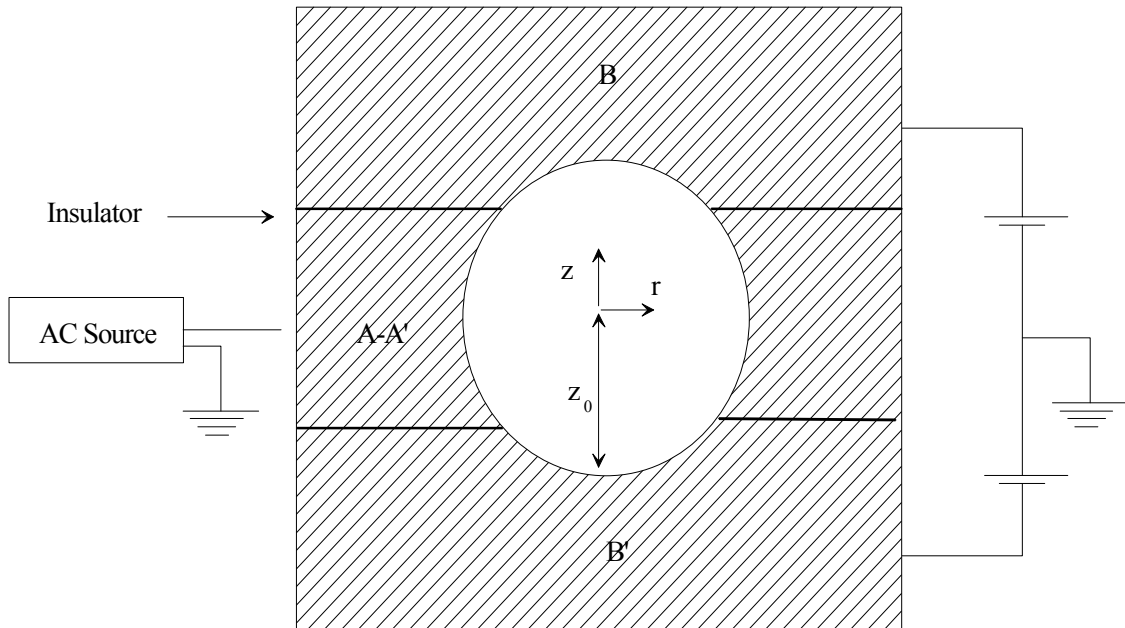


Fig. 3.5. Spherical void electrodynamic balance (Arnold and Folan [53]; A-A', B and B' have the same signification as in the Fig. 3.1).

The inner walls of this cavity are coated with a highly diffuse reflective material, so that the detected light is integrated over 4π steradian solid angle. Recently, Ray [54] used a double ring configuration to investigate the evaporation rate of a coated droplet eliminating the DC endcap electrodes by applying a DC bias voltage to each ring. Starting from this geometry another type of electrodynamic balance – four ring balance – has been developed.

For all the electrodynamic configurations, a particle is focused stable in the center of the trap when all vertical forces are balanced by the DC potential and radial restoring forces are provided by the AC potential. However, there are conditions under which the particle's motion will become unstable and it can be propelled completely out of the trap. The stability is characterized by the magnitude of the AC and DC fields, the frequency of the AC field, the properties and size of the particle and the properties of the surrounding gas. A theoretical description of these electric fields, particle trajectory and the frequency influence on the trapped particle is presented in Chapter 5.

3.3.2 The quadrupole trap

In the previous section the two paths in the development of trapping systems were mentioned, one of them was the quadrupole ion trap system. Its features as a mass filter or as an ion store are well documented in many papers, review articles and books (Dawson [55], March and Hughes [56]).

As a storage device, the ion trap acts as an ‘electric field test tube’ for the confinement of gaseous ions. The confining capacity arises from the formation of a trapping potential well when appropriate potentials are applied to the electrodes of the trap. This confinement permits the investigation of gas-phase chemistry and the elucidation of ion structures. In addition to the confinement of ions, the ion trap can function as a mass spectrometer in that the mass/charge ratios of the confined ion species can be measured. A quadrupole mass filter consists of four parallel metal rods arranged as in the figure below.

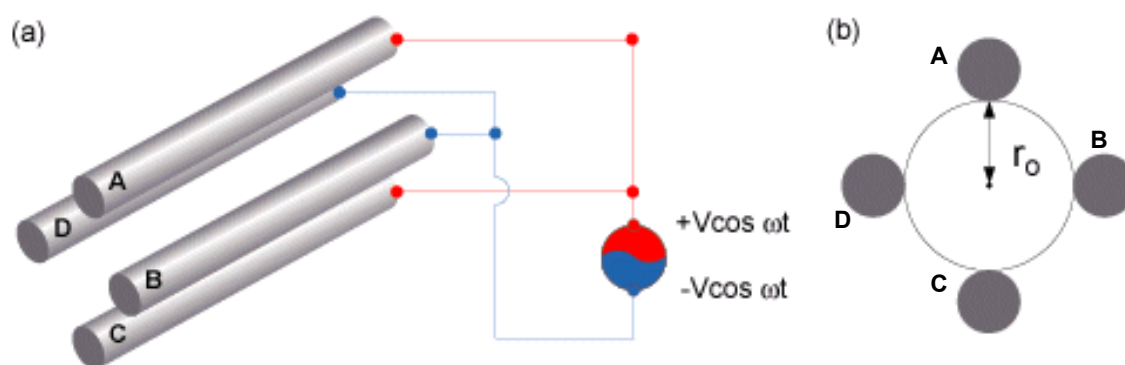


Fig. 3.6. Schematic view of the quadrupole system: (a) the electrical connections; (b) in section.

The two opposite rods have an applied potential of $U + V \cdot \cos(\omega t)$ and the other two rods have a potential $-(U + V \cdot \cos(\omega t))$, where U is a DC potential and $V \cdot \cos(\omega t)$ is an AC potential. The applied voltage affects the trajectory of ions or charged particles travelling down the flight path centred between the four rods. For given DC and AC voltages, only ions of a certain mass-to-charge ratio pass through the quadrupole filter and all other ions are thrown out of their original path. In general, the function principle of the quadrupole mass filter is fully described by the Mathieu equations, their solutions can be classified with the help of the stability diagram. Conditions for obtaining

periodic and stable solutions of the Mathieu equation are well known [57, 58]. The geometry is not restricted to only this four rods, much more complicated geometries like hexa- or octopole can be also used.

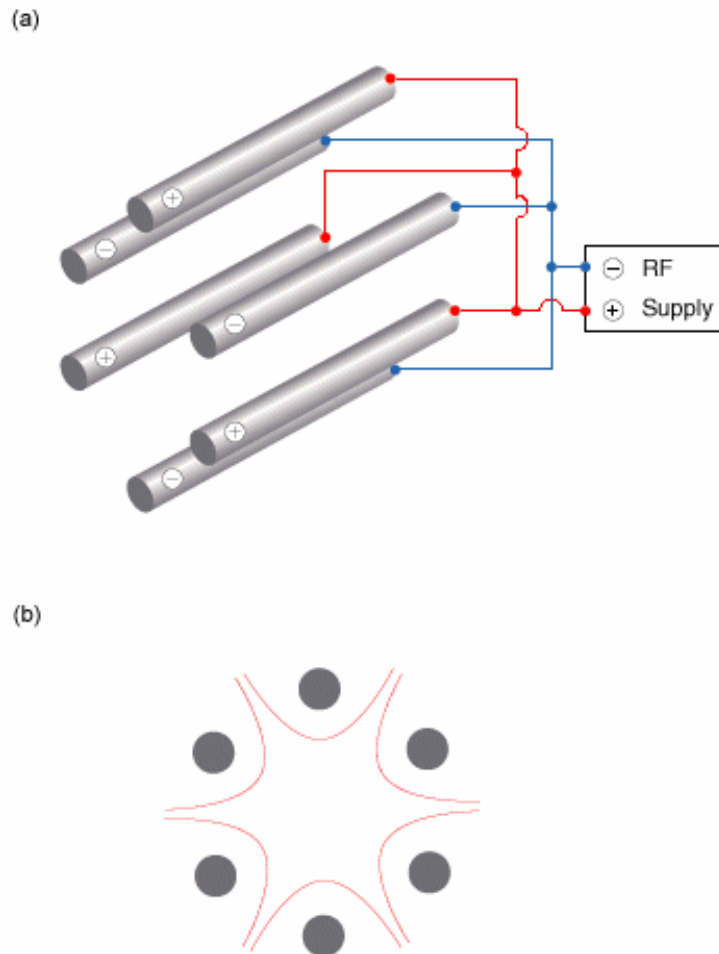


Fig.3.7. Schematic view of the hexapole system: (a) the electrical connections; (b) in section illustrating also the equipotential surfaces..

Discussion

The process of particle charging by ion bombardment of one polarity is discussed. An overview regarding the classical diffusion and field charging mechanisms as well the corona discharge is presented. The concept and the advantages of non-contact particle charge measurements are discussed. Finally, the electrical containment in an electrodynamic balance and quadrupole system of a charged particle is treated.

A more complete theoretical description is presented in Chapter 5.

Chapter 4

Light scattering phenomena

In this chapter the feasibility of using the scattered light to obtain information about the physical parameters and/or about the chemistry of a single levitated particle are discussed. The physical properties can be determined using the elastically scattered light, while Raman spectroscopy is applied to obtain chemical information.

4.1. Elastic light scattering

Chemists, physicists and various engineers utilise light scattering to study a whole range of materials including gases, pure liquids or solutions.

Generally, there are two classes of problems – (i) the direct problem and (ii) the inverse problem: the direct problem is to calculate theoretically or to observe experimentally the scattering by a known, well-defined system; the inverse problem is to characterise the system via a knowledge of the scattering, usually obtained by the experiment.

For a dielectric sphere (ideal model of an aerosol), the absorption and scattering of electromagnetic radiation is described by Maxwell's equations. Particular interesting in characterisation such a sphere is the case when the wavelength of the incident radiation is of the order or smaller than the diameter of the irradiated sphere. Mie [59] investigated this case in an attempt to understand the absorption properties of a gold

suspension in water and he solved the electromagnetic field equations in- and outside the sphere. Several texts describe the Mie theory [60, 61]. Therefore only a summary of the results is provided here. If the wavelength of light is small compared to the diameter of the sphere, the latter can act as a cavity for light to resonate, resulting in a complex scattering pattern. Analysing this scattering pattern according to the Mie theory, the intrinsic physical (size, refractive index) and extrinsic (aerodynamic diameter) parameters of the scattering object can be obtained.

4.2. Inelastic light scattering

The Raman effect was predicted by Smekal [62], and it was experimentally measured by Raman [63] in 1928. Raman [63] and Raman and Krishnan [64] published the discovery of a new type of secondary radiation from liquids and gases. Shortly afterwards, Landsberg and Mandelstam [65] published similar results for quartz crystals. Raman was awarded with the Nobel Prize in 1930 for his discovery and since then there have been numerous treatments of the phenomenon. These texts cover both the classical and quantum mechanical aspects of Raman scattering and only a summary of these results is provided below.

Raman scattering is a phenomenon in which light interacts inelastically with the chemical bonds of the molecule. Raman can be used as vibrational and rotational spectroscopy which differs from other spectroscopic methods like infrared or fluorescence spectroscopy [66, 67, 68]. Raman scattering is unique in that it involves the momentary elastic distortion of the electron cloud of a molecular bond and the spontaneous, incoherent re-emission of radiation upon relaxation. The distorted bond induces temporarily a dipole which dissipates after the molecule returns to its initial state. The ability of the electron clouds to be distorted and to generate an induced dipole is represented by the polarisability. In general, this polarisability depends on how tightly the electrons are bound to the nuclei. In the symmetric stretch the strength of the electron binding is different between the minimum and maximum internuclear distances. Therefore the polarisability changes during the vibration and this vibrational mode scatters Raman light (the vibration is Raman active). In the asymmetric stretch the electrons are more easily polarized in the bond that expands but are less polarized in the bond that compresses. There is no overall change in polarisability and the asymmetric stretch is Raman inactive.

The Raman mechanism is sharply different from that of infrared spectroscopy where the absorption of radiation results in the excitation of the vibrational, rotational and bending modes, generated from a change in the molecule's dipole moment. Therefore, for homogeneous molecules, such as N₂, O₂ or Br₂ there is no possibility for a permanent change in the molecule's dipole moment, and the Raman activity can be observed but not absorption of infrared light.

In the classical treatment, the induced dipole moment \bar{p} , is expressed as a function of the applied field vector by:

$$\bar{p} = \mathbf{a} \cdot \bar{E} + \mathbf{b} \cdot \overline{EE} + \mathbf{g} \cdot \overline{EEE} \quad (4.1)$$

where \mathbf{a} , \mathbf{b} and \mathbf{g} are polarisabilities which are tensors of rank 2, 3 and 4 respectively. Typical values for \mathbf{b} and \mathbf{g} are a factor of 10¹⁰ and 10²⁰ smaller than \mathbf{a} . Thus, for the linear Raman effect, the expression reduces to:

$$\bar{p} = \mathbf{a} \cdot \bar{E} \quad (4.2)$$

where the polarisability tensor can be expressed in a Taylor series with respect to the displacement coordinates, \mathbf{z}_k by

$$\mathbf{a} = \mathbf{a}_0 + \left(\frac{\partial \mathbf{a}}{\partial \mathbf{z}_k} \right) \mathbf{z}_k + \dots \quad (4.3)$$

with the zero description for the equilibrium position of the molecule.

Using the notation of Schweiger [69, 70], the differential light flux, $d\Phi$, radiated per solid angle, $d\Omega$, from an oscillating dipole is given by:

$$\frac{d\Phi}{d\Omega} = \frac{k^4}{2\pi\mathbf{m}_0^{1/2}\mathbf{e}_0^{3/2}} \left[\bar{r}_0 \times (\bar{r}_0 \times \bar{p}) \right]^2 \quad (4.4)$$

where \bar{r}_0 is the unit vector in the direction of observation and \mathbf{m}_0 is the magnetic permeability of the vacuum. This expression can be integrated to yield the ratio of the total scattered light, Φ , to the incident power density per molecule, D_0 . For a cartesian

coordinate system and linear polarised incident radiation, the integrated result of eqn. 4.4 is:

$$\frac{\Phi}{D_0} = \frac{8p}{3} \left[k_0^4 |\mathbf{a}_0|^2 + \frac{1}{4} \sum_i (k_0 \pm k_i)^4 \left| \left(\frac{\partial \mathbf{a}}{\partial \mathbf{z}_i} \right)_0 \right|^2 \right]. \quad (4.5)$$

This equation (4.5) predicts correctly that there is frequency shifted light, emitted during the scattering. The shifted or inelastic scattered contribution is represented by the second term in brackets while the first term is the elastic scattered component. The shifted light is predicted to appear at higher (anti-Stokes Raman) or lower (Stokes Raman) frequencies. Equations (4.4, 4.5) also show that the Raman flux is proportional to the fourth power of the incident frequency. Consequently, it is advantageous to operate at small wavelengths, but not in the region where fluorescence occurs UV domain.

This classical treatment does not give the correct intensities of the shifted Raman light and the temperature dependence of the Raman effect is also not accounted for. Experimentally, the Stokes line is much stronger than the anti-Stokes line and the relative strengths and also the previous mentioned effects, can be better understood by examining a quantum mechanically derived model for the Raman effect [68].

From this short introduction, it can be resumed that laser methods can be applied to analyse the chemical, physical and geometrical properties of very small objects, for example for the investigation of transport and reactive processes in aerosols and sprays.

Chapter 5

Design and construction

In this chapter the process of particle charging by ions of one polarity is discussed. The diffusion, field and alternating electrical field charging devices are presented from the mechanical and electrical point of view. Furthermore, using a similar theoretical description the constructed electrodynamic balances and electric quadrupoles are described. The instrumentation used for the Raman measurements is also described. Finally the advantages and/or disadvantages characteristic for each device are mentioned.

5.1 Materials and particle generation

Materials

All chemicals used within this project were reagent grade materials. As a function of the suspending medium two different classes of materials were used: particles suspended in a liquid or used as powders. The first material class was purchased from Microparticles GmbH. Due to the different polymer composition, the physical and chemical properties are very different and can be adjusted for the desired application. To perform the experiments, the research particles from MF-F (Monodispersen Fluoreszenzmarkierte Forschungspartikel) class with a monodisperse size distribution in diameters ranging from 1 to 10 μm were used.

The powder materials were purchased from Aldrich Chemical Company. These chemicals from Aldrich Chemical Company include: titan dioxide TiO_2 , sodium sulphate Na_2SO_4 , potassium sulphate K_2SO_4 . In chapter 6 another two types of materials were used: (i) an organic polymer which present a banana-shaped structure based on monoaromatic ring (benzen) and (ii) a biological substance – pollen.

Particle generation

An important feature of aerosol study is the production of test aerosols to calibrate the instrument. Standard particles having diameters between $1\mu\text{m}$ and $10\mu\text{m}$ were used considering the physical condition of the suspending medium. For particles suspended in a liquid, a stream of test particles was obtained by atomisation, which is the general name for the process of disintegrating a liquid into airborne droplets [71, 72]. Atomisers are classified by the type of energy used to break up the liquid (pressure, jet and pneumatic). The most common type is the pneumatic atomiser, which uses the energy from compressed air to break up a liquid stream. To generate test particles an atomiser type ATM220 (see A.1a) from Topas GmbH was used [73]. This atomiser works as a two-stream nozzle based on the injection principle and is combined with a baffle placed close to the spray outlet. This section removes coarse spray droplets and leads to a resulting particle size number distribution below $1\mu\text{m}$. The atomiser produces a highly concentrated output aerosol with a high grade of stability and reproducibility. The particle production rate adjustment can be performed by a needle valve at the inlet flow-meter and/or using a diluter (see A.1b).

The most widely used method for generating solid-particle test aerosols is the pneumatic redispersion of dry powders. Particles can be redispersed after settling or aggregation (which is similar to powder) by motion relative to the fluid, which can be caused by oscillation of the container or by a rotating and/or oscillating the stirrer. An overview is given in Ref. [74]. The simple system, feeds loose powder into an air stream by means of gravity, usually assisted by vibrations. These systems give variable aerosol concentrations because of uneven delivery of powder and variations in the bulk density of the powder.

Particle collimator

In order to reduce the particle losses it is necessary to transform the generated particle cloud into a particle stream [75]. Particle beams have been used extensively because they facilitate on-line measurements of the size and chemical composition of individual particles [76, 77]. These particle beams can be generated using different nozzles, aerodynamic lenses or acoustic devices.

To reduce the beam divergence sheath flow has been used to confine the particles close to the axis. After the generation the particles are drawn into the inlet and immediately split into a sample flow, through the inner tube (or nozzle), and a sheath flow, through the outer tube (see Fig. 5.2., Inlet-module). The sheath flow is filtered and confines the sample particles to the centre of the stream (for a better confinement of the particles it was necessary to use a sheath flow 4 or 5 times higher as the sample flow) before bringing them into the charging device.

A second possibility to produce a particle stream takes into account aerodynamic lenses [78] illustrated in Fig. 5.1.

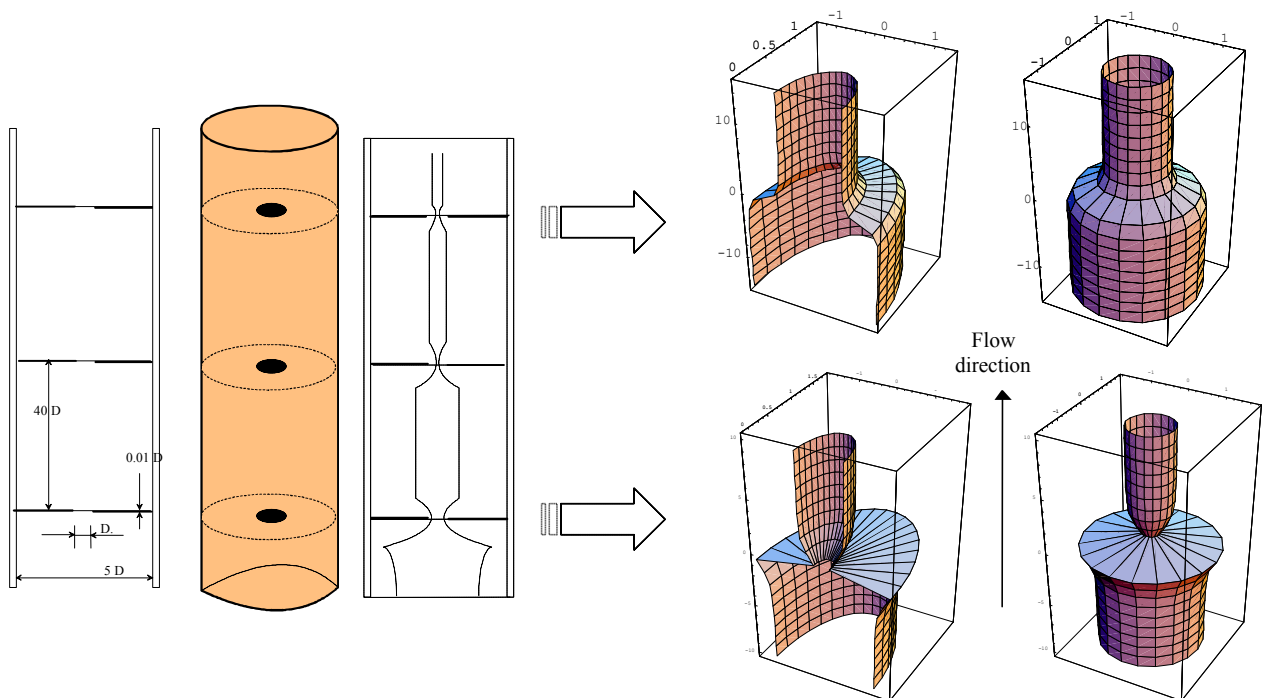


Fig. 5.1. A system of three aerodynamic lenses (left) and the calculated trajectories (right) for a $10\ \mu\text{m}$ particle passing through one aerodynamic lens (see A.2) for different positions of the particle relative to the centre of the lens.

In this case, the beam is produced by expanding an aerosol through a nozzle into an evacuated chamber. Downstream of the nozzle the carrier gas expands rapidly while the suspended particles tend to retain the motion they have acquired during the nozzle acceleration, due to their large inertia. So, after the particles pass an aerodynamic lens they are moved closer to the centreline. At the right side of Fig. 5.1, the expansion close to the system's origin (the plane of the aerodynamic lens) results from a mathematical approach but might be a bad choice for the initial condition.

Acoustic radiation pressure is capable of levitating [79], deforming [80] or moving particles that are entrained in a fluid medium. One possible application of this phenomenon is to concentrate small particles entrained in a moving air stream to a small section of the stream. This application can serve for the analysis of the particles [81]. For example: a hollow cylindrical piezoelectric crystal can be modified to tune the resonance frequency of the breathing mode resonance of the crystal to that of the interior cavity of the cylinder [82]. When the resonance frequency of the interior cylindrical cavity is matching to breathing mode resonance of the cylindrical piezoelectric transducer, the acoustic efficiency for establishing a standing wave pattern in the cavity is high. The cylinder does not require accurate alignment of a resonant cavity.

5.2 Charging devices

5.2.1 Diffusion charger

For a charging device it is important to reduce any possible source of flow and flow velocity perturbation e.g. from "corners". The development of an analysis device to investigate the physical parameters of flowing particles imposes a cylindrical geometry [83]. A typical construction is presented in Fig. 5.2. [84].

The material of the diffusion charger is an aluminium alloy. This material offers the desired mechanical and electrical properties. In order to keep a much higher flexibility (by changing) the charger device was constructed in a modular form: inlet-, unipolar charging and outlet-module.

The inlet-module consists of two parts: the aerosol inlet with an internal/external diameter of 3/5 mm and the charger admission unit with an internal diameter of 15 mm. Even in this cylindrical geometry particle losses can occur by contact with the chamber

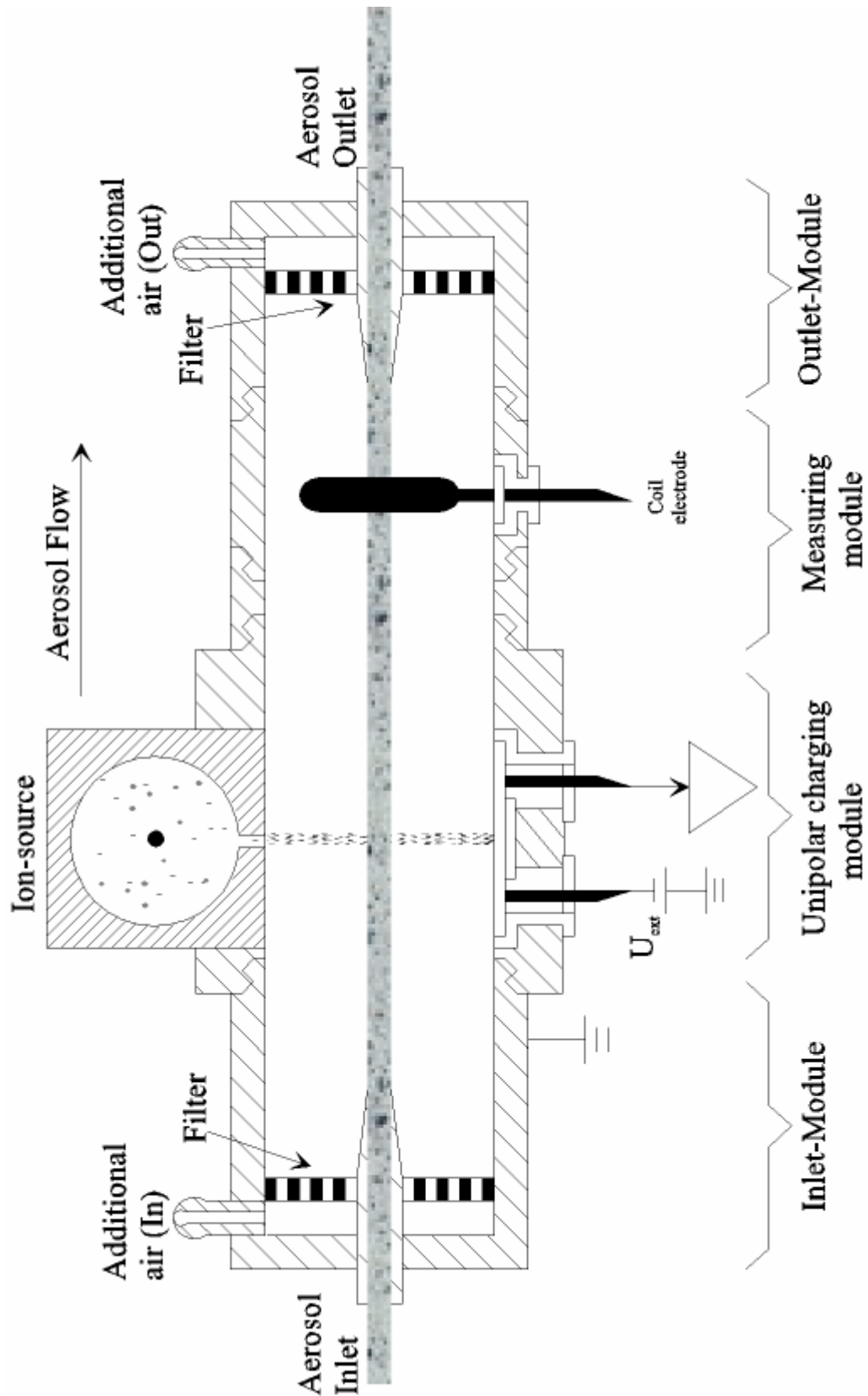


Fig. 5.2. Typical construction of a diffusion charger: Inlet-, Unipolar charging and Outlet-Module (see A.3a).

walls generated by fluid expansion [84]. Therefore a sheath of air was used to collimate the particles. The aerosols pass through the inlet into the charger device and will be surrounded by this ring-shaped air flow. In this case a direct contact between the particles and walls was avoided.

The unipolar charging module consists of two parts: the ion-source and the extraction electrode located in the charging chamber as depicted in Fig. 5.3.

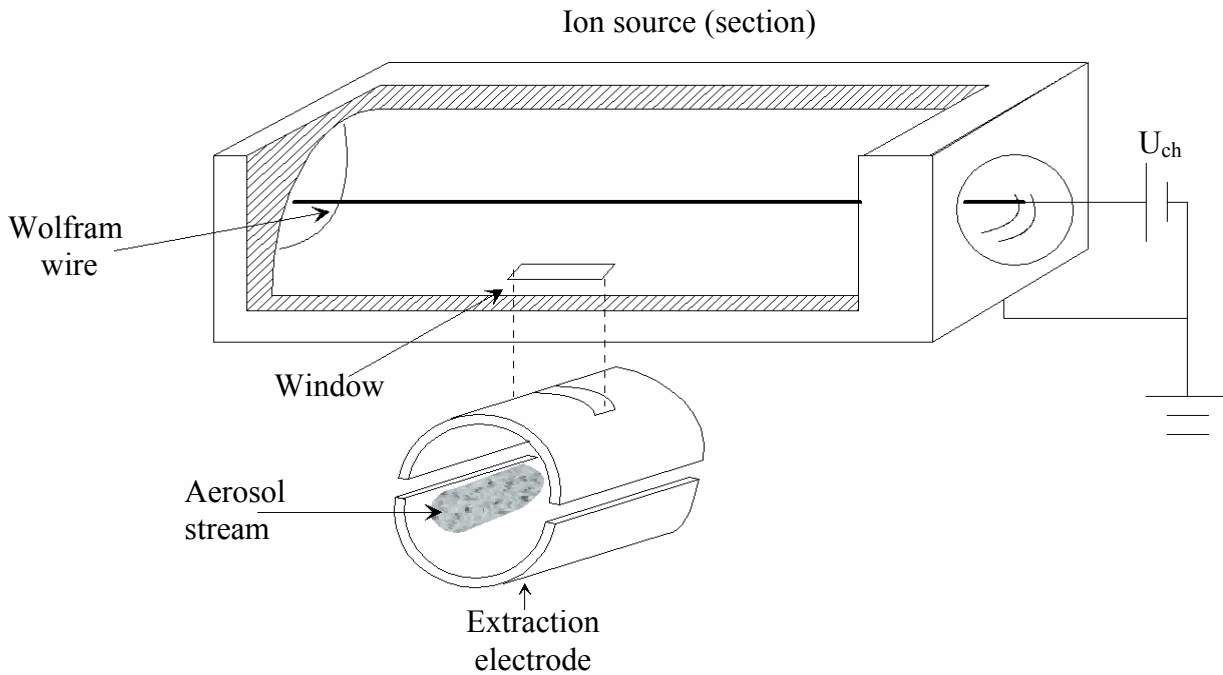


Fig. 5.3. The unipolar charging module: ion-source, and the extraction electrode (see A.3b).

This construction assures an independency between the different charging parameters. The two parts, ions source and extraction electrode are connected through a window in the ion-source, in such a way allowing ion diffusion into the charging chamber. A wolfram wire (50 μm) was stretched axially inside the cylindrical ion source cage with two teflon isolators. The isolators close the cavity air-tight and assure the exact axial position of the wire allowing in the same time the electrical connection of a continuous high voltage source U_{ch} . The applied DC potential (3.31 and 4.14 kV) on this wolfram wire is responsible for the ion generation. The ions are produced in the centre of the source (see Fig. 5.2.) and they move radially to the exterior. While the major fraction of them is removed by the source cage, a small amount diffuses through

the window (parallel cut with respect to the wire) in the charging chamber, where they are accelerated by the extraction potential U_{ext} (200 V) and travel to the opposite side. In the middle of the chamber they meet the aerosol stream and initiate the charging process by collisions. The extraction electrode satisfies two functions: (i) with its influence ions are extracted from the source and (ii) when ions are captured on it, an ion current can be measured using an amplifier; thus the ion concentration can be calculated in the charging zone.

The measuring module offers the possibility to measure the electric charge acquired by the particle. The measurement principle was described in Chapter 3 and considers the inductive electric interaction between a charged particle and a metal coil [24] when the charge moves rectilinearly along the geometrical axis (which corresponds to the charger axis). To evaluate the charge we have performed several measurements for each particle size d_p . The obtained values were used for averaging, and with the averaged values, the corresponding charge on the particle was calculated. The calculated number of elementary charges on the particle is listed in Table 5.1.

	n_q (a.u.)	n_q (a.u.)
d_p (mm)	$U_{ch} = 3.31kV$	$U_{ch} = 4.14kV$
0.94	8	12
4.05	34	62
5.44	48	80
6.15	56	92
9.11	84	134

Table 5.1. The number n_q of elementary charges on different particles.

The dependence between n_q and the particle diameter d_p is depicted in Fig. 5.4 for two different corona voltages. It can be observed that the particle mobility b (the ratio of the terminal velocity to the steady force producing that velocity) and the active surface S (the area accessible for impinging molecules of the carrier gas, measuring the interaction of the particle with the surrounding gas) are inversely proportional within an uncertainty of some percent ($\sim 3\%$). For Raman, the behaviour does not depend on

particle size, shape, or material (these dependencies are cumulated in the Cunningham correction factor as shown below).

$$b \cdot A = \text{const.},$$

$$b = \frac{1}{3\mathbf{p}h d_p}, S = \mathbf{p}d_p^2 \cdot \frac{2\mathbf{l} \cdot (A+Q)}{d_p + 2\mathbf{l} \cdot (A+Q \cdot e^{-b \cdot d_p / 2\mathbf{l}})}, \quad (5.1)$$

where \mathbf{h} is the viscosity of gas: air; \mathbf{l} is the mean free path of gas molecules, ~ 66 nm; d_p : diameter of the particle; A, Q, \mathbf{b} : Cunningham fit parameters from

$$C_C = 1 + \frac{2\mathbf{l}}{d_p} \cdot (A + Qe^{-b \cdot d_p / 2\mathbf{l}}). \quad (5.2)$$

The Cunningham correction factor is defined as [1]:

$$C_C = \frac{3\mathbf{p}hVd_p}{F_D} = \frac{3\mathbf{p}hVd_p}{(\mathbf{r}_p - \mathbf{r}_F)\mathbf{p}d_p^3g} \approx \frac{1}{1 - \frac{\mathbf{r}_F}{\mathbf{r}_p}} \quad (5.3)$$

where $V = V_{TS} = \frac{\mathbf{r}_p d_p^2 g}{18\mathbf{h}}$ is the terminal settling velocity identical with the velocity of

an aerosols particle undergoing gravitational settling in still air.

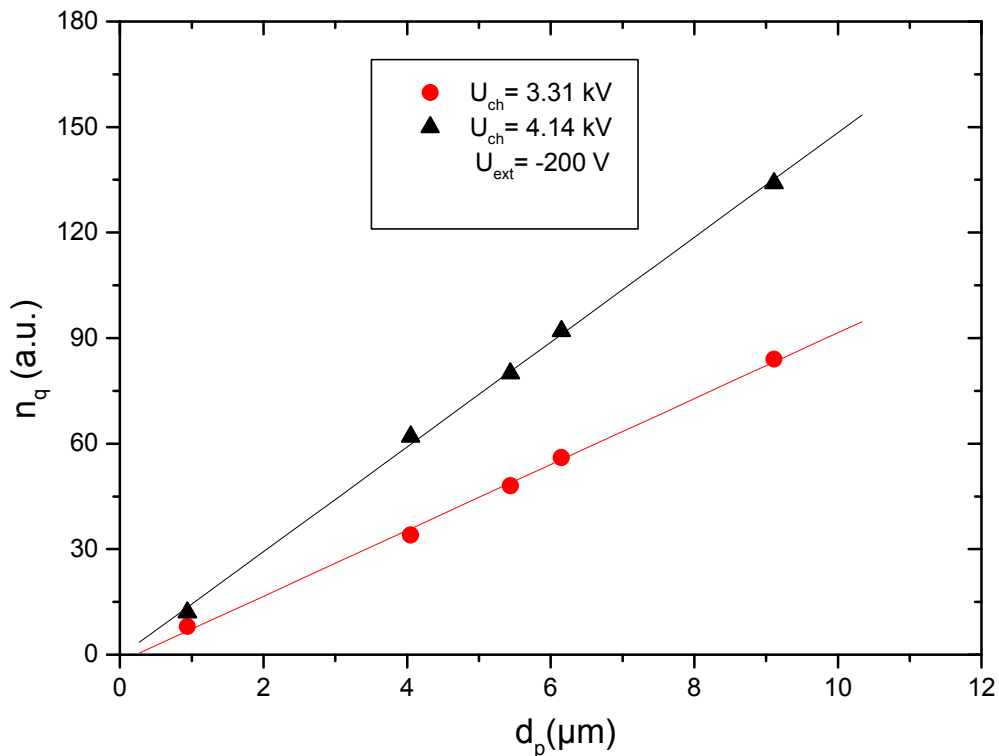


Fig. 5.4. The dependence between the acquired charge and particle diameter for two different corona voltages. The extraction potential has a constant value equal to -200 V.

From the definition of the Cunningham factor, a particle material dependence is predicted. Anyway this dependence is very weak allowing us to consider that $C_C \cong 1$ (for example, a water droplet settling in air has a density ratio $\frac{\rho_p}{\rho_F} = 800$ and neglecting the buoyancy introduces an error of only 0.1 %).

The exposed dependence between the particle mobility and active surface, implies a linear dependence between the particle charge and the particle diameter. This behaviour is common for the diffusion charging (see Chapter 3) as it is expected to be the case for the device presented here.

The outlet-module is constructed in the same way as the inlet-module, and will thus not be further explained.

5.2.2 Field charger

The diffusion charger presented in the previous paragraph is most efficient in charging particles with a diameter smaller than 2 μm , while for larger particles the Brownian motion is insufficient for acquiring high charge levels. Starting from a cylindrical configuration (see precedent paragraph) where the corona discharge appears along the axis of symmetry, the positive ions are moving in a radial direction to the exterior. To acquire a high charge level, an electric field is applied. So that, the motion of the ions and electrons is assumed to be driven in the direction of the electric field, which will increase the particle/ion collision rate. The environment near the corona wire can not be used as a charging zone because of the strong electric field and the ion concentration doesn't satisfy the requirements. By positioning a concentric grid between the corona wire and the measuring foil a screen is realised, which stops any undesired discharge. Applying a positive potential on this grid allows ions to travel in the region between grid and an external electrode [85]. A big disadvantage of this configuration is that even a small variation of the grid potential which producing the expected ion current needed for charging, will introduce a field distortion. In order to overcome this situation a second cylindrical electrode was introduced between the first grid and measuring electrode (the foil). Figure 5.5 shows the field charger concept [86].

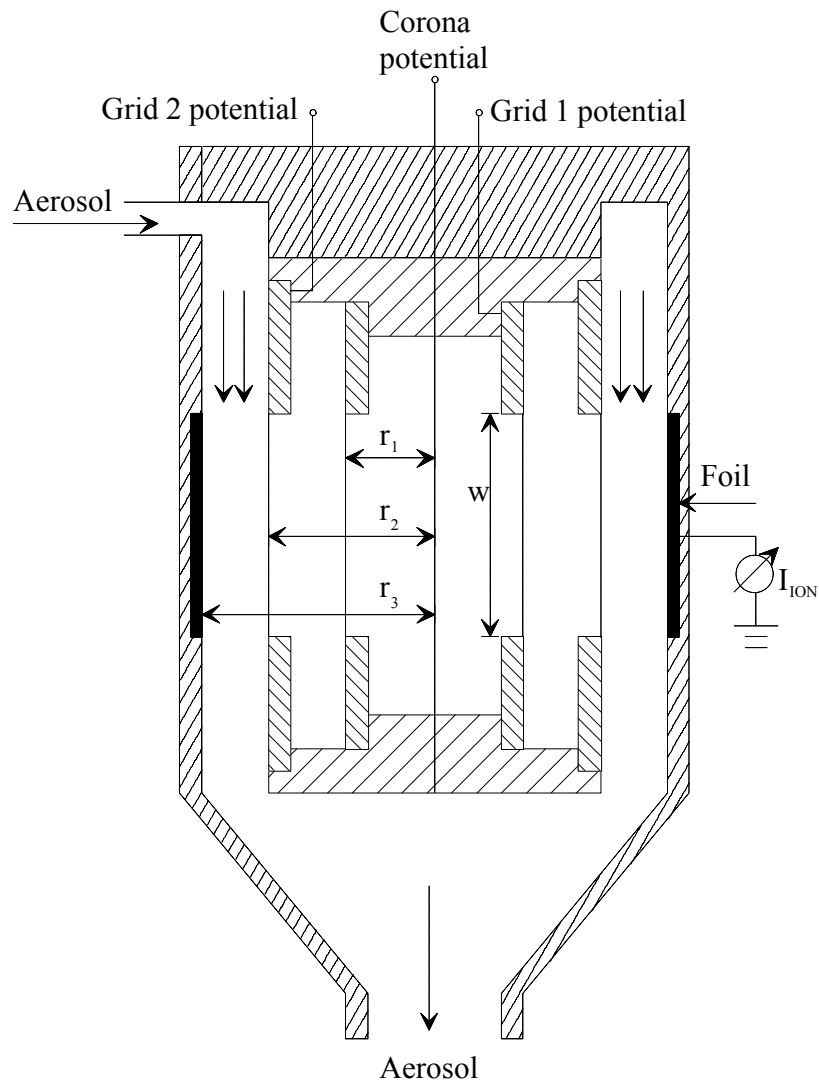


Fig. 5.5. The field charger concept (see A.4b).

Operation parameters: microparticles $d_p > 1 \mu\text{m}$		
Corona voltage	U_C	8 kV
Potential grid 1	U_{G_1}	3 kV
Potential grid 2	U_{G_0}	± 2.4 kV
Frequency grid 2	$f(U_{G_0})$	100÷400 Hz
Ion current	I_i	700 nA

Table 5.2. The parameters used in operation.

A high potential corona discharge U_C applied on a wolfram wire ($50 \mu\text{m}$) along the axis of the three concentric cylinders produces positive ions. The inner cylinder with

the grid (mesh) is connected to a constant potential U_{G_i} for a stable corona discharge (as a function of the potential difference $U_C - U_{G_i}$ the ion rate generation can be controlled). U_{G_i} is variable to adjust the ion current to the outer grid being on potential U_{G_0} without disturbing the ion generation. The ratio of the electric field inside and outside the outer grid determines which fraction of this current enters the aerosol charging zone [85]. The housing cylinder is grounded. To minimise the particle losses in the charging zone, U_{G_0} is a square wave voltage [87] as depicted in Fig. 5.6. An insulated foil at the inner side of the charger housing (made out of plastic), opposite to the grids, is connected to a current amplifier to measure the ion flow current. At the same time, the charging area is periodically filled with ions, while the charged particles perform an oscillatory motion of small amplitudes in a high electric field (see A.4).

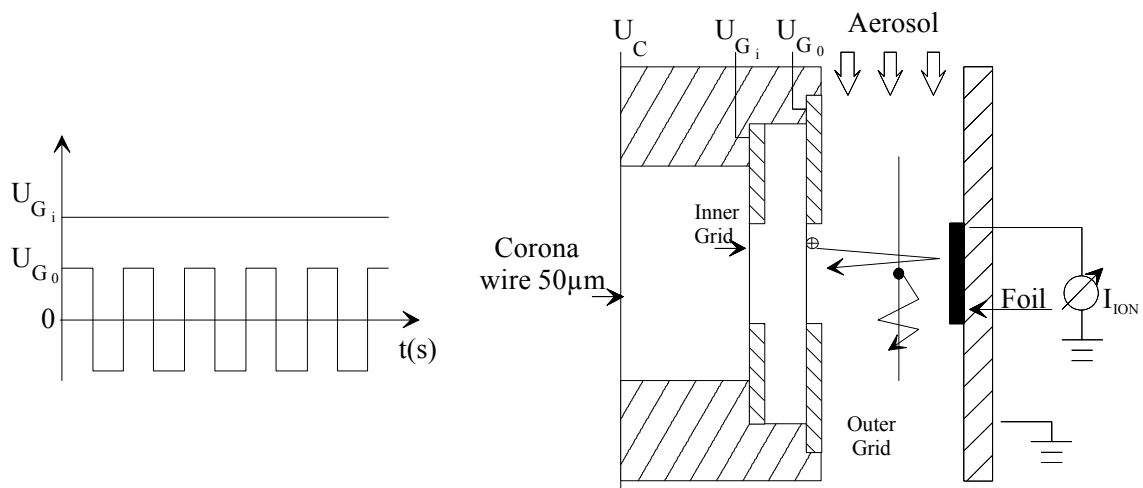


Fig. 5.6. Section through the field charger (right side, see also A.4a); the applied voltages (left side).

The measured electrical charge of the particle is illustrated in Fig. 5.7. As a reference the results from the diffusion charging device are also presented. Examining the graph it can be concluded that the charge obtained on the particle with this device increases compared to the diffusion charger; for big particles the differences are much more accentuated while for small particles these are not so significant.

Another important conclusion resulting from Fig. 5.7 deals with the slope of the curves. As mentioned in the previous paragraph for diffusion charging, the linear

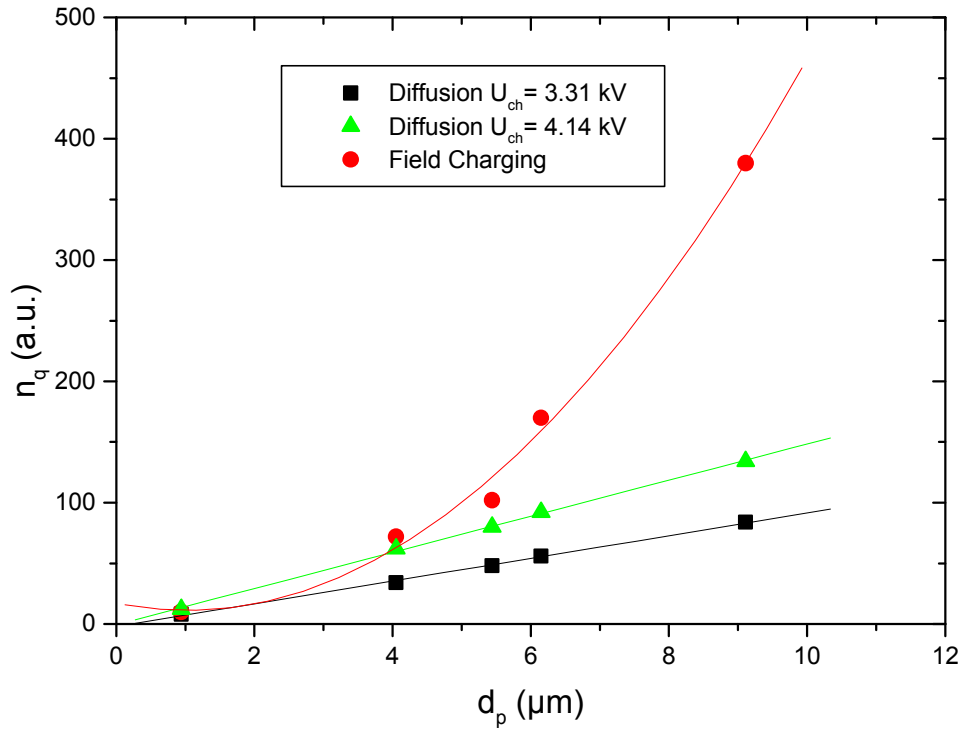


Fig. 5.7. The number of the elementary charges versus particle diameter obtained with the field charger device (circle); as reference the results from the diffusion charging device are also presented.

dependence between the particle charge and particle diameter implies that the charge does not depend on the particle material. Following the same algorithm, a material dependence for the field charging was observed (the charge vs. diameter dependence for the field charger is no linear, but rather shows a square dependence). This result can be also confirmed by examination of eqs. 3.2 and 3.3 (see Chapter 3). Another material dependence will be presented below.

Normally, in field charging models for spherical particles it is assumed that the particle does not rotate. However rotation would lead an increased charging rate for high resistively particles. It is a common assumption that viscous resistance forces prevent the rotation of particles [20].

If we assume a non-uniform charge distribution on the particle (the normal case of a real particle with no perfect surface), the particle rotation can be quantitatively analysed by calculating the rotation W induced by the electric force \mathbf{F}_e on a charge q , as $W \sim \tilde{N} \cdot \mathbf{F}_e$. Considering the axial-symmetric geometry the approximation yields:

$$\Omega \approx \nabla \times F_e = \nabla \times \begin{pmatrix} qE_r \\ qE_q \\ 0 \end{pmatrix} = q \begin{pmatrix} 0 \\ 0 \\ \frac{\partial(rE_q)}{r\partial r} - \frac{\partial E_r}{r\partial q} \end{pmatrix}. \quad (5.4)$$

For the development presented in Chapter 3 it can be shown that for field charging W is zero. For a more general case, the time scale for a rotation due to a non-equilibrium charge distribution may be approximated by modelling the particle as a cylinder with length l and radius r_p , $l \gg r_p$ [19]. The rotation along its axis is determined by the electric torque T , the density of the material ρ_s , the dynamic viscosity of the surrounding medium η_F and the moment of inertia of the cylinder I . As an illustration, the steady-state value for Ω (assuming that $\Omega(0)=0$) is given [20] by:

$$\Omega = \frac{2e_0 E_0^2 r_p}{\eta_F} \left(\frac{e_r - 1}{e_r + 2} \right). \quad (5.5)$$

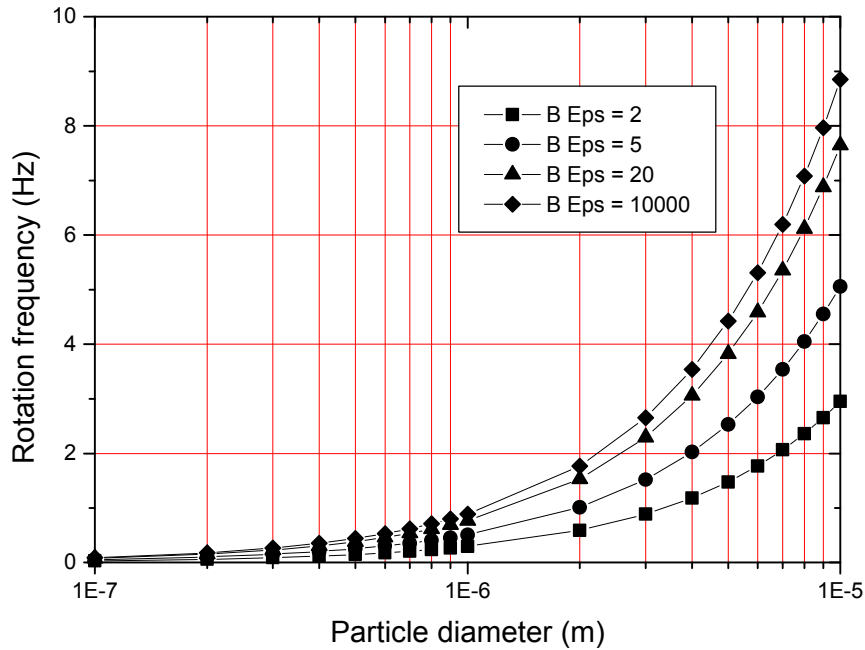


Fig. 5.8. Particle rotation frequency versus particle size [90].

For $E_0 = 10^6$ V/m, $\eta_F = 2 \cdot 10^{-5}$ Pa·s and the relative dielectric constants $e_r(Eps) = 2, 5, 20$ and ∞ this steady-state value for Ω is given in Fig. 5.8. This result indicates that the

viscous effects cannot prevent a rotation of the particle due to an unbalanced charge distribution of the particle.

A major disadvantage of this system is that just the positive half-cycle of the alternating potential is responsible for the ion presence in the charging zone. In the same time, considering the applied alternating electric field it is obvious that particles for which the distance to the electrode is smaller than the amplitude of the imposed oscillation, are lost. Thus a new type of charger which improves these disadvantages was constructed.

5.2.3 AC charger: bi-directional, uni-polar charging

Research of electrostatic precipitation, electrostatic coating and electrical methods of particle size measurement need precise and controllable charging of small particles. The main shortcoming of the conventional methods of particle charging, using DC corona discharge is the limit of charge acquired by a particle [1, 2]. Several methods have been proposed to overcome this disadvantage [88, 89]; most of them apply an AC electric field in the charging zone. Two types of chargers utilising this concept were proposed in the literature. The first device was developed by Masuda et al. [17, 91]. In such a device the ions were generated by a high frequency surface discharge while the alternating electric field of low frequency was imposed on the corona discharge zone by an additional pair of electrodes. A similar idea was implemented by Jaworek and Krupa [19, 92]. The ions were emitted by a corona discharge from needle electrodes, and the electric field was generated by two additional grids, forming the charging zone [93, 94]. By using an alternating electric field the following problems can be avoided: the collection of particles on one electrode and the low charge imparted to the small particles.

The schematic diagram of the alternating electric field charger is shown in Fig. 5.9. The charger consists of discharge electrodes and two grids spaced at 5 mm forming the charging zone. The grids were made of stainless mesh with a wire diameter of 0.5 mm, 80 mm height and 30 mm wide. The discharge electrodes, A and B, were composed of a set of 3×14 stainless needles spaced at 5 mm. The electrodes were placed

15 mm behind each grid. The diameter of the needles was 1 mm, its length 10 mm and the angle of the cone was 25°.

The electrodes of the charger were supplied by two high voltage (~2 kV) transformers in a diode circuit as shown in Fig. 5.9.

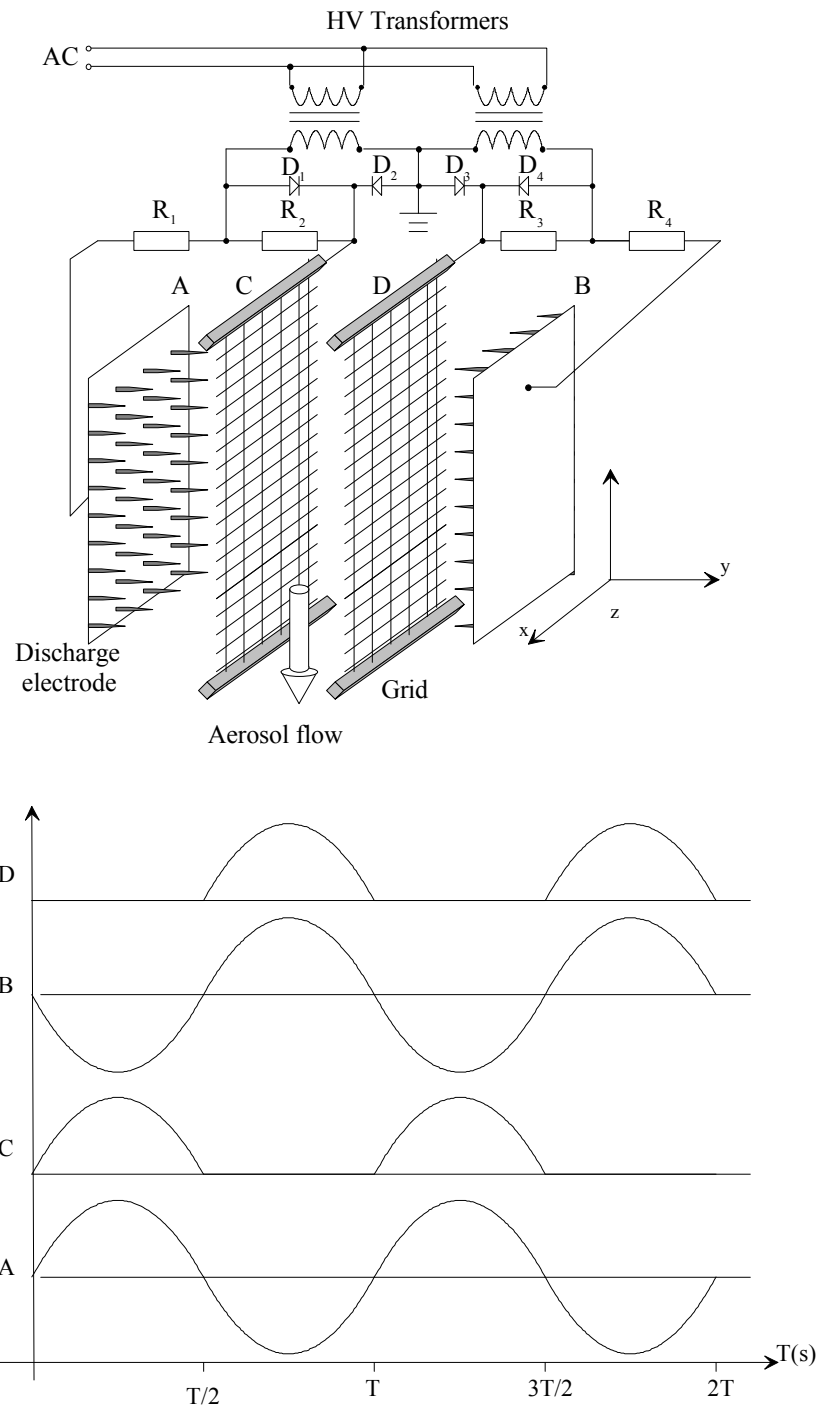


Fig. 5.9. The schematic diagram of the alternating electric field charger - top, and the applied potential – bottom (see A.5).

The transformer windings are connected in such a way as to obtain an opposite sign of the potential of each grid at the same half-cycle. In the first half-cycle of the AC voltage, the electrodes A and C have positive potential while the electrode B is at negative potential relative to the grounded grid D. The negative ions emitted from the electrode B are accelerated by the potential of the grid C, and fly through the plane of the grid D to the grid C. The ions passing the charge zone between the grids C and D form a negative space charge. Particles flowing across the charging zone are bombarded and charged by these ions. In the second half-cycle, the whole situation is reversed; the negative ions emitted from electrode A are accelerated by the potential of the grid D, and flow throughout the plane of the grid C to D. The frequency of the excitation was varied between 30 and 500 Hz.

The oscillation amplitude depends both on the value of the electric charge of the particle and the value of the alternating electric field. In the charging zone the amplitude increases with an increased value of the AC voltage. The charging proceeds until the electric field acting on the particle is too low to drive the ions to the particle. For higher frequencies, oscillation amplitude is low, and for this reason high frequencies are more appropriate for particle charging (see A.5b, c). Higher amplitudes and low frequencies can lead to a collection of particle on the electrodes.

5.3 Charged particle containment

5.3.1 The Electrodynamic Balance

Electrodynamic balances have become a major tool for studies involving single and multiple particle reactions and dynamics. Both hyperboloidal and toroidal rings have been used in electrodynamic balances and also the literature available concerning the stability of particles in such systems is very extensive. A straightforward technique for evaluating the radial and axial components of the electric field at the centre of the balance was given by Singer [95] and was recently applied by Sloane and Elmoursi [96], Davis [34, 97] and Loyalka et al. [98]. Generally, particle motion in an electric field is described by :

$$m \frac{d^2 \bar{r}(t)}{dt^2} = q \bar{E}(\bar{r}, t) + \bar{F}_g(\bar{r}) + \bar{F}_D(d\bar{r}/dt) \quad (5.6)$$

where m is the particle mass, $\bar{r}(t)$ is the particle displacement, q is the particle charge, $\bar{E}(\bar{r}, t)$ is the electric field, \bar{F}_g is the body force and \bar{F}_D the drag force. \bar{F}_g and \bar{F}_D are described by:

$$\bar{F}_g = -mg\bar{n}_z \quad \bar{F}_D = -K_D \frac{d\bar{r}(t)}{dt} \quad (5.7)$$

where K_D is the drag coefficient defined as $K_D = 3\mu m d_p / C_c$. Here μ is the gas viscosity, d_p is the particle diameter, and C_c is the Cunningham correction factor which is a function of the Knudsen number $Kn = \lambda / d_p$ where λ is the gas mean free path. The electrical field is typically approximated by:

$$\bar{E}(\bar{r}, t) = \bar{E}_{DC}(\bar{r}) + \bar{E}_{AC}(\bar{r}) \cos(\omega t). \quad (5.8)$$

In previous studies, the time-independent component of the electric field $\bar{E}_{DC}(\bar{r})$, was assumed to act only in the z -direction for all values of \bar{r} . Using cylindrical coordinates and assuming axial symmetry, particle motion and stability in the balance are then described by the following coupled ordinary differential equations:

$$m \frac{d^2 r}{dt^2} = -K_D \frac{dr}{dt} + q E_{r, AC}(r, z) \quad (5.9)$$

$$m \frac{d^2 z}{dt^2} = -K_D \frac{dz}{dt} + q [E_{z, DC}(r, z) + E_{z, AC}(r, z) \cos(\omega t)] - mg \quad (5.10)$$

for the radial and axial motion, respectively. By substituting:

$$2t = \omega t \quad A = \frac{K_D}{m\omega} \quad \text{and} \quad B = \frac{q}{m\omega^2} \quad (5.11 \text{ a, b, c})$$

and further assuming that the axial force of the DC electrical field exactly compensates the body force at all points, the equations 5.9 and 5.10 can be normalised to:

$$\frac{d^2 r}{dt^2} = -2A \frac{dr}{dt} + 4BE_{r,AC} \cos(2t) \quad \text{and} \quad (5.12)$$

$$\frac{d^2 z}{dt^2} = -2A \frac{dz}{dt} + 4BE_{z,AC} \cos(2t). \quad (5.13)$$

Once the AC electric field is specified, these equations can be solved even by applying Mathieu functions or, more generally, by numerical methods. The determination of the electric field for relevant geometries, requires the solving of the Laplace equation. In the aerosol literature, this task has been accomplished by using analytical techniques developed by Wuerker et. al [42], Müller [99], Davis[100] and Hartung and Avedisian [101] and has been accomplished applying the charge simulation technique described by Sloane [96], Davis et al. [100, 102]. Both techniques present in some cases considerable limitations. The analytical techniques can give full description of the electric fields only for geometries in which a separation of the variables is possible (e.g. hyperboloidal rings). For certain axial symmetric geometries, polynomial expansions can also be used to provide a description of the electric fields near the null points (near the centre of the system) [101].

Computation of the electric field

Connected with a stability analysis is the computation of the electrical potential in the balance. The potential is determined from the solution of the Laplace equation:

$$\nabla^2 \Phi = 0 \quad (5.14a)$$

$$\frac{1}{r} \cdot \frac{\partial}{\partial r} \cdot \left(\frac{\partial(r\Phi)}{\partial r} \right) + \frac{\partial^2 \Phi}{\partial z^2} = 0 \quad (\text{cylindrical coordinates})$$

together with appropriate boundary conditions :

$$\Phi(\bar{r}_s) = \text{as specified}, \quad \lim_{|\bar{r}| \rightarrow \infty} \Phi(\bar{r}) = 0. \quad (5.14b)$$

Here, \bar{r}_s indicates a point on the surface which may be multiply connected or disjoint. The boundary value problem can be solved by the use of finite elements. However one of the most effective methods solving this problem is to use the Green's function. This allows the conversion of the partial differential equation with its boundary conditions, to

an integral equation of reduced dimensionality [98]. The analytical solution for the potential in toroidal coordinates is given by [103]:

$$\Phi(\mathbf{z}, \mathbf{h}) = [\cosh(\mathbf{z}) - \cosh(\mathbf{h})]^{1/2} \cdot \sum_{n=0}^{\infty} A_n P_{n-1/2}(\cosh(\mathbf{z})) \cos(n\mathbf{h}) \quad (5.15)$$

where the A_n coefficients are found by applying the boundary conditions (eqs. 5.14a and 5.14b) to equation 5.15. The potential can then be expressed as:

$$\Phi(\mathbf{z}, \mathbf{h}) = [\cosh(\mathbf{z}) - \cosh(\mathbf{h})]^{1/2} \frac{\sqrt{2}\Phi_0}{p} \left[\frac{Q_{-1/2}(\cosh(\mathbf{z}_0))}{P_{-1/2}(\cosh(\mathbf{z}_0))} P_{-1/2}(\cosh(\mathbf{z})) + 2 \sum_{n=1}^{\infty} \frac{Q_{-1/2}(\cosh(\mathbf{z}_0))}{P_{-1/2}(\cosh(\mathbf{z}_0))} P_{-1/2}(\cosh(\mathbf{z}_0)) \cos(n\mathbf{h}) \right] \quad (5.16)$$

The transformation to cylindrical coordinates, $\Phi(\mathbf{z}, \mathbf{h}) \rightarrow \Phi(r, z)$, is achieved by substituting \mathbf{h} and \mathbf{z} from the following equations :

$$\mathbf{h} = \cos^{-1} \left[\frac{R_1^2 + R_2^2 - (2c)^2}{2R_1 R_2} \right] \text{ and } \mathbf{z} = \ln \left(\frac{R_2}{R_1} \right) \quad (5.17a)$$

where

$$R_1^2 = z^2 + (r - c)^2, \quad R_2^2 = z^2 + (r + c)^2 \quad \text{and} \quad (5.17b)$$

$$c_0 = \sqrt{R_0^2 - a_0^2}, \text{ and } \mathbf{z}_0 = \cosh^{-1} \left(\frac{R_0}{a_0} \right) \quad (5.17c)$$

Once the potential is expressed, the electric field can be calculated from:

$$\bar{\mathbf{E}} = -\nabla\Phi \quad (5.18)$$

$$E_r(r, z) = -\frac{\partial}{\partial r}\Phi(r, z), \text{ and } E_z(r, z) = -\frac{\partial}{\partial z}\Phi(r, z). \quad (5.19)$$

Ring-charge simulation

A straightforward technique for evaluating the radial and axial components of the electric field at the centre of the four ring balance has been provided by Singer [95].

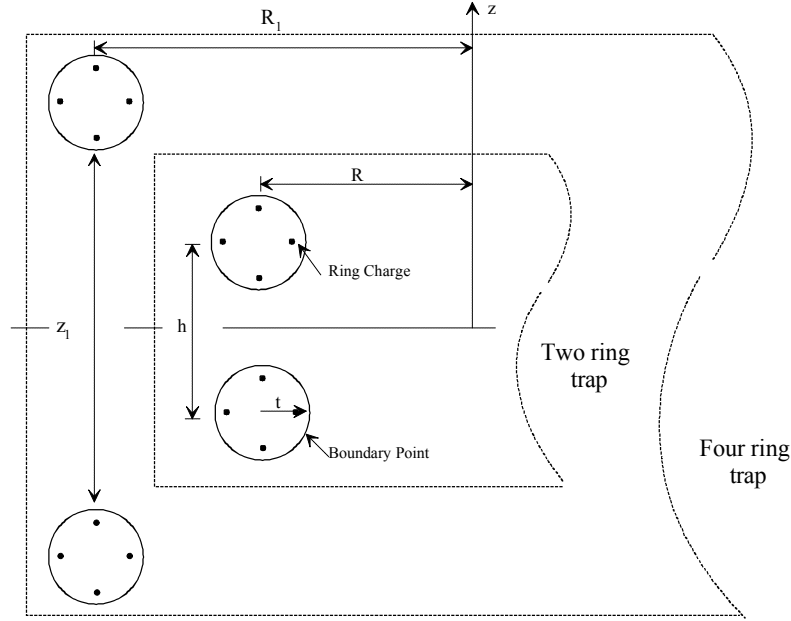


Fig. 5.10. Location of the ring charges to determine the ring potential for a two ring trap; for a four ring trap. The theoretical development is the same for both (see B.1a, b).

The method called charge simulation, approximates the potential of a surface by placing fictitious discrete charges outside the space where the field is calculated. This technique is used first for designating the location of the N ring charges which simulate the constant potential electrode [70] and then for generating an N by N matrix geometric constant for each ring charge. In a next step, the boundary conditions for the charges on each ring are applied, then the potential is obtained by summing the contribution from all ring charges. For a ring of a radius r_i , the total potential is given by:

$$\Phi(r, z) = \sum_{i=1}^N \frac{q_i}{4\pi\epsilon_0} \frac{2K(k_i^2)}{\mathbf{p}\mathbf{a}_i} \quad (5.20)$$

where $K(k_i^2)$ is the complete integral of first order, ϵ_0 is the permittivity of free space, and k_i^2 and \mathbf{a}_i are defined as:

$$k_i^2 = \frac{4rr_i}{\mathbf{a}_i^2} \quad \text{and} \quad \mathbf{a}_i^2 = (r + r_i)^2 + (z - z_i)^2 \quad (5.21)$$

Solving equation 5.18 for the electric potential one gets the electric field in the radial and axial direction:

$$E_{ac,r} = \sum_{i=1}^N \frac{-q_i}{4\mathbf{p}e_0} \cdot \left\{ \frac{[r_i^2 - r^2 + (z - z_i)^2]E(k_i^2) - \mathbf{b}_i K(k_i^2)}{\mathbf{p}r\mathbf{a}_i\mathbf{b}_i^2} \right\} \text{ and} \quad (5.22)$$

$$E_{ac,z} = \sum_{i=1}^N \frac{q_i}{4\mathbf{p}e_0} \cdot \frac{2(z - z_i)E(k_i^2)}{\mathbf{p}a_i\mathbf{b}_i^2} \quad (5.23)$$

where $E(k_i^2)$ is the complete elliptic second kind integral and \mathbf{b}_i^2 is given by:

$$\mathbf{b}_i^2 = (r - r_i)^2 + (z - z_i)^2. \quad (5.24)$$

Examining eqs. 5.22 and 5.23, it can be seen that the axial and radial equations of motion are decoupled when the electric field expressions are linearized in the neighbourhood of the centre of the balance (near the null point). For the four ring configuration the axial electric field component is greater than the radial component. So, the particle will become unstable first in the vertical direction, and the onset of instability can be described by the z-component of the equation of motion. A ring potential was obtained by solving the Laplace equation in cylindrical coordinates (5.14a), and differentiating the electric field components were obtained (5.19). The axial electric field is then given by:

$$E_{ac,z} = \frac{\mathbf{p}V_{ac} \cos \omega t}{\Psi(\mathbf{x}_1, \mathbf{x}_2)[R^2 + h^2]^2} z \quad (5.25)$$

where $\Psi(\mathbf{x}_1, \mathbf{x}_2)$, \mathbf{x}_1 and \mathbf{x}_2 are defined as:

$$\Psi(\mathbf{x}_1, \mathbf{x}_2) = \frac{K(\mathbf{x}_1)}{(2R - t)} + \frac{K(\mathbf{x}_2)}{[(2R - t)^2 + 4h^2]^{\frac{1}{2}}} \quad (5.26)$$

$$\mathbf{x}_1 = 1 - \frac{t^2}{4R(R - t)} \text{ and } \mathbf{x}_2 = 1 - \frac{t^2 + 4h^2}{4R(R - t)} \quad (5.27)$$

Using the above described analysis a similar result for the DC field can be obtained.

$$E_{dc,z} = \frac{\mathbf{p}V_{dc} h}{\mathbf{j}(\mathbf{x}_1, \mathbf{x}_2)[R^2 + h^2]^2} z \quad (5.28)$$

where

$$\mathbf{j}(\mathbf{x}_1, \mathbf{x}_2) = \frac{K(\mathbf{x}_1)}{2R} - \frac{K(\mathbf{x}_2)}{2(R^2 + h^2)^{\frac{1}{2}}}. \quad (5.29)$$

The computational results for the AC field are displayed in a three-dimensional form in Fig. 5.11. The AC potential is shown for $\omega t = 0$, that is, at its maximum strength. The influence of the support posts can be clearly seen in the two ridges extending out from the central depression (the rods are opposite connected).

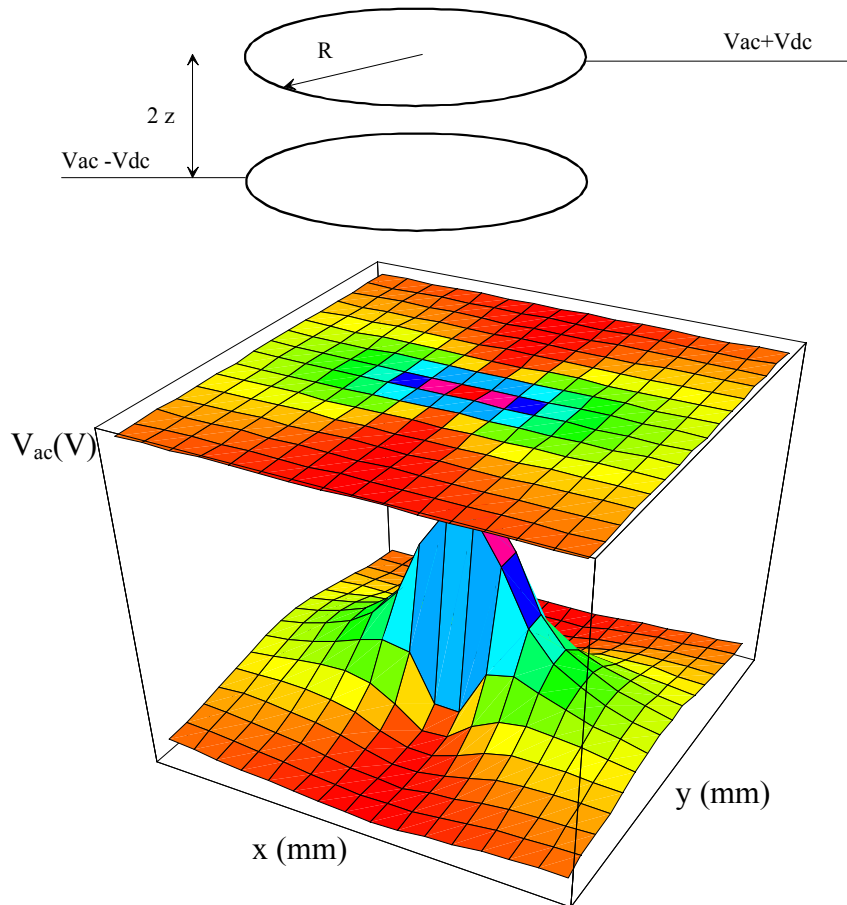


Fig. 5.11. The AC potential distribution at the midpoint ($z = 0$) calculated for the presented configuration.

A simpler and more useful depiction of the AC field is presented in Fig. 5.12., showing the potential at the midplane ($z=0$) in the plane of the posts (parallel) and in the plane perpendicular to the posts. The distortion of the AC field by the posts is clearly indicated by the bulge in the potential and by the deeper potential well in the centre of the chamber. By fitting and differentiating the data in Fig. 5.12, the resulted function can be used to determine the C_1 constant. In this case two different values are obtained, $C_{||}$ and C_{\perp} for the parallel and perpendicular direction respectively. The mean value of C_1 should be close to the perpendicular value while the effects of the rods are limited to small angles.

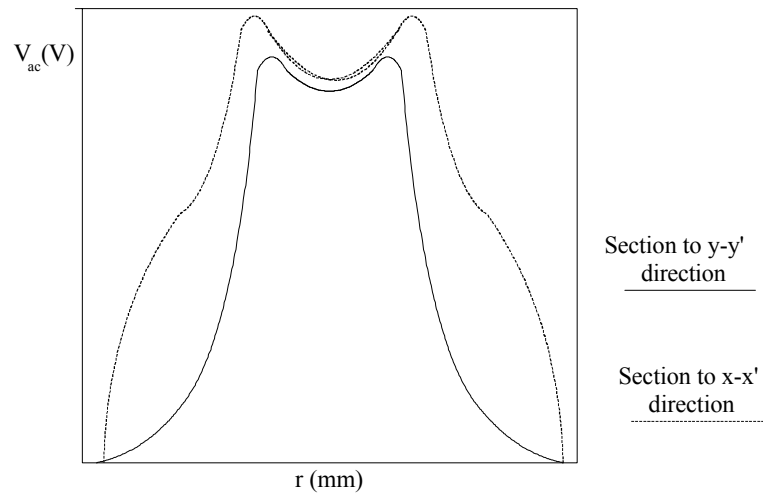


Fig. 5.12. The AC potential distribution corresponding to the direction parallel and perpendicular to the supporting rods.

When the supporting rods are connected on the same side the field is looks like the one depicted in the Fig. 5.13. Than, by performing a section through xx' direction we get:

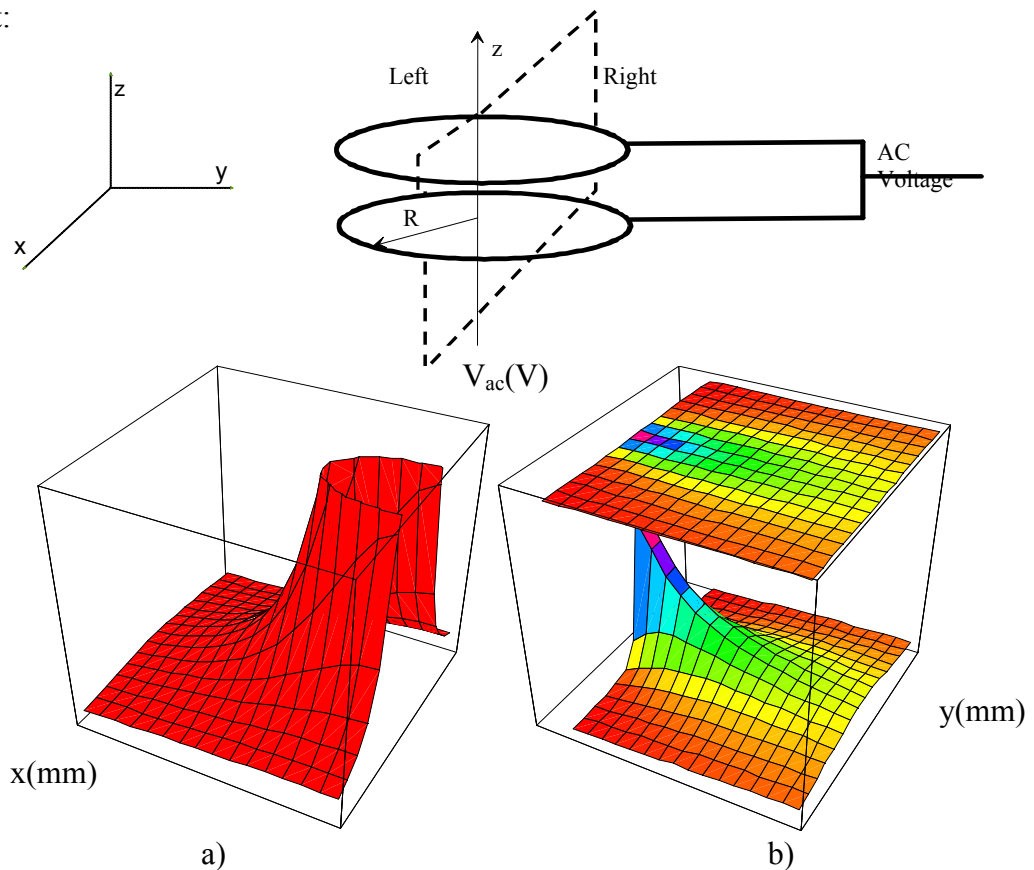


Fig. 5.13. The AC potential distribution at the midpoint ($z = 0$) for a geometry illustrated in the upper part of the figure; a) and b) represent the electric field in the regions on the left and right of the section plane (dashed lines).

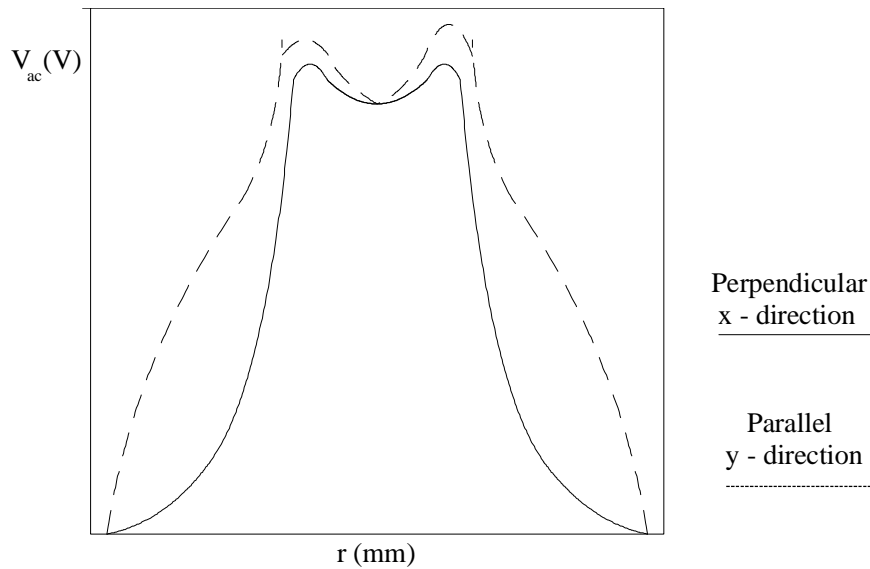


Fig. 5.14. The AC potential for the rods connected on the same side (section through the electric potential upon a direction parallel to the supporting rods).

Comparing Fig. 5.12 and Fig. 5.14, a second distortion along yy' direction can be founded. This distortion will increase the instability of the balance. Because of the distortion of the electric field created at the connecting point between the wire and the ring, the particles may be trapped in-between these connection points (see B.2).

A similar numerical procedure as for a AC field has been applied for a DC electric field. The three-dimensional DC field at the middle for the rings without support

Fig. 5.16.

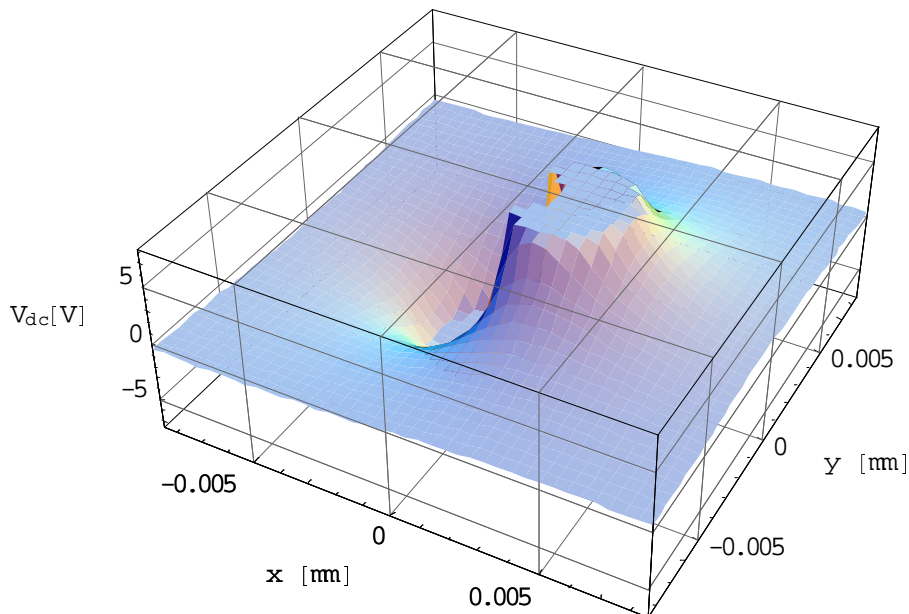


Fig. 5.15. The DC potential distribution at the middle plane ($z = 0$).

Generally, the DC field is used to balance vertical forces while the AC field acts to focus a charged particle at the null-point of the balance (in the centre of the balance).

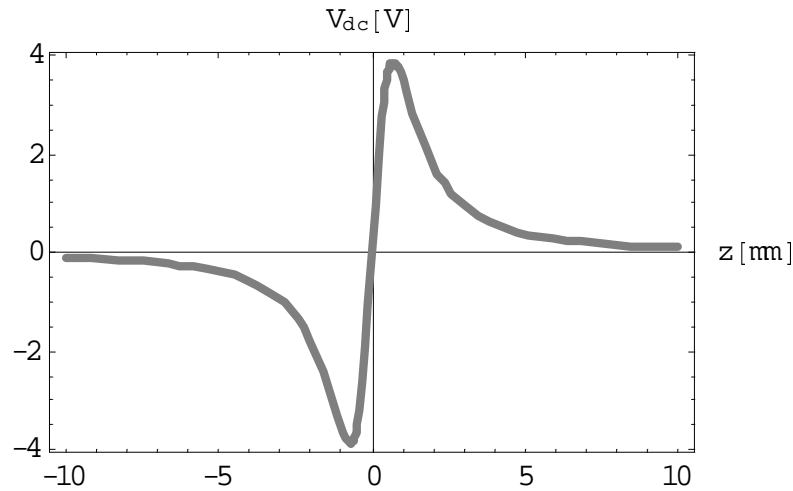


Fig. 5.16. The DC potential distribution as a function of z on the axis of the chamber ($r = 0$).

For a single particle of mass m and charge q , levitated in the mid-plane of the rings, a vertical force balance yields:

$$-mg + \sum_i F_i = C_0 \frac{qV_{dc}}{z_0} \quad (5.30)$$

where g is the gravitational acceleration, $2z_0$ is the separation distance between the rings, F_i represents vertical forces and C_0 is the *levitation strength constant*, which is a geometrical factor that accounts for the deviation of the DC field from the uniform field generated by infinite parallel plates.

Substituting the result obtained for $E_{ac,z}$ (eq. 5.25) in the equation of vertical motion (eq. 5.10), and considering that at the middle plane the DC voltage balances all vertical forces equation 5.10 is reduced to:

$$m \frac{d^2 z}{dt^2} + K_D \frac{dz}{dt} - \frac{q\pi V_{ac} \cos \Omega t}{\Psi(\xi_1, \xi_2) [R^2 + h^2]^2} z = 0. \quad (5.31)$$

Examining this relation a similar constant C_1 (*stability strength constant*) as the one derived for the DC field (C_0 in eq. 5.30) can be introduced. Knowing C_0 and C_1 the

regions of stable operation for any balance can be calculated. For different geometries both C_0 and C_1 have been calculated. The results are listed in Table 5.3.

A		B		C		D		Davis	
	R_1	z_1	t_1	R_2	z_2	t_2	C_0	C_1	
A	8	6.7	0.8	3.4	2.4	0.5	0.612	0.0942	
B	5	6	0.5	8	3	0.5	0.065	0.0317	
C	5	3	0.5	-	-	-	0.504	0.0721	
D	5	6	0.5	-	-	-	0.65	0.138	
Davis	6.5	2.65	0.8	-	-	-	0.383	0.0399	
Hyperboloidal		$R_0/z_0 = 1.4142$				$C_0 = 0.800$			

Table 5.3. The values for C_0 and C_1 obtained for different geometries (specified by A, B, C, D. For comparison the results from Davis [100] and Wuerker [42]) are also listed. The symbols have the same signification as in Fig. 5.10, all values are given in mm.

Based on the similarity among the equations listed above (5.9-10 and 5.12-13) and the Mathieu equations an identical stability characteristic with respect to the ideal case, of an bihyperboloidal device can be expected. A complete description of the stability maps is given in the paper from Hartung und Avedisian [101]. As mentioned before, the equation of motion for a particle in the electrodynamic balance is governed by the Mathieu equations. There are two different classes of these equations represented by the (i) homogeneous and (ii) inhomogeneous form. The first class (i) equations are:

$$\frac{d^2}{dt^2}r(t) + [a + q \cdot \cos(\omega t)]r(t) = 0, \quad (5.32a)$$

$$\frac{d^2}{dt^2}z(t) + [a + q \cdot \cos(\omega t)]z(t) = 0. \quad (5.32b)$$

For the second class, the equations contain a damping coefficient δ :

$$\frac{d^2}{dt^2}r(t) + \delta \cdot \frac{d}{dt}r(t) + [a + q \cdot \cos(\omega t)]r(t) = 0, \quad (5.33a)$$

$$\frac{d^2}{dt^2} z(t) + \mathbf{d} \cdot \frac{d}{dt} z(t) + [a + q \cdot \cos(\mathbf{w}t)]z(t) = 0. \quad (5.33b)$$

By substituting $r \cdot e^{-\mathbf{d}t}$ with r and $z \cdot e^{-\mathbf{d}t}$ with z , the two equations (5.33a and 5.33b) can be reduced to the form of eqs. 5.32a and 5.32b, while the a coefficient is transformed to $a - \mathbf{d}^2$. Generally the solutions for the Mathieu equations are $ce_m(z, q)$ and $se_m(z, q)$ for even and odd solutions respectively [57]. A more general expression can be obtained using the Floquet theory [104]:

$$y(t) = e^{\mathbf{d}t} \Xi(t) + e^{-\mathbf{d}t} \Xi(-t) \quad (5.34)$$

where

$\Xi(t)$ and $\Xi(-t)$ are bounded and periodic with \mathbf{p} , and \mathbf{d} is a complex constant called the characteristic exponent.

An important aspect of these functions is the a dependence upon q . As a function of $ce_m(z, q)$ and $se_m(z, q)$ the characteristic numbers a_m and b_m can be obtained [105]. The stable regions are defined as the regions between the characteristic numbers a_m and b_m . The stability region for the homogeneous Mathieu equation is plotted in Fig. 5.17 and Fig. 5.18.

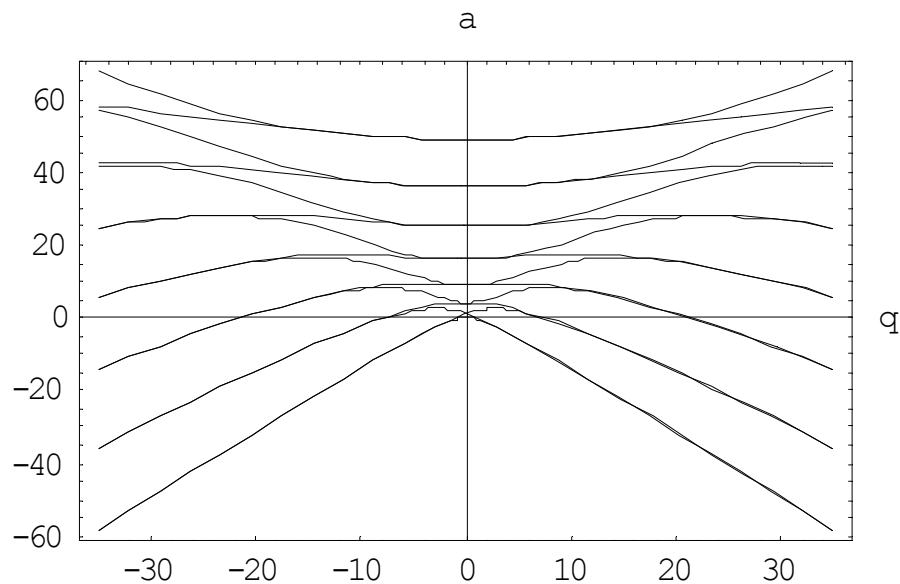


Fig. 5.17. The general form of the characteristic numbers and stability regions for the homogeneous case.

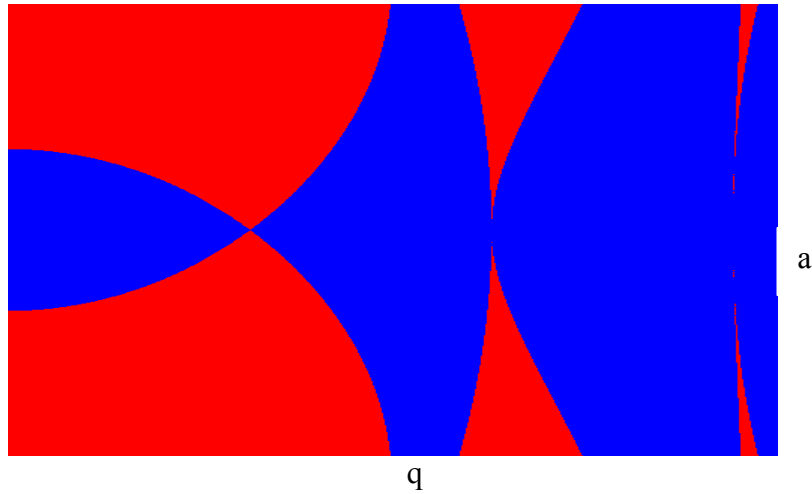


Fig. 5.18. The first three stability (blue) and instability regions (red).

For the damped (inhomogeneous) equations, different authors used different stability criteria, as mentioned before. Gunderson [106] has found the following stability criteria:

$$q = a^{1/2} \cdot \mathbf{d} + \mathbf{d}^2 \quad (5.35)$$

while Taylor & Narendra [107] derived:

$$q^2 = (a - 1)^2 + (2\mathbf{d})^2 \quad (5.36)$$

where the symbols significations are given by the Mathieu equation.

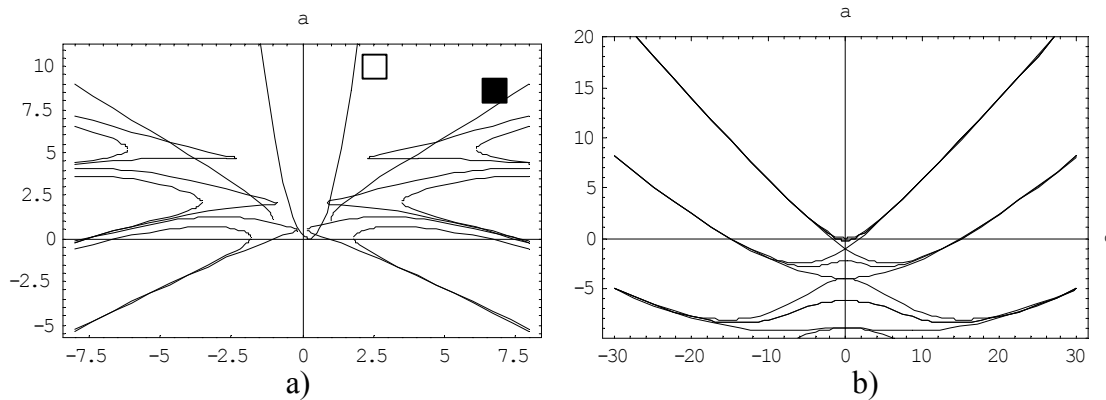


Fig. 5.19. a) and b) the approximated stability diagram for damped Mathieu equation with $\mathbf{d} = 0.5$ plotted in axial respectively radial direction. Also is shown the stability criteria of Gunderson (eq. 5.35 white square) and Taylor (eq. 5.36 black square).

As can be observed in Fig. 5.19, the stability regions for the axial and radial direction differ from the homogeneous case. The performed calculations show that the predicted results from reference [107] are acceptable for small d but are incorrect for d in the vicinity of 0.5 or higher, since the results presented in reference [106] are acceptable just for small values of d . Comparing the stability for axial and radial direction an amplitude difference can be observed (explained in the quadrupole section). The entire stability region (in order to trap a stable particle into the trap) is obtained by the superposition of both axial and radial stability regions. The stability regions for the homogeneous and inhomogeneous case are shown in the Fig. 5.20.

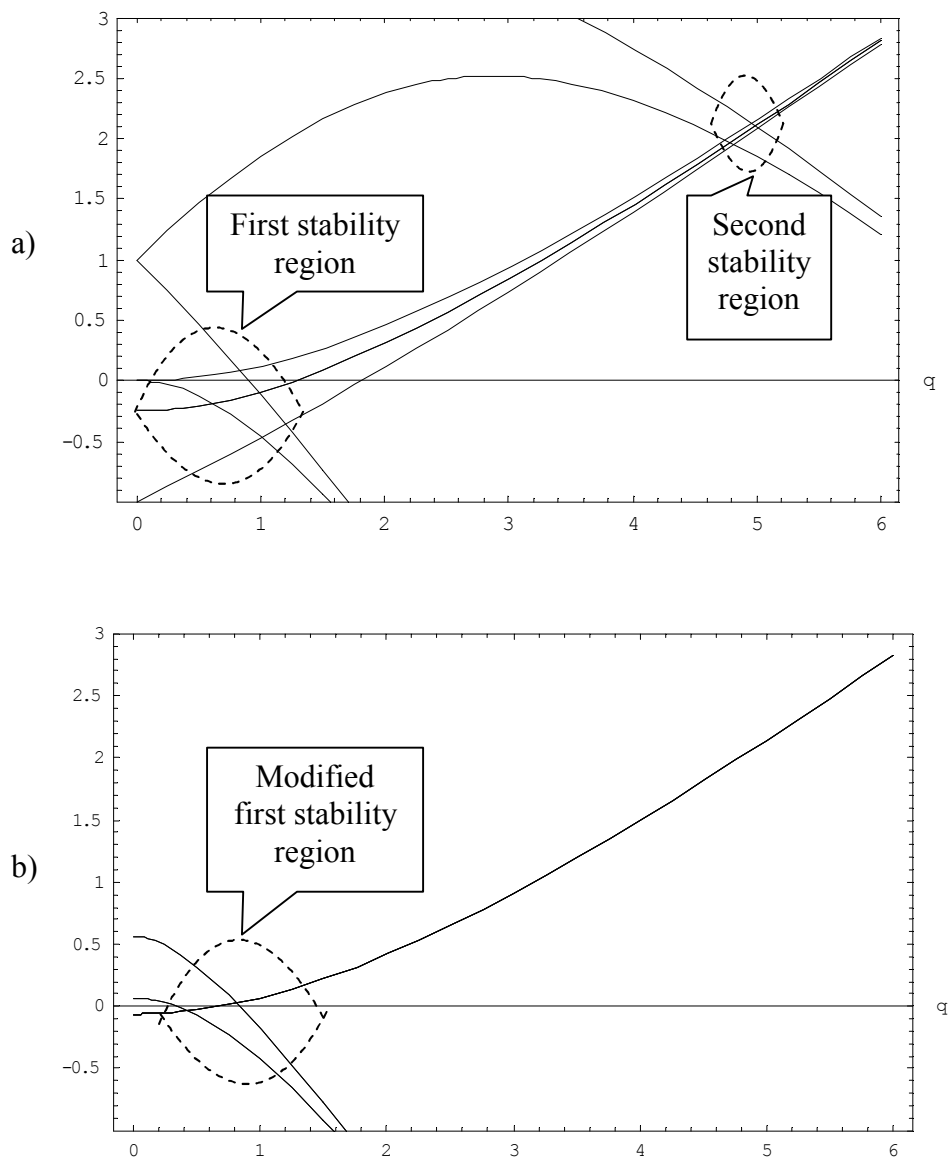


Fig. 5.20. The stability regions; a) the homogeneous case with the first and second stability region; b) the inhomogeneous case with the first stability region.

Following an inverse algorithm as that one exposed to deduce the stability regions, once calculated, these regions were used to develop the system. The importance of this development is twofold: first, (i) the drag and field strength parameters provide design criteria to permit the construction of a ring set that will give stable operation second, (ii) this analysis defines the voltage ranges available to suspend a particle stable for a particular ring geometry (knowing the measured electric charge, particle mass and the air flow properties, these maps have been used to choose the DC and AC values for potential and frequency).

Frickel [108] *et al.* calculated the entire stability envelope (marginal stability curve) and Davis [34] computed the first four unstable regions using a method called the spring point technique.

Phase Injection

Once the electric fields are determined, the particle trajectory can be obtained by studying the equation of motion for the inhomogeneous case. Performing this study a strange behaviour of the charged particles inside the electrodynamic trap has been observed. These results show that the phase of the AC potential plays a crucial role in particle trapping. There are two ways to prove that: (i) by solving numerically the equation of motion in the axial direction (which is also similar for the radial direction, Ref. [14]), or (ii) by using the theoretical development of Fang [110]. In Figs. 5.20 and 5.21 a simulation of a typical particle trajectory and maximum displacement is shown.

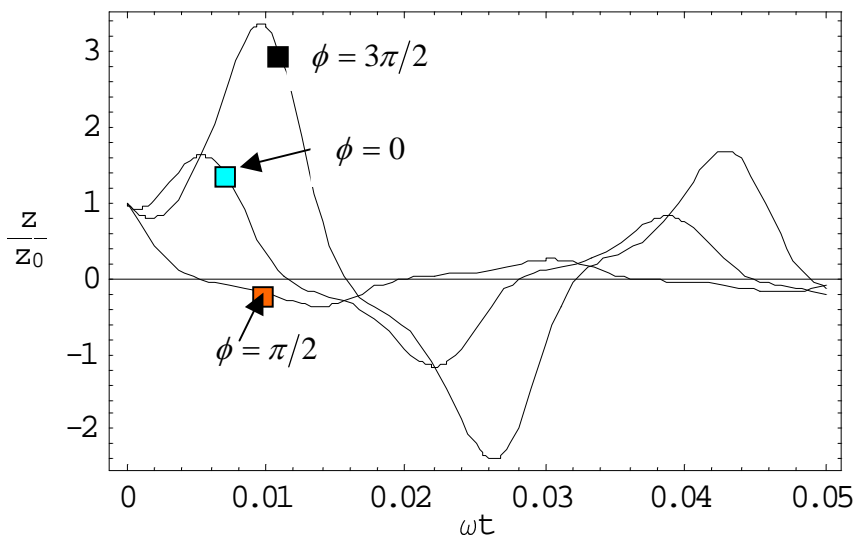


Fig. 5.21. The normalised trajectories $\frac{z}{z_0}$ of injected particles at various frequency phases ϕ represented through different boxes.

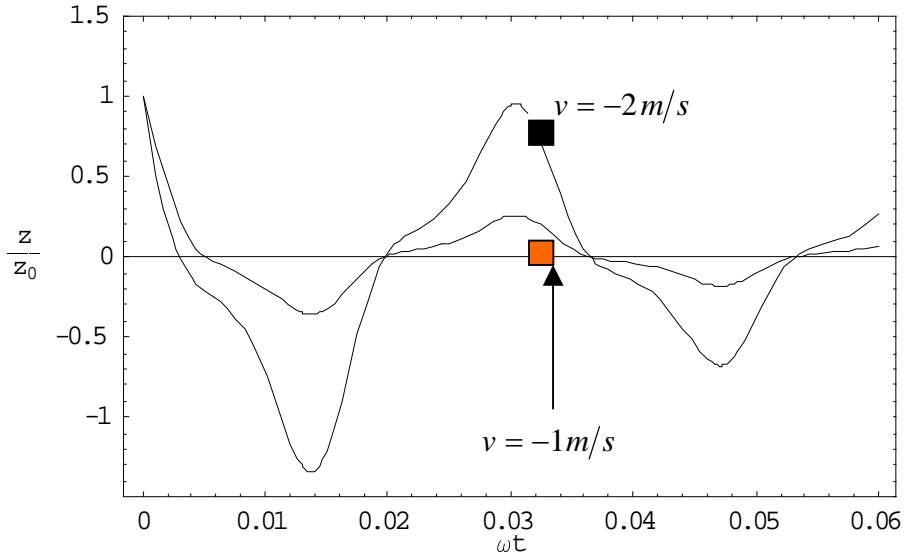


Fig. 5.22. Maximum excursion (normalised) for a particle in Fig. 5.20 vs. phase for $v = -1$ and $v = -2\text{ m/s}$.

Here at $t = 0$ a particle having a diameter of $10\ \mu\text{m}$ and carrying a specific charge $q/m = 2.29 \cdot 10^{-3}\ \text{C/kg}$ is injected into the trap from the top electrode located at $z_0 = 4.5\text{mm}$, with a velocity of -1 m/s . As one can see the phase of injection ϕ plays a crucial role in the trapping process. For our simulated parameters injection at $\phi = 0$ or $\phi = 3\pi/2$ causes the particle to collide with the top electrode ($\frac{z}{z_0} \geq 1$), in less than one trap cycle. However for $\phi = \pi/2$ the particle is trapped. In all these calculations only the AC potential was considered.

The influence of the DC potential was considered by the second method which calculates the density of probability to find a particle in one position in our system as a function of different voltages and frequencies. This can be done by using a series expansion of functions to solve the corresponding Schrödinger equation for the electrodynamic trap. The theoretical values obtained are listed in Table 5.4.

U_{dc} (V)	V_{ac} (V)	ω (s^{-1})	t=0		t= $\pi/2$		t= π	
			r	ρ	r	ρ	r	ρ
1	4	10	2.274	0.5895	2.193	0.6142	2.112	0.6406
		30	2.202	0.6115	2.193	0.6142	2.184	0.617
		50	2.196	0.6133	2.193	0.6142	2.19	0.6152
1	1	10	2.211	0.6079	2.193	0.6142	2.172	0.6207
		30	2.193	0.6136	2.193	0.6142	2.19	0.6149

		50	2.193	0.614	2.193	0.6142	2.19	0.6145
1	0.3	10	2.199	0.6123	2.193	0.6142	2.187	0.6162
		30	2.193	0.614	2.193	0.6142	2.19	0.6145
		50	2.193	0.6142	2.193	0.6142	2.193	0.6143
2	8	10	2.025	0.6708	1.875	0.7305	1.731	0.7984
		30	1.89	0.724	1.875	0.7305	1.86	0.7371
		50	1.881	0.7281	1.875	0.7305	1.869	0.7328
2	2	10	1.914	0.7148	1.875	0.7305	1.839	0.7466
		30	1.881	0.7288	1.875	0.7305	1.872	0.7321
		50	1.878	0.7299	1.875	0.7305	1.875	0.7311
2	0.6	10	1.887	0.7257	1.875	0.7305	1.866	0.7353
		30	1.878	0.73	1.875	0.7305	1.875	0.731
		50	1.875	0.7303	1.875	0.7305	1.875	0.7306

Table 5.4. Maximum radius and peak values of the trapping probability for different values of U_{dc} , V_{ac} , ω and t .

Table 5.5 shows some selected values in order to observe the probability behaviour as a function of phase, also presented in a graph form in Fig. 5.22.

ωt ($^\circ$)	0	$\pi/2$	π	$3\pi/2$	2π
ρ (%)	0.6708	0.7305	0.7984	0.7305	0.6708

Table 5.5. Selected values for ωt and ρ .

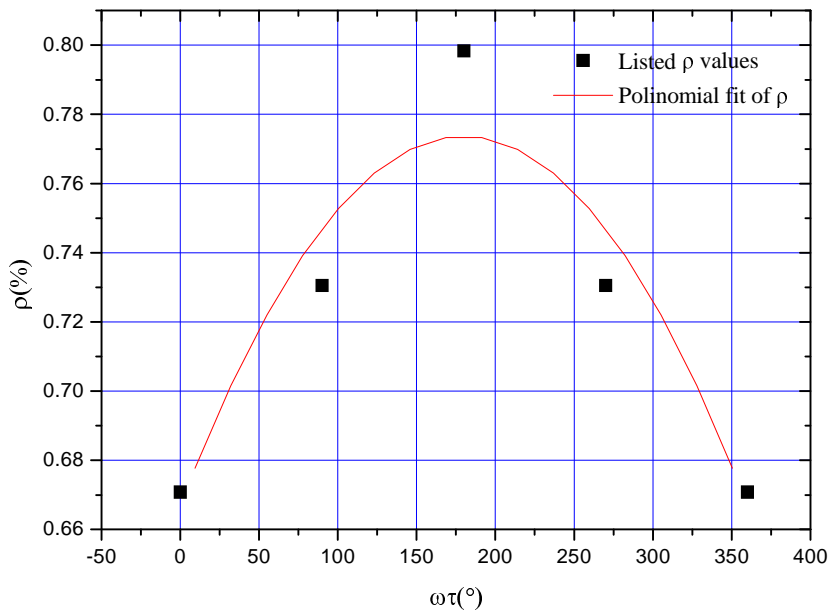


Fig. 5.23. Typical curve for probability dependence of ωt .

From the simulations (Figs. 5.21 and 5.23) and the presented values in the tables 5.4 and 5.5, it can be concluded that the injection of particles at a random phase will cause the loss of many particles. This aspect is very important, since charged particles adhering to the electrodes lead to stray electric fields and to background contamination which can ruin sensitive experiments, such as the detection of a single particle.

This disadvantage can be suppressed either by placing a phase synchronising circuit between the AC ring electrodes and the particle input, or by using an appropriate geometry for the trapping system for which the phase of the alternative potential will not show this strong dependence.

Considering the purpose of the presented work, it is very difficult to build a phase synchronising circuit for particles that are flowing in air (these particles are brought into the system at random times), so another type of trapping system has been developed, namely the quadrupole trap.

5.3.2 Quadrupole system

The motion of ions in quadrupole devices differ greatly from straight lines and arcing curves of ions in free-field regions and in magnetic or electrostatic sectors. The quadrupole ion trap and the quadrupole mass filter are described as dynamic instruments since ion trajectories in these instruments are influenced by a set of time-dependent forces. These time-dependent forces make the prediction of particle trajectories in dynamic instruments more difficult as for sector (static which means that the electric or magnetic field has no time dependence) instruments.

An ion in a quadrupole field experiences strong focusing in that the restoring force, which drives the ion back towards to the centre of the device, increases as the ion deviates from the centre of the device. It has been found that the ion motion in a quadrupole can be described mathematically by the solutions of the second-order differential equation described originally by Mathieu [1]. From Mathieu's investigation of the mathematics of the vibrating stretched skins, he was able to describe solutions in terms of regions of stability and instability. It can be easily shown that the equation of motion of an ion confined in a quadrupole device is described by Mathieu's equation.

The general construction of such a quadru-, hexa- or octopole was presented in Chapter 3. The trapping potential created within the electrode assembly of the

quadrupole ion trap can be compared to a bowl of parabolic cross section [55, 111, 112] as shown in Figure 5.24.

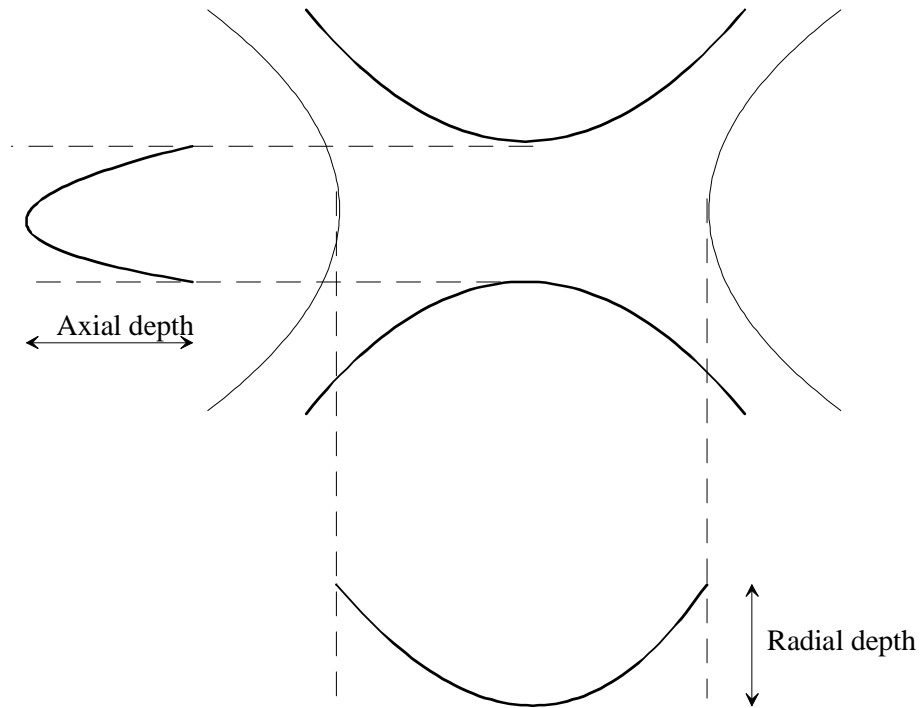


Fig. 5.24. Representation of the parabolic trapping potential wells.

The quadrupole potential can be expressed as:

$$\phi = \frac{\phi_0}{r_0} (\lambda x^2 + \sigma y^2 + \gamma z^2) \quad (5.37)$$

where ϕ_0 is the applied electric potential (an alternating potential $V \cdot \cos(\omega t)$ with ω the AC potential frequency or a combination of AC and DC potential $U + V \cdot \cos(\omega t)$), λ , σ and γ are weighting constants for the x , y and z coordinates, respectively, r_0 is a constant which is defined separately depending on whether the quadrupole device is an ion trap or mass filter. In any electric field, it is essential that the Laplace equation, which requires that the second differential of the potential at a point (origin) to be equal to zero, is satisfied (ensure that the field in the x , y and z direction is linear). When that is done, it was found that [40]:

$$\lambda + \sigma + \gamma = 0. \quad (5.38)$$

For the ion trap, $\lambda = \sigma = 1$ and $\gamma = -2$, whereas for the quadrupole mass filter $\lambda = -\sigma = 1$ and $\gamma = 0$. Substituting these values, the following expression for the potential at any point within the quadrupole field in a quadrupole ion trap can be obtained [41]:

$$\phi = \frac{\phi_0}{r_0} (x^2 + y^2 - 2z^2) \quad (5.39a)$$

or transforming in cylindrical coordinates

$$\phi_{r,z} = \frac{\phi_0}{r_0} (r^2 - 2z^2) \quad (5.39b)$$

The force (considering the x direction) experienced by an ion of mass m and charge e at any point within a quadrupole field is [41]:

$$F_x = m \cdot a = m \frac{d^2x}{dt^2} = -e \frac{\partial \phi}{\partial x}. \quad (5.40)$$

By substituting the electric potential in the last term of eq. 5.40 it can be shown that:

$$m \frac{d^2x}{dt^2} = -\frac{2e}{r_0^2} (U + V \cdot \cos \omega t) \quad (5.41)$$

which represents the Mathieu equation. The solutions of these equation can be interpreted in terms of trajectory stability (and instability) in each of the x , y and z directions similar with the described maps for the electrodynamic balance.

The trapping system consists of four steel rods (1.5 mm diameter and 110 mm length, placed at 5 mm one to another) and two tubes (3 mm in diameter and 40 mm length – see B.3). The last two electrodes which are usually separated by 20 mm determine the symmetry axis, perpendicular to the plane shown in Fig. 5.25.

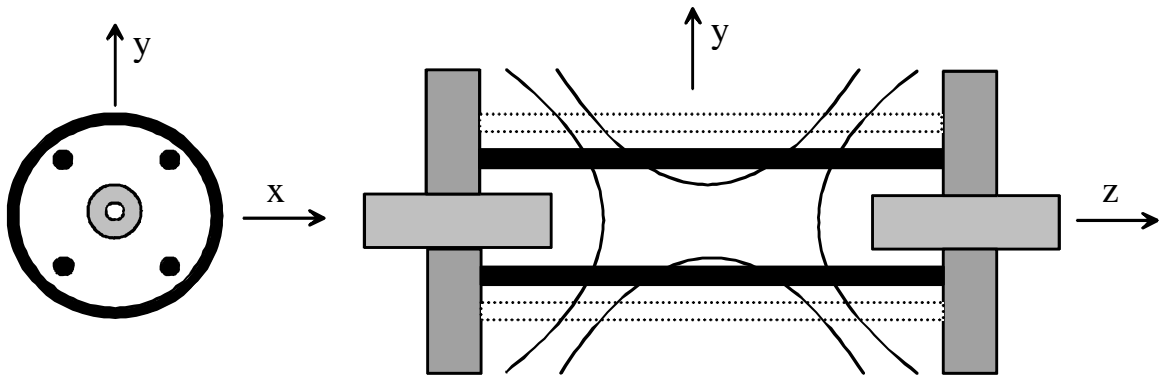


Fig. 5.25. Sectional view of the quadrupole system. The four steering rods are seen in the x - y plane (left side). Both tubes and the quadrupole electrodes are shown in the y - z plane (right side). In addition the parabolic trapping potential wells are presented.

For reducing the air flow perturbation from the chamber, the quadrupole device was installed in an enclosure (a glass tube) to protect the particle stream. The tube electrodes are supplied with a DC voltage (0-1000 V) usually of opposite polarity for vertical stabilisation of the charged particles. The other four electrodes have an AC voltage (0-7000 V) necessary for stabilising the microparticle radially in the centre of the system [113]. The frequency of the AC potential can be varied from 30-1500 Hz. The studied particle trajectories were relatively nonsensitive to the choice of the AC potential and frequency.

The calculated normalised electric field inside the quadrupole is plotted in Fig. 5.26 together with the equipotential lines and a gradient representation.

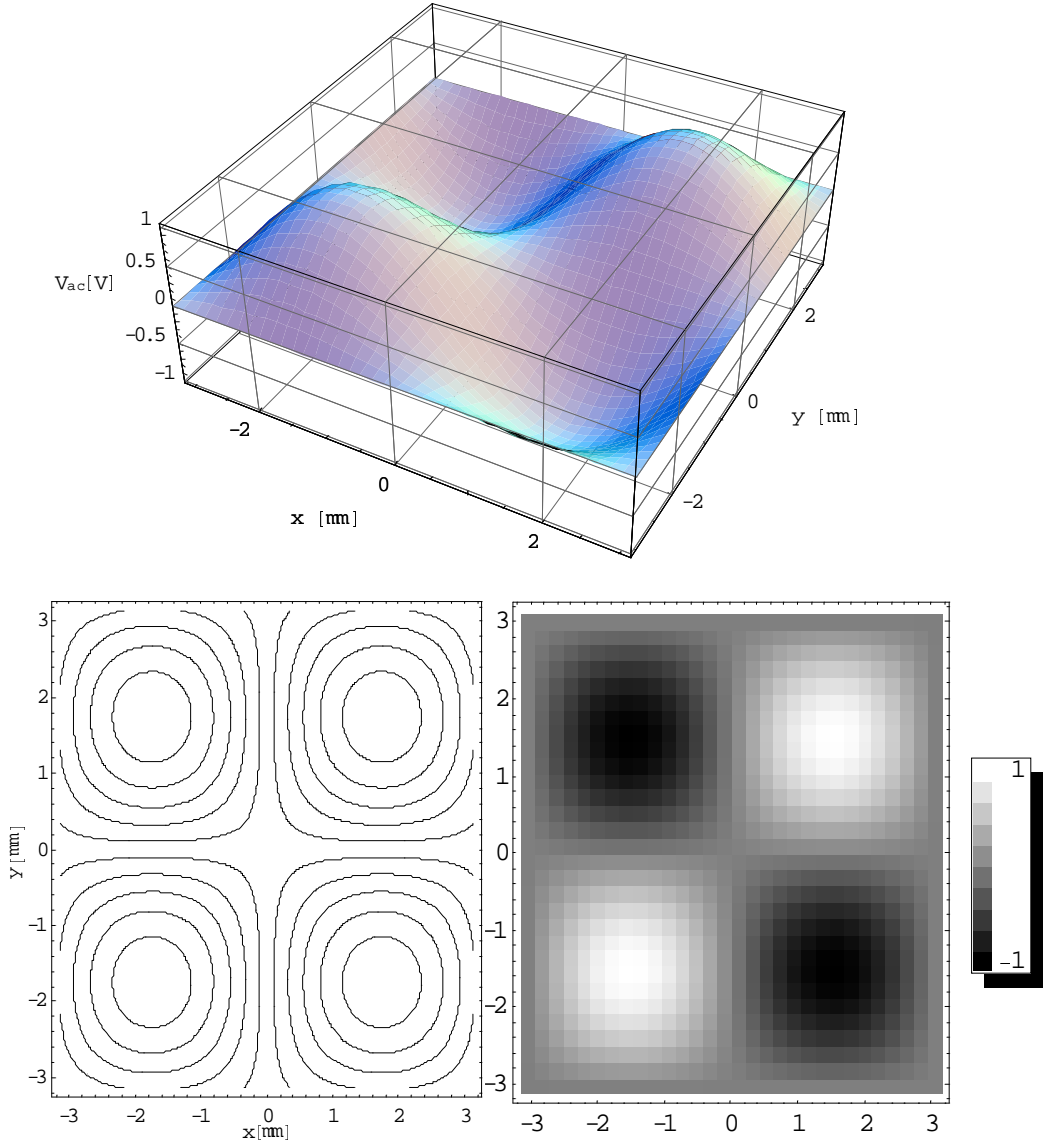


Fig. 5.26. The electric field inside the quadrupole system (only the alternating potential is shown).

Using this theoretical description an important feature of quadrupole fields is presented, namely their ability to create a phase-space-conserving image [114], e. g. they are able to focus all trajectories (see Fig. 5.27) starting from one point onto another point, which is a direct consequence of the harmonic electric potential. Additional aspects of focusing and results from trajectory calculations were reported by Dawson[115], although in none of these references experimental advantages have been presented. A more recent discussion on spatial focusing in an rf-only quadrupole was given by Miller [116] where pronounced transmission maxima and minima were observed as a function of the ion amplitudes.

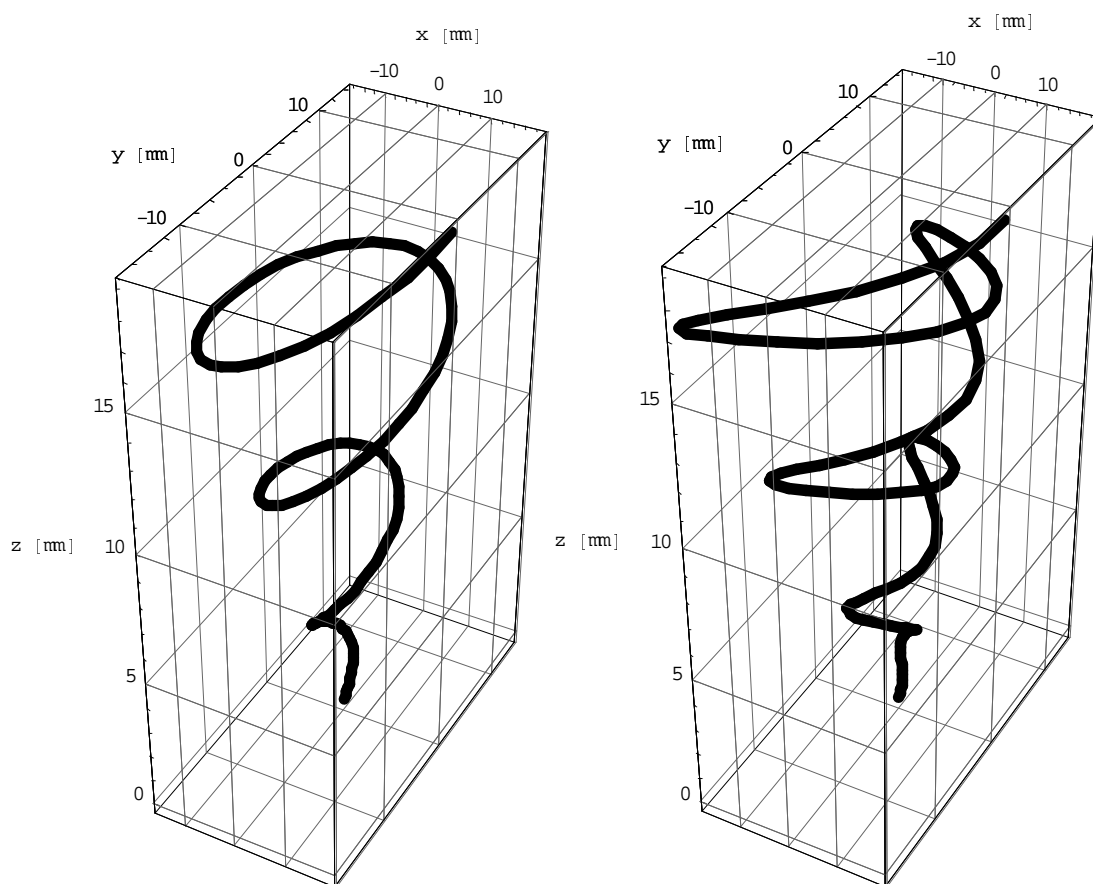


Fig. 5.27. Different particle trajectories inside a quadrupole ion trap.

Using this focusing characteristic of the quadrupole fields, it is clear that no phase synchronising circuit for particle injection is needed. The incoming particle stream will be focused to the centre of the system and also the applied DC potential

onto the tube electrodes, results in stable trapping of one or more particles as shown in Fig. 5.28.

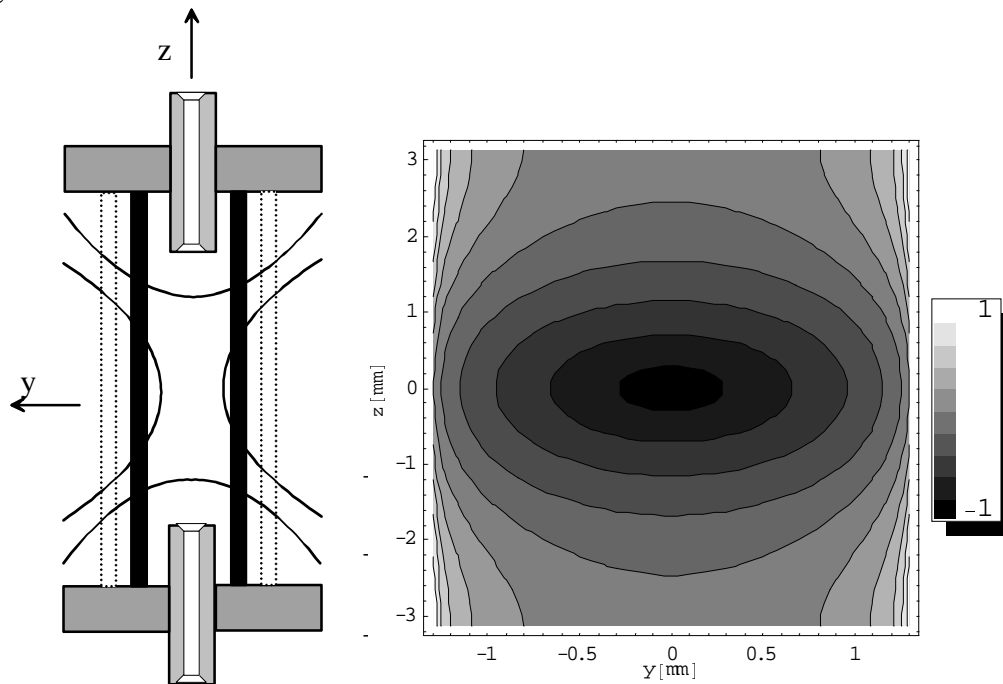


Fig. 5.28. The electric field inside the quadrupole system (a superposition of the AC and DC potential which form an parabolic potential well).

Discussion

In this chapter the process of particle charging by ions of one polarity was discussed. The constructed diffusion, field and alternating electrical field charging devices were presented from the mechanical and electrical point of view and characterised by measuring the electric charge acquired on a particle. The diffusion charger shows no substance dependence but the applicability is limited to small particles with diameters below $1 \mu\text{m}$. An improvement (increase) of the net charge with a narrow charge distribution was observed for the field charging device. Examining the charge time diagram it can be observed that just the positive half-cycle of the alternating potential is responsible for the ions present in the charging zone. This disadvantage was eliminated by the construction of the alternating field charger, for which the electric charge is near the Pauthenier limit avoiding also the particle precipitation on the electrodes.

The interaction between a charged particle and the electric potential was presented for different trapping systems. In order to characterise these systems, different calculations of the electric field and particle trajectory were performed. The performed theoretical simulations display a radical inconvenience in using the electrodynamic balance, like the strong influence of the supporting rods and the phase injection. This becomes much more important if the flow superposition is also considered (as mentioned in the previously presented chapters, the particles are brought into the system by flow suction). To overcome this handicap, two methods were proposed. From these two, just one has been realised: a quadrupole system which presents the ability to create a phase-space-conserving image or focusing property, has been built.

Chapter 6

Results and discussion

This chapter consists of two parts: describing the system for (i) single particle and for (ii) many particle investigation. The individual devices presented in Chapter 5 are now put together (see B.7). The time diagram and the selection criteria governing the entire process of retaining just one particle from a particle cloud, and the method for many particle investigation are presented and discussed. Finally the Raman results for both cases are presented.

6.1 Single particle investigation

Solid microparticles were generated using the methods described in the previous chapter. Standard microparticles with a size range between 1 and 10 μm sucked into the inlet are immediately splitted into a sample flow, through the inner tube, and a sheath flow through the external tube [117]. The sheath flow is filtered and both flows are controlled by the same pump using two valves. After passing through the tubes the sample flow is reunited with the sheath flow. This second flow confines the sample particles to the center of the system (for a better confinement of the microparticles it was necessary to use a sheath flow 4 or 5 times higher than the sample flow), and introduces them into the charging device [118].

Microparticles charged by diffusion [84] or by field charging [85-87], were measured with the method described by Kasper [24]. The obtained values show a linear dependence between the particle charge and particle diameter for diffusion charging and a square dependence for field charging. Once the particles have an electric charge, they can interact with the electric potential applied on the quadrupole electrodes.

In the experiment described here two identical stages of linear quadrupole types were used (see B.4). The trapping system consists of four steel rods and two tubes. For reducing the air flow perturbation from the chamber, the quadrupole device was installed in an enclosure (a glass tube) to protect the particle stream. The tube electrodes are supplied with a DC voltage (0-1000 V) usually of opposite polarity for vertical stabilization of the charged particles. The other four electrodes have an AC voltage (0-7000 V) necessary for stabilising the microparticle radially in the center of the system [113]. The frequency of the AC potential can be varied between 30-1500 Hz. The studied particle trajectories are relatively insensitive to the choice of the AC potential and frequency. Generally, more than one particle can be trapped at a time. Because we are interested in one particle investigations, further manipulation of the DC/AC voltage and AC frequency, results in a stable trapping of a single particle.

An argon ion laser (Spectra Physics) operating at 514 nm was used as Raman excitation laser. This 514.5 nm line provides the highest intensity available, maximising the Raman signal. A plan-convex cylindrical lens, with a focal length of 60 mm, was used to focus the beam before entering the quadrupole. Normally, Raman spectra were taken using a back scattering geometry which assures a maximum detection of the scattered radiation. An alternative way to record the Raman spectra is a 90° scattering geometry as shown in Figure 6.1. In this case a spherical mirror was used to avoid the deflection of the particle which occurs when high laser intensities are used.

A lens collection system is sending the inelastically scattered light to a monochromator. The collection system consists of two equiconvex lenses (or just a simple system composed of one lens as presented in Figs. 6.1 and 6.5), with a focal length of 50 respectively 80 mm. The laser beam was aligned to the focal point of the lens system and the particles were moved into the illuminating light by manipulating some micrometer stages.

A Spex 1404 double monochromator (focal length 0.85 m, 2400 lines/mm) was used to separate the wavelengths of the scattered light. The monochromator was controlled both manually and by computer through a Spex CompuDrive CD2A. There

were also two exit ports for the dispersed light, but they could not be accessed simultaneously.

The spectra were recorded by a liquid-nitrogen cooled CCD camera (Photometrics Ltd.) mounted in a backscattering direction. CCD's are usually fabricated using metal-oxide-semiconductor technology with the front side covered by a silicon-oxide layer isolating the polysilicon gate structure from the p-silicon substrate. These gates are arranged in an array of a few hundreds columns and rows. The pixels are read out after exposure and generate a certain number of counts depending on the brightness of the incoming radiation. A computer adds the data of the pixels to a picture. The application of CCD camera make possible the radial resolution in two dimensions on the micrometer scale.

With these components, recording of single-shot or integrated spectra (to improve the signal to noise ratio) is possible.

The experimental setup is presented in Figure 6.1 and the time sequence is illustrated in Fig. 6.2.

Initially the DC and AC potentials are applied onto the electrodes. At the starting point the first magnet valve V1 is open, while the second magnet valve V2 is closed. Particles are introduced into the system directly by flow suction through the sample inlet (pp. 69) and charger (one of them exposed in Chapter 5). As a function of their charge and the applied potential on the electrodes, some particles will be trapped in an upper position of the DC1 (see Fig. 6.1) electrode, the others particles that have not the optimal physical parameters (electric charge and mass) are removed from the system through a hole located in the continuous voltage electrode, avoiding the contamination of the second quadrupole.

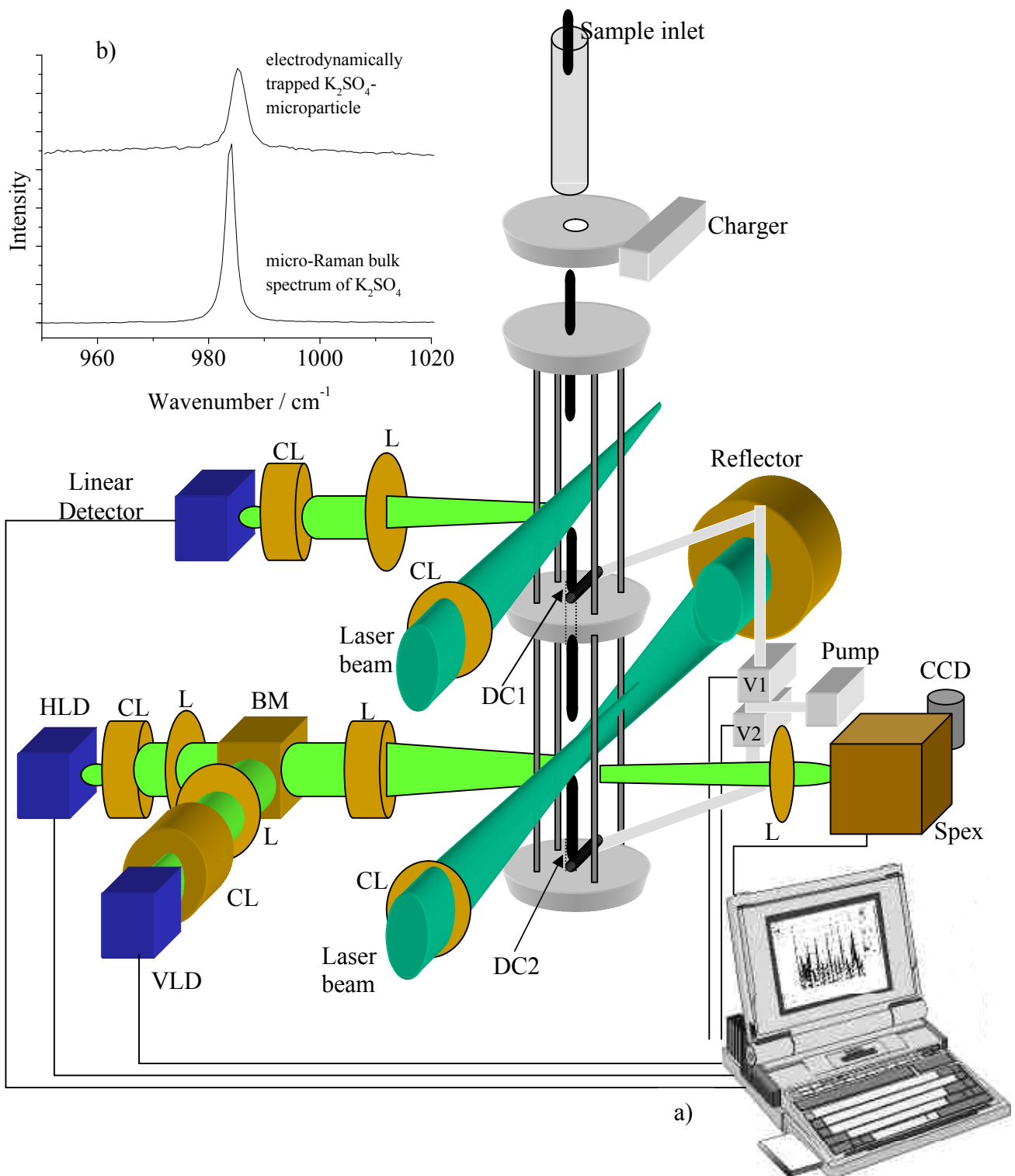


Fig. 6.1. a) The developed experimental setup where: L - normal convergent lens; CL - cylindrical lens; BM beam splitter; V1 and V2 are the first and second magnetic valves; DC1, DC2 are the continuous voltage electrodes corresponding to the first and second quadrupole; CCD charge coupled device; Spex: double monochromator; HLD and VLD are a linear detectors (TSL 215) orientated in an horizontal respectively vertical plane, see also B.5. b) Left part upper, a recorded Raman spectra of one particle and as reference the bulk signal.

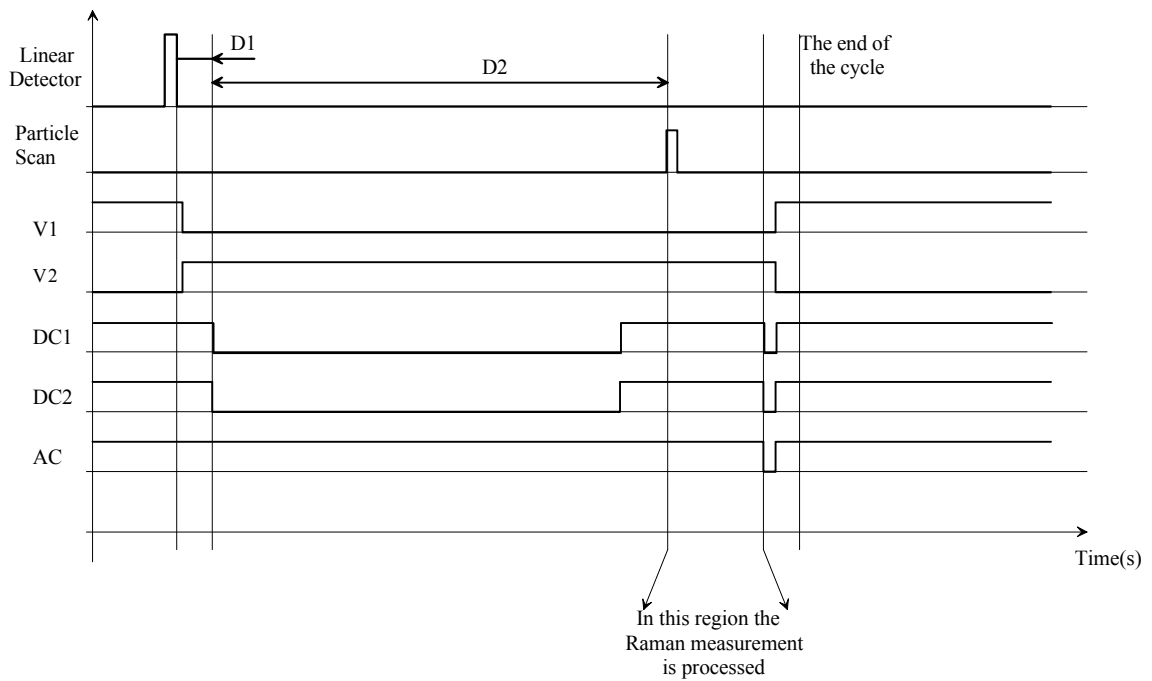


Fig. 6.2. The time diagram used for the system.

By illuminating the trapped particles with a laser passing through a cylindrical lens an optical signal is generated. An linear detector (see Fig. 6.1 and 6.3) transforms this optical signal in an electrical one which can be further processed.

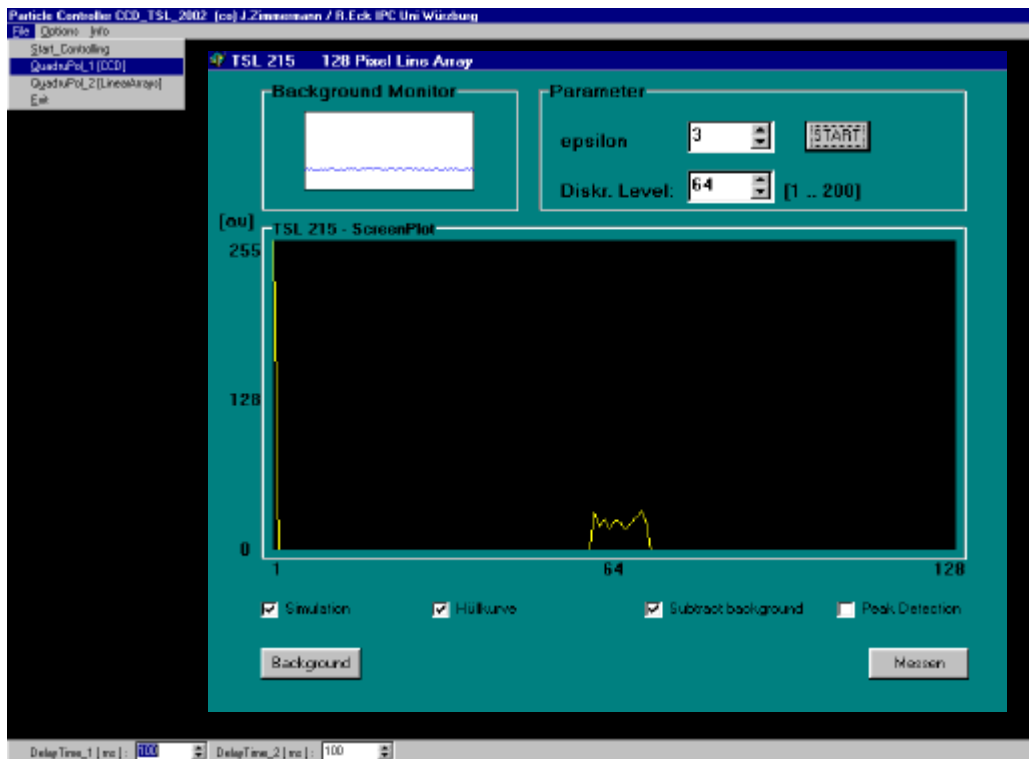


Fig. 6.3. The obtained information from the first quadrupole after background elimination.

The electrical signal generated from the CCD-Array starts our developed program for a reduction of the particle number. After a delay time of 20 ms when the valves are changed (valve V1 will be closed correlated with the opening of the V2 valve) the DC potential is reduced to 0V in order to facilitate the injection of the particles into the second quadrupole Q2. For keeping the system as simple as possible the same potential source for the DC1 and DC2 electrodes was used. Therefore, it was necessary to use a delay time D1 which is the time interval after which a 0 volt potential is applied on the DC1 electrode (also DC2).

The particles are now in the second quadrupole. Since the investigation of the moving particles can perturb the running program, a second delay D2 (placed in the bottom part of the program, as also D1) was introduced between the DC rehabilitation and the starting moment of the Part_Scan (a routine in the entirely developed program for the automatisisation of the process).

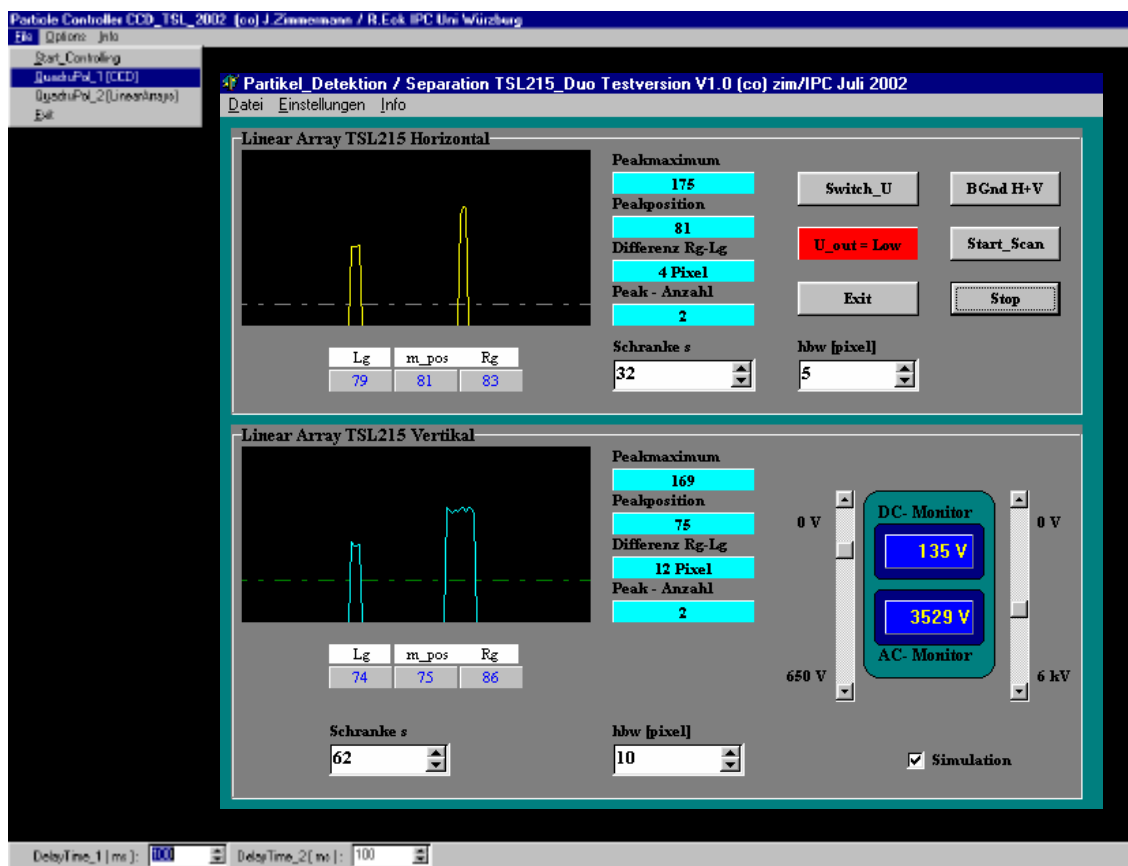


Fig. 6.4. The main part of the program, Part_Scan which selects just a single particle from a particle cloud as a function of the discrimination level (“Schranke”), peak number (“Peak-Anzahl”) and peak halfwidth (“blw[pixel]”).

The Part_Scan routine (shown in Fig. 6.4) uses the information obtained from both the HLD (linear detector orientated horizontal) and VLD (linear detector orientated vertical) detectors (TSL 215 detectors with 128 pixel length). As a function of different criteria (peak intensity, width, stability obtained from both detectors) the DC, AC voltage and the frequency are changed (reduced/increased) in such a way that just one single particle from a particle cloud is trapped and levitated. This one single particle can be investigated by Raman spectroscopy [119, 120] as shown in the upper part of Fig. 6.1 (we used K_2SO_4 or TiO_2 particles; or other particles in the crystalline state which usually exhibit characteristic Raman frequency shifts with a narrow bandwidth). In the last step the DC voltage is driven to a lower value in order to remove the investigated particle from the second quadrupole. Finally the cycle is close when all the instruments are driven to the initial condition.

6.2 Many particle investigation

The basic idea for this experiment is similar to that presented for the single particle experiment. Differences to the exposed setup, appear just in the domain of particles manipulation (see Fig. 6.5).

The developed Part_Scan_1 routine (which is almost identical to the Part_Scan for single particle investigation) uses the information obtained from the HLD (horizontal linear detector) and as a consequence of different criteria the AC voltage and the frequency are changed in such a way that the particles are constrained to the center of the system and form a stream (see B.6). For this purpose the scattered light passes through a system made of a equiconvex and a cylindrical lens resulting in a narrow line of light. The line width shows the displacement of the particles from the center of the system, viewed in a radial direction and it can be influenced by modifying the AC potential. The line intensity is correlated to the particle radial oscillations, and can be attenuated by acting on the AC frequency. By manipulating these two parameters and considering the presented method an algorithm for transformation of a particle cloud to a stream can be built. The information obtained from the VLD (vertical linear detector constructed into an identical optical system as described for the HLD) is applied to take the Raman spectra. In this case a linearity between the HLD indication (peak position) and the CCD detector has been found, as shown in Fig. 6.6.

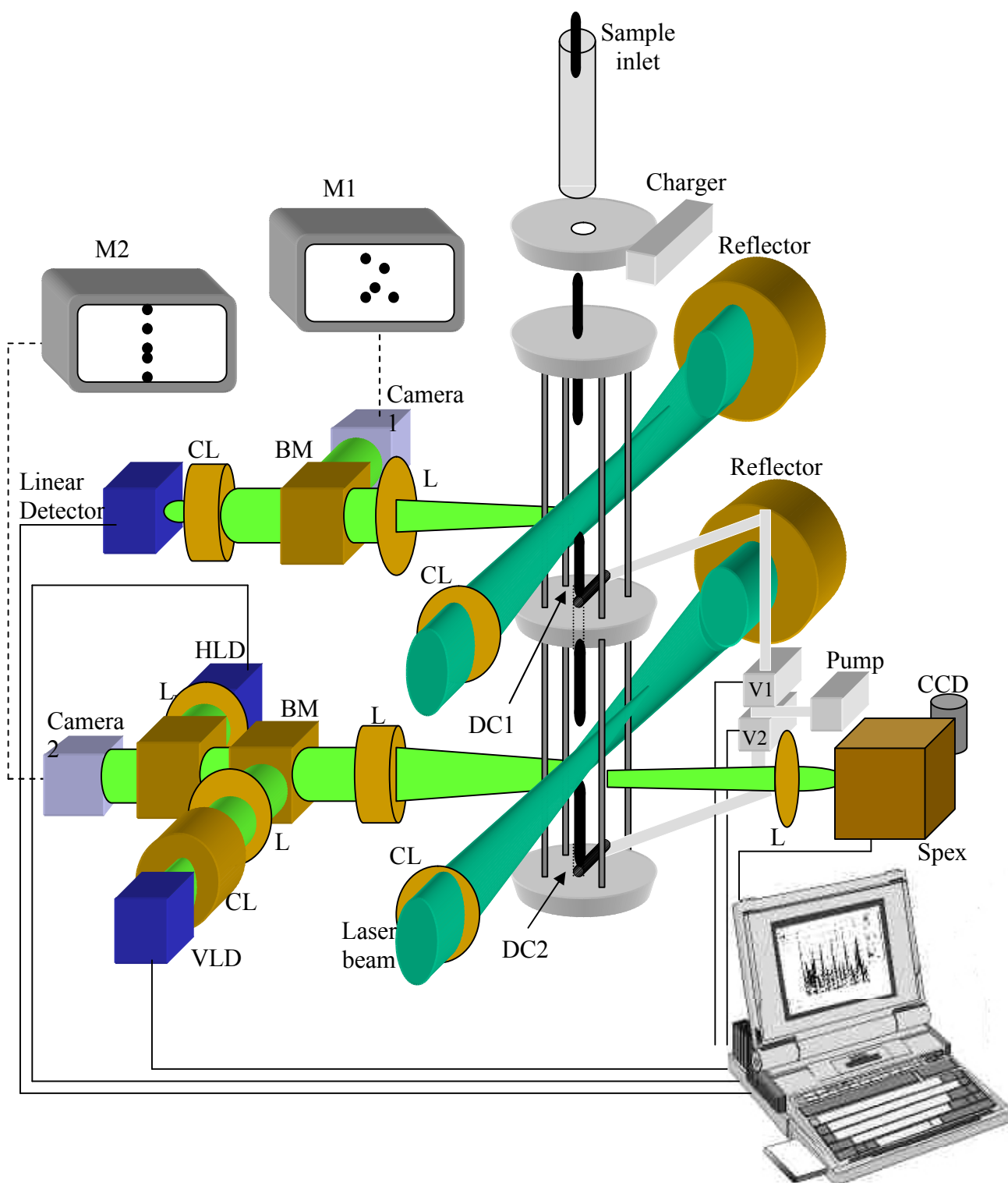


Fig. 6.5. The developed experimental setup where the symbols: L normal convergent lens; CL cylindrical lens; BM beam splitter; V1 and V2 are the first and second magnetic valve; DC1, DC2 are the continuous voltage electrodes corresponding to the first and second quadrupole; CCD charge coupled device; Spex: double monochromator; M1 and M2 two monitors for particles observation; HLD and VLD are linear detectors orientated in an horizontal respectively vertical plane.

Using this linearity, a subroutine which automatically divides the CCD detector and also includes the possibility to drive the DC potential for a better adjustment of the particle stream to the CCD, can be built. In this case the CCD detector is divided using the processed optical information obtained from the VLD as a function of peak position and half width, resulting in an equal number of tracks. The track lengths on the radial (or r) direction are equal, while the vertical (or z) dimension is different and proportional to the half width of the peak. The particle stream was investigated by Raman spectroscopy using the presented track properties.

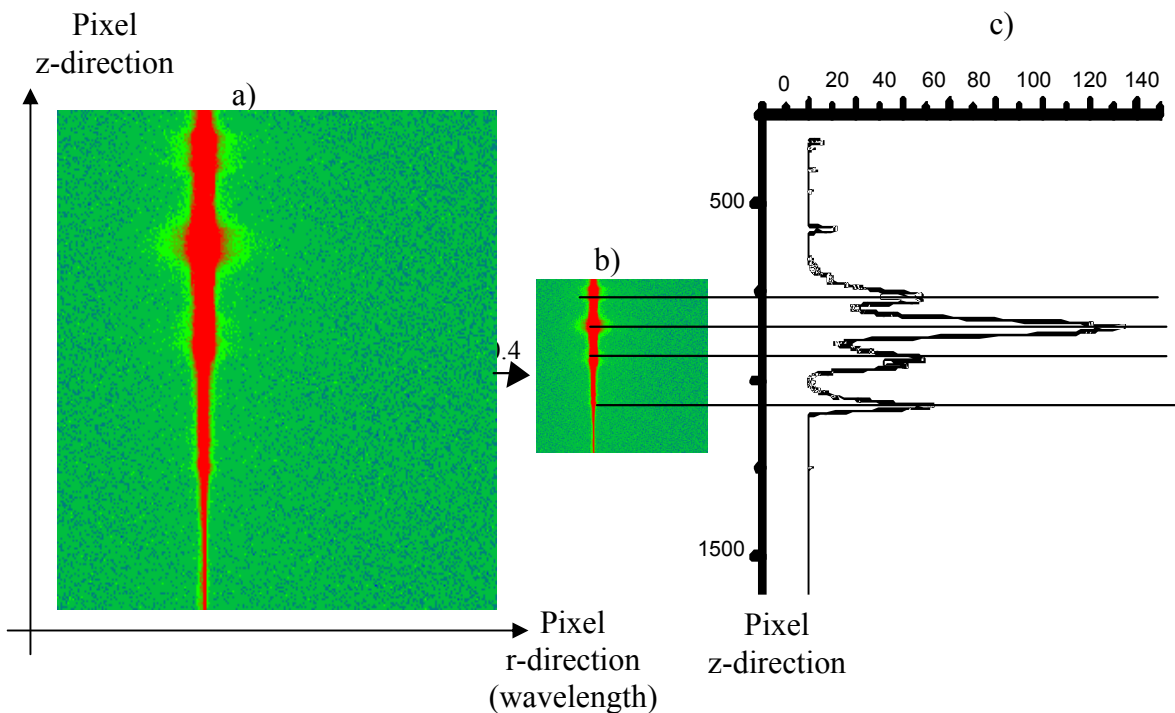


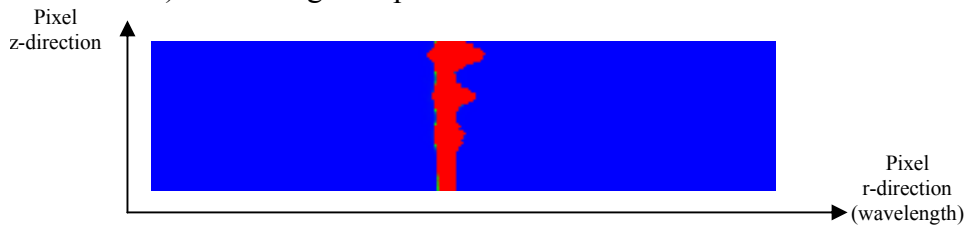
Fig. 6.6. The linearity between the VLD indication and the built image of the particle stream on the nitrogen cooled CCD, (a) the CCD image of four particles measured near the excitation line, (b) the same image but scaled with a factor of 0.4, (c) the information obtained from the external detector (VLD) proving that a linear dependence between the exposed signals was found (from the technical point of view this means that once the dependence is found, the Raman measurements can be performed just by using the external information - VLD) and used for track generation.

The spectral results obtained with the instrument are presented in Figs. 6.7-6.9. The different Raman spectra for two or more particles were recorded with an integration time of 10 minutes. To test the technique, different mixtures were used: (a) inorganic (TiO_2) and inorganic (K_2SO_4); (b) inorganic (K_2SO_4) and organic (banana-shaped

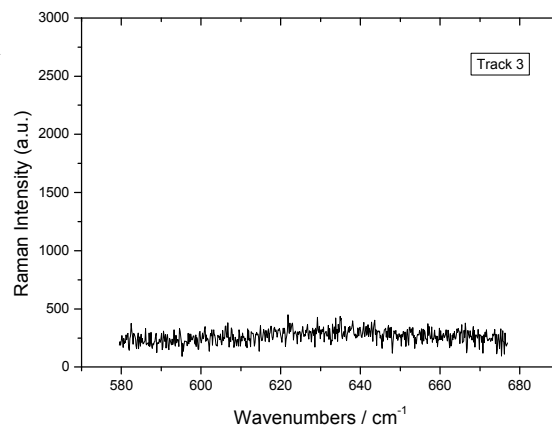
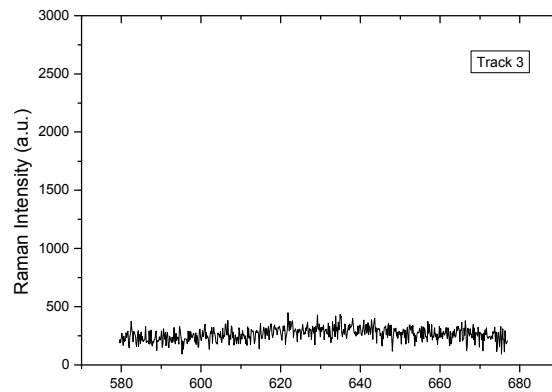
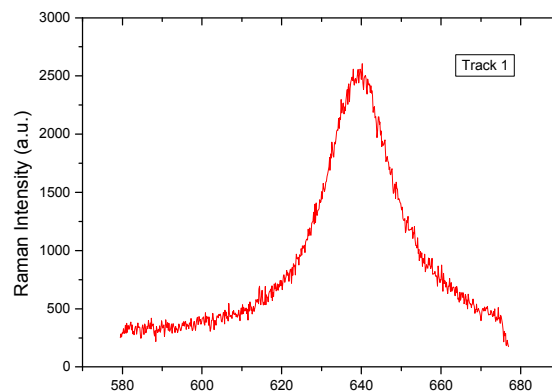
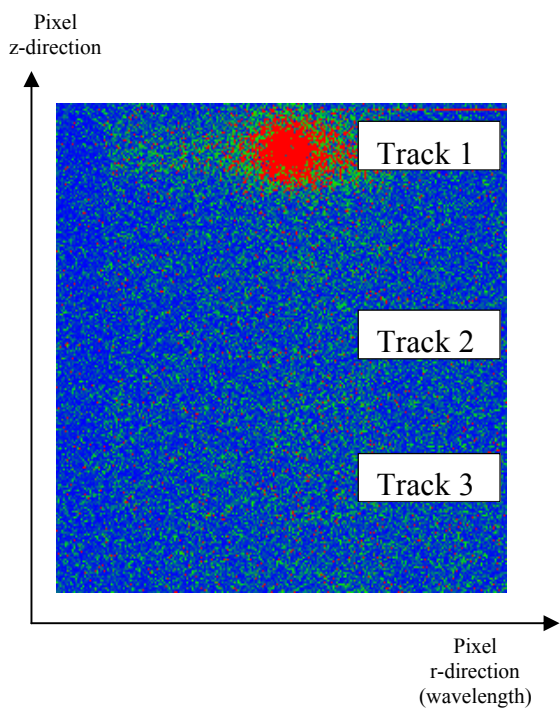
compound based on monoaromatic ring); (c) inorganic (TiO_2) and biologic (pollen). The Raman spectra for these substances are well known, so no further evaluation in order to identify the observed Raman bands needed to be carried out.

TiO_2 and K_2SO_4 mixture (inorganic and inorganic)

a) CCD Image – 3 particle at 20 cm^{-1}



b) 640 cm^{-1} (TiO_2 particle)



c) 985 cm^{-1} (K_2SO_4 particle)

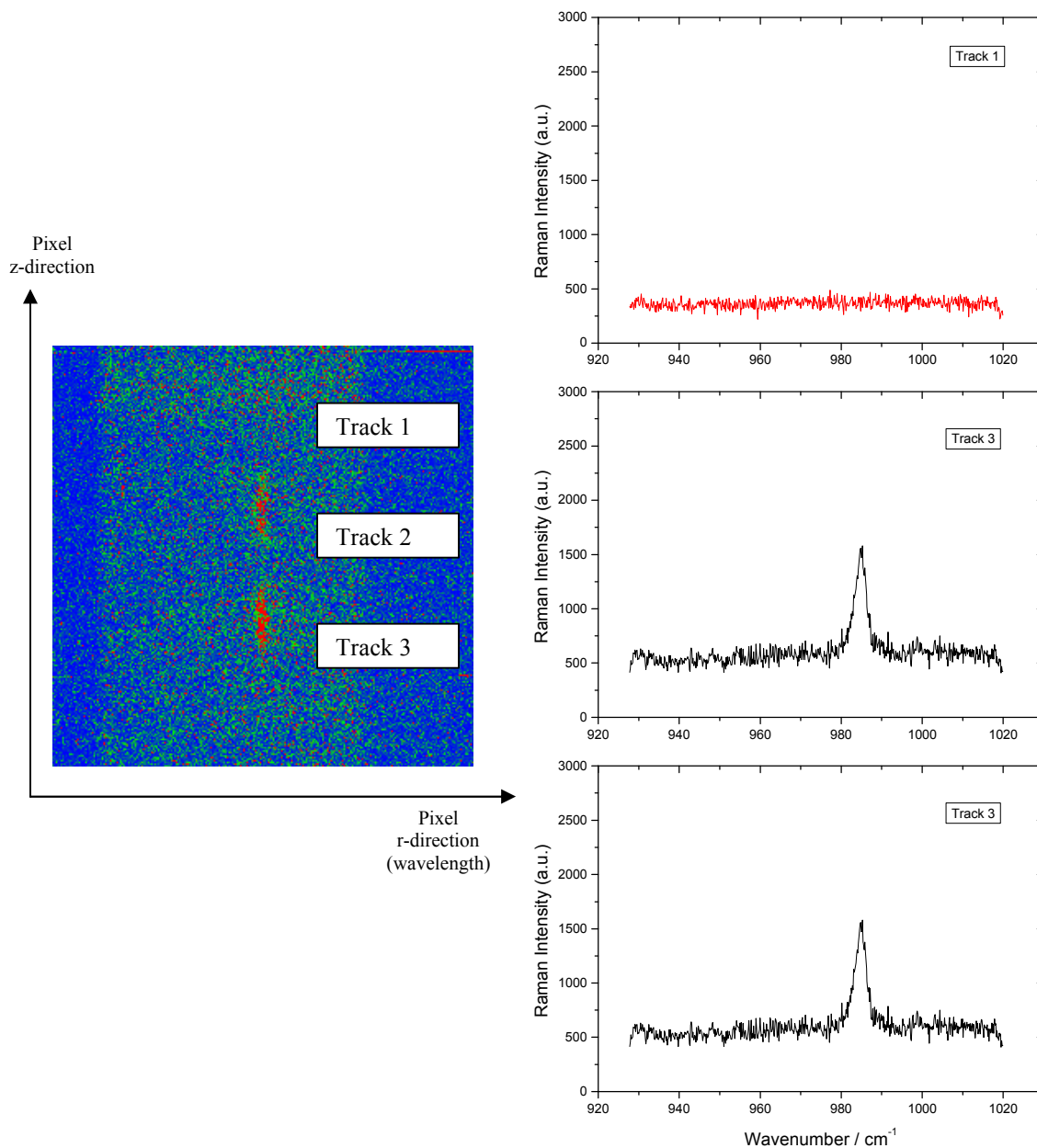


Fig. 6.7. Raman spectra for an inorganic/inorganic mixture: a) shown a CCD image (dimensions are like in Fig. 6.6, pixels) of a group of three particles taken at 20 cm^{-1} from the excitation line; b) on the left side the CCD image of these three particles while on the right side the recorded single shot spectra obtained for each track at 640 cm^{-1} and proving the presence of one TiO_2 particle on first track; c) similar to b) Raman measurements at 985 cm^{-1} shown that two K_2SO_4 particles are trapped in the system corresponding to the positions of track 2 and 3.

During the measurements the track positions and dimensions are constant.

TiO₂ and banana-shaped compound mixture (inorganic and organic)

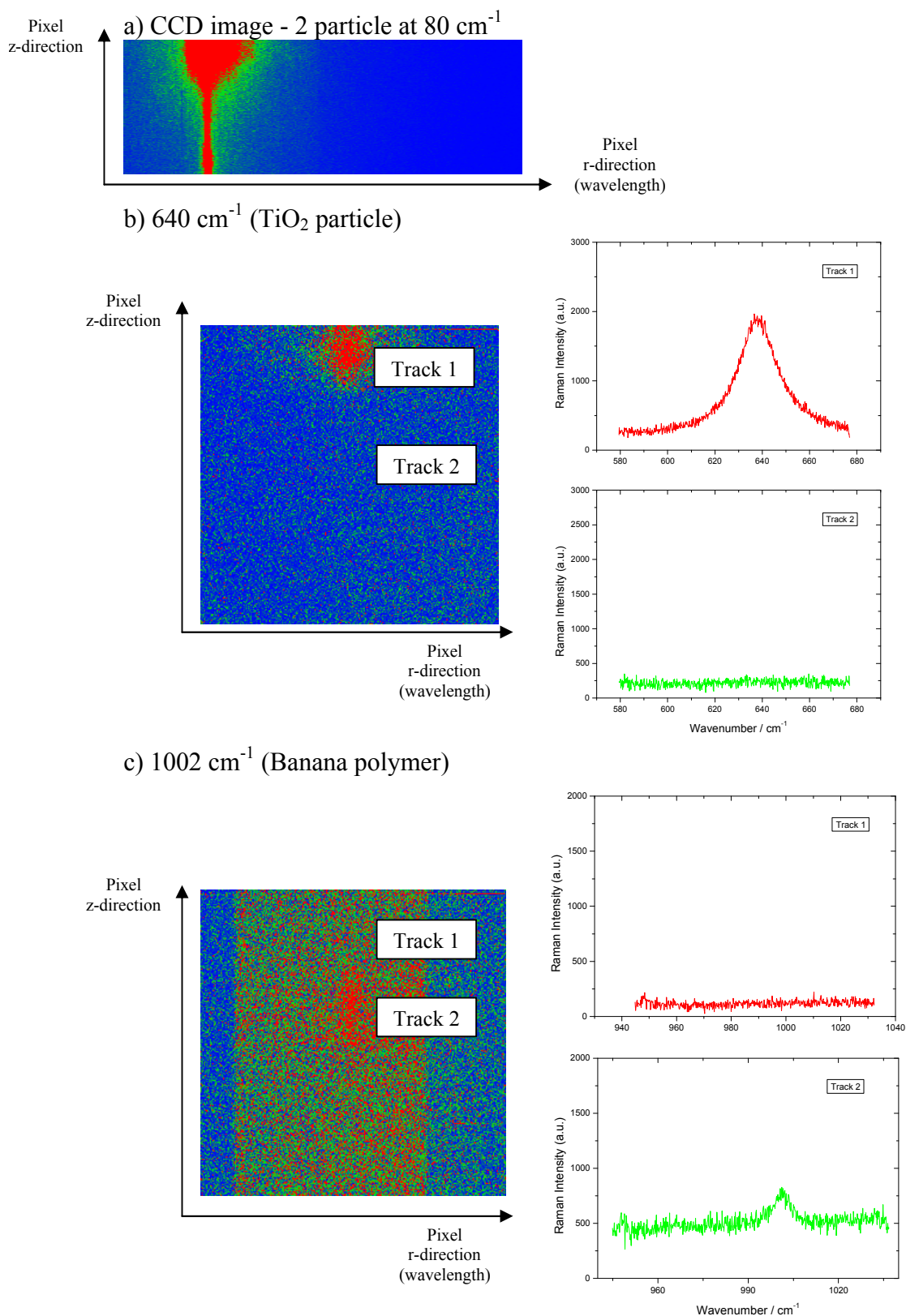


Fig. 6.8. Raman spectra for an inorganic/organic mixture: a), b) are similar to that presented in Fig. 6.7; c) shown the presence of the monoaromatic ring (1002 cm⁻¹) in the banana-shaped compound.

TiO₂ and pollen mixture (inorganic and biologic)

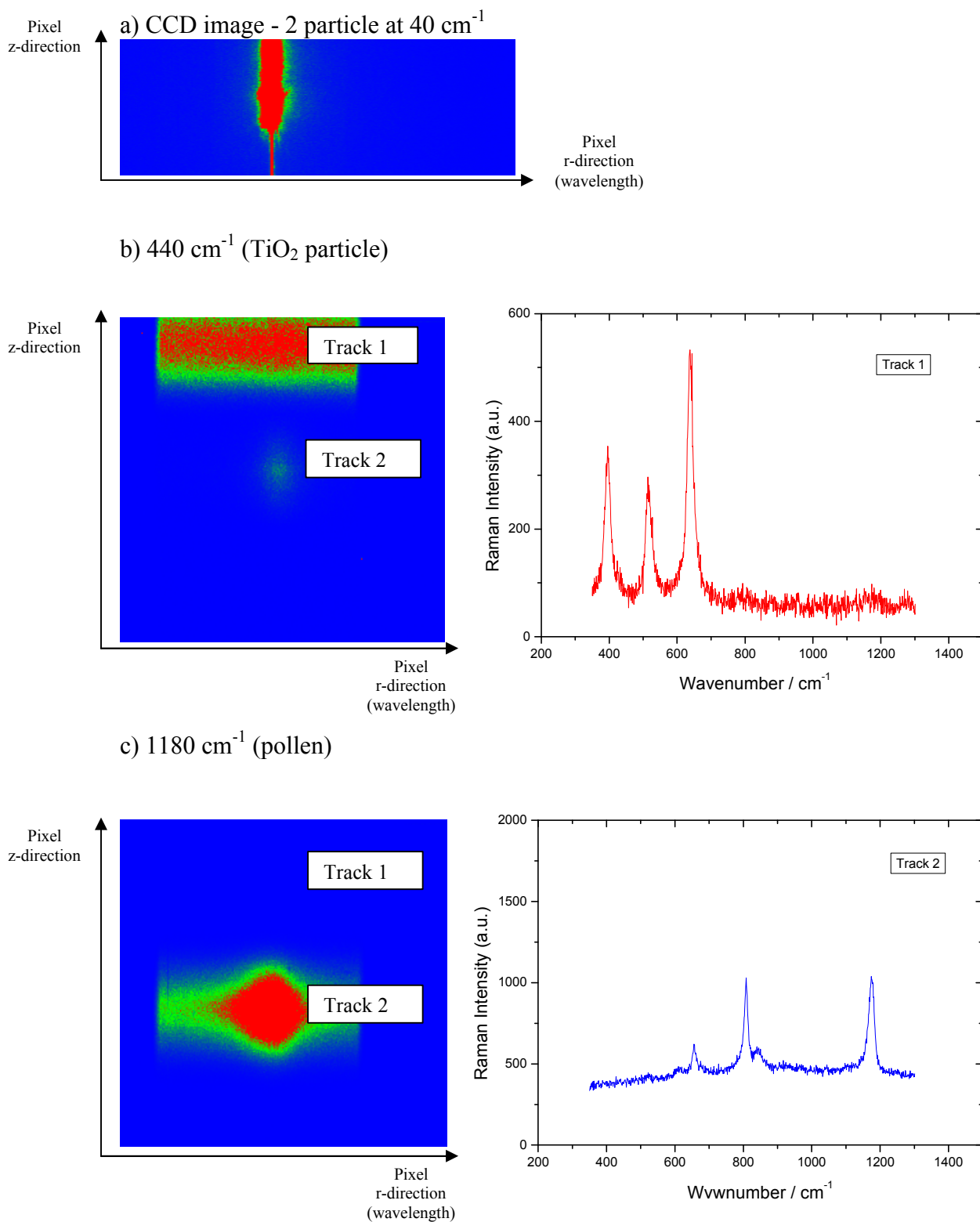


Fig. 6.9. Raman spectra for an inorganic/biologic mixture: a), b) are similar to that presented in Fig. 6.7; c) shown the presence of the biological compound (1180 cm⁻¹) in system.

6.3 Discussion

In the first part of this chapter, a method and an experimental setup for solid particle injection in a quadrupole trap near atmospheric pressure was described. The method is nondestructive due to the optical investigation method. Using this system the manipulation of the particles from one quadrupole to another and also the selection of just one particle from a particle cloud can be achieved.

In the second part, the method presented before was extended for the investigation of many particle. The technique shows a large range of applicability on: inorganic, organic and biologic substances. Using this method the particles are moved from one quadrupole to another and transformed from a cloud to a stream.

From the preliminary results we have observed that the presented systems show an improvement of the radial stability and a great feasibility for minimisation.

For both cases Raman measurements were performed.

In the first experiment, as illustrated in Fig. 6.1, it was demonstrated (examining the sulfate stretching vibration $\sim 985 \text{ cm}^{-1}$) that microparticle Raman signals don't differ significantly from bulk samples regarding the frequency shift. Differences appear for intensity and line half width. These can be explained as follows: (i) the intensity is lower because the light flux radiated per solid angle is lower (see eq. 4.4 which shows that the Raman scattering is a volume effect) and (ii) the change in the line width is a direct consequence of the particle size (as the size decreases the number of the dangling bonds on the surface increase and become significant). A stronger difference would be expected for liquid particles, when the optical resonance effect must be considered.

In the second experiment (Fig. 6.5), Raman spectra (Figs. 6.7–6.9) for different substances were recorded. The measurements allow us to identify the characteristic Raman bands, e.g., for TiO_2 .

B_{1g}	$A_{1g} + B_{1g}$	E_g
398/15	516/18	638/20

Table 6.1. Peak position and FWHM's (full-width at half maximum) of the B_{1g} , $(A_{1g} + B_{1g})$, E_g modes of anatase TiO_2 .

The Raman and micro-Raman techniques are useful methods to detect the phase composition, spatial inhomogeneity and morphology changes of TiO_2 . Raman spectra are also sensitive to the small amount of other impurities on the external surface of anatase TiO_2 . The low absorption level (typical for the Raman process) of the laser excitation source should allow us to estimate the surface components on TiO_2 .

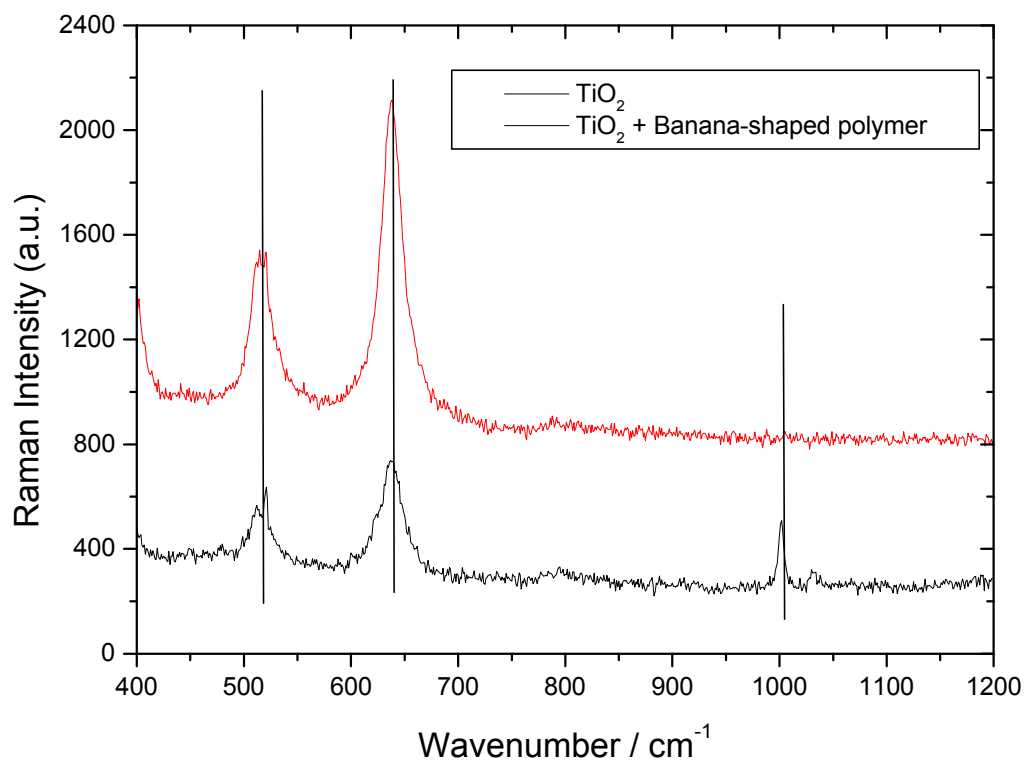


Fig. 6.10. The Raman spectra of TiO_2 (red) and banana-shaped polymer concentrated on TiO_2 particle (black). The position of the Raman bands correspond to that presented in previous Figs. 6.7 and 6.8.

Therefore, structural inhomogeneity, such as banana-shaped polymer concentrated on the surface of anatase particles, can be detected using Raman spectroscopy as illustrated in Fig. 6.10.

Chapter 7

Final discussion and conclusions

This thesis is concerned with the development of an on-line in-situ device for a chemical characterisation of flowing aerosols. The thesis describes the principles and most important features of such a system, allowing also on-line measurements using Raman spectroscopy as a diagnostic technique. Using the presented results a commercial instrument can be build. Applications of the developed techniques include experiments with single or many particles.

However, these goals could not be achieved without considering some fundamental aspects of particle dynamics in fluids or electric fields, particle charging and particle electrodynamic containment.

7.1 Summary

An analysis of the effect of forced oscillations on the motion of the particle dispersed in a gas flow is given in **Chapter 2**. Also the most important particle parameters are introduced. A review of the particle/fluid interaction in laminar air flows and the response of the particle is presented. When external oscillating electric fields are used to induce a transverse particle motion, it is shown that AC frequencies below the reciprocal of the relaxation time of the particle must be selected. The analysis indicates that a high level particle charge should be acquired in order to compensate the Coulomb forces.

In **Chapter 3** the behaviour of the particle under different external conditions (ion bombardment and electric fields) is extended. A brief review of the most important particle charging theories (diffusion, field, and alternating potential charging) shows, that the effect of the electrical properties (represented by the dielectric constant) of the particles affects the charging process. A non-contact method for particle charge measurement was also presented.

In the second part of the chapter, the interaction between the electric field and the charged particle for the purpose of particle trapping is illustrated. The most common systems like the two or four ring electrodynamic balance and the quadrupole trap are pointed out.

In **Chapter 4** a short review of the possibility of using scattered light to study aerosol particles is presented. First, the conditions and the facilities of using the Mie theory for particle size and refractive index determination are mentioned, then some features concerning the classical treatment of the Raman effect are presented. Based on these theoretical considerations the measurements were performed in an 90° degree geometry using the 514.5 nm line of an argon ion laser for excitation.

Supported by the theoretical considerations exposed in Chapter 2, 3, and 4 the construction and the tests of different devices are presented in **Chapter 5**. Following the goal of the thesis, first an overview of the used materials and methods for particle generation is presented. Then, the constructed charging devices are described (from the mechanical and electrical point of view) and compared by measuring the acquired charge on the particle. As a function of this measured charge and furthermore taking into account the higher ratio of particle losses by the diffusion and field charger, the AC charger is adapted to the required queries.

Charged particles can be trapped in different containers. Two types of axially symmetric electrodynamic balances (two ring or an extended four ring configuration) were presented. For a deeper understanding these systems were studied using analytic and numerical methods. A theoretical description of the trapping systems and the particle motion inside them is given in the terms of the Mathieu equations. An important behaviour regarding the particle motion inside an electrodynamic balance has been observed. The simulated trajectory and the calculated probability to find a particle in one position in the system shows that the phase injection f plays a crucial role in the trapping process. From these simulations it can be concluded that the injection of the particle at a random phase will cause a loss of the particle. This disadvantage can be

overcome either by placing a phase synchronising circuit between the AC ring electrodes and the particle input, or by using an appropriate geometry for the trapping system for which the phase of the alternative potential will not present this strong dependence.

Considering the presented purpose of the work another type of trapping system has been developed, namely the quadrupole trap. A similar theoretical characterisation (in term's of Mathieu equation) as for the electrodynamic balance was presented pointing out some specific features of this system. One of the most important characteristics is the ability of quadrupole systems to create a phase-space-conserving image, e. g., they are able to focus all trajectories starting from one point onto another point. Using this focusing characteristic of the quadrupole fields, it is clear that no phase synchronising circuit for particle injection is needed. The incoming particle stream will be focused to the centre of the system simultaneously also the applied DC and AC potential onto the tube electrodes, yields a stable trapping of one or more particles.

Chapter 6 consists of two parts: the system for single particle and for many particles investigation. The individual devices presented in Chapter 5 are now put together. The first part presents the method and the experimental realisation of a set-up for solid particle injection. In order to suppress the phase injection disadvantage found for the electrodynamic balance a developed program processes the information obtained from a particle cloud through an adequate electronic detection system, and reduces the number of particles until just one single particle is trapped.

The method for one particle investigation can be extended for many particles. Using the presented set-up the particles are moved from one quadrupole to another and transformed from a particle cloud to a particle stream. A linearity between an external vertical mounted detector and the formed image of the particle stream on the CCD camera has been observed and used for simultaneous detection of many particles by Raman spectroscopy.

For both methods Raman results are presented.

One limitation of Raman Spectroscopy is the relatively long integration time needed for adequate signal-to-noise ratio. There are two factors which influence the integration time: first the incident radiation and the detector sensitivity, and second the intensity of the Raman bands. Using a CCD detector, the desired detector sensitivity should be achieved. So, the improvement of the signal-to-noise ratio should be the next

goal in the system development. In order to reduce the integration time an optical system including optic fibres and the integration of an FT-Raman [121] module operating in the visible region is planned.

The goal of this work was to develop and construct an instrument for on-line in-situ single particle investigation by Raman spectroscopy. With the presented experimental set-up and the developed program the purpose of the work, the on-line in-situ near atmospheric pressure aerosol investigation was achieved. The Raman spectroscopy has been used successfully for a chemical characterisation of the aerosol particles.

7.2 Zusammenfassung

Diese Arbeit beschäftigt sich mit dem Aufbau eines *on-line in-situ* Analysegerätes zur chemische Charakterisierung von Aerosolen in Luftströmungen. Die Arbeit beschreibt neben den Grundlagen die wichtigsten Eigenschaften eines solchen Systems für *on-line* Messungen, das die Raman-Spektroskopie als eine Diagnosetechnik einsetzt. Die vorliegenden Ergebnisse ermöglichen den Aufbau eines kommerziellen Messgerätes. Die Anwendungen der entwickelten Technik beinhalten Experimente mit nur einem oder mehreren Partikeln.

Diese Ziele konnten nur unter Berücksichtigung einiger grundlegender Aspekte der aerodynamischen Teilchendynamik bzw. Bewegungsdynamik der Partikel in elektrischen Feldern sowie der Teilchenladung erreicht werden.

Kapitel 2 beinhaltet eine Analyse der Effekte von erzwungenen Oszillationen auf die Bewegung dispergierter Teilchen im Gasfluss. Dort werden auch die wichtigsten Eigenschaften von Partikeln vorgestellt. Es wird ein Überblick über die Teilchen-Gas Wechselwirkungen in laminarer Strömung gegeben, und die Reaktion des Teilchens in Abhängigkeit von Veränderungen (Kräften) werden diskutiert. Im Falle eines oszillierenden elektrischen Feldes, das eine transversale Teilchenbewegung bewirkt, wird gezeigt, dass bei AC-Wechselstrom Frequenzen unterhalb des Kehrwerts der Relaxationszeit gewählt werden müssen, um die Teilchen zu fangen. Die Analyse zeigt, dass ein hoher Wert von Teilchenladungen erreicht werden muss, um die Coulombkraft auszugleichen.

In Kapitel 3 wird das Verhalten von Teilchen unter verschiedenen externen Bedingungen (Ionenbeschuss oder elektrisches Feld) weiter erörtert. Ein kurzer Überblick über die wichtigsten Theorien zur Teilchenladung (Diffusions-, Feld-, und alternierende Potentialaufladung) zeigt, dass die elektrischen Eigenschaften (dargestellt durch die dielektrische Konstante) des Teilchens den Ladungsprozess beeinflussen. Darüber hinaus wird eine kontaktlose Messmethode für die Ladung der Teilchen diskutiert.

Im zweiten Teil des Kapitels wird die Wechselwirkung zwischen dem elektrischen Feld und dem geladenen Teilchen erläutert, zu dem Zweck, dass man die

Teilchen "einfängt". Die gängigen Systeme wie z.B. die elektrodynamische Waage mit zwei oder vier Ringen und die Quadrupolfalle werden ebenfalls diskutiert.

In **Kapitel 4** werden die Möglichkeiten zur Untersuchung von Teilchen durch um Analyse des gestreute Lichts vorgestellt. Zunächst werden die Bedingungen und Möglichkeiten für die Eignung der Mie-Theorie zum Studium von Partikelgröße und Brechungskoeffizient diskutiert; des weiteren wird auf die Eigenschaften des klassischen Raman-Effektes eingegangen. Aufgrund dieser theoretischen Überlegungen wurden die Messungen in einer 90° Geometrie mit Hilfe eines Argon-Ionen-Lasers mit einer Anregungswellenlänge von 514.5 nm durchgeführt.

In **Kapitel 5** wird die Konstruktion und anschließende Erprobung von Geräten beschrieben. Der Aufbau dieser Geräte erfolgte mit Hilfe der theoretischen Erwägungen aus den Kapiteln 2, 3 und 4. Es wird ein Überblick über die verwendeten Materialien und Methoden für die Teilchenerzeugung gegeben. Dann werden die entwickelten Ladegeräte beschrieben (vom mechanischen und elektronischen Standpunkt aus gesehen), und sie werden untereinander verglichen, indem die erzielte Ladung auf den Teilchen gemessen wird. Durch diesen Vergleich und unter Berücksichtigung der größeren Teilchenverluste in den Diffusions- und Felddaufladern wurde die alternierende Potentialaufladung den gewünschten Bedingungen angepasst.

Geladene Teilchen können in verschiedenen Anordnungen gefangen werden. Zwei Arten von achsensymmetrischen elektrodynamischen Waagen (Zwei-Ring- oder eine erweiterte Vier-Ring-Konfiguration) werden vorgestellt. Für ein besseres Verständnis wurden diese Systeme durch analytische und numerische Methoden untersucht. Eine theoretische Beschreibung der Fallensysteme und der Teilchenbewegung in ihrem Inneren ist durch die Mathieu-Gleichungen gegeben. Ein wichtiges Verhalten der Teilchen im Inneren der elektrodynamischen Waage wurde festgestellt: Die simulierte Flugbahn und die berechnete Wahrscheinlichkeit, zeigen, dass die Phaseninjektion f eine wichtige Rolle im Fangprozess der Teilchen spielt. Anhand dieser Simulationen konnte bewiesen werden, dass die Injektion der Teilchen bei einer willkürlichen Phase den Verlust von Teilchen bewirkt. Dieser Nachteil kann eingeschränkt werden, indem entweder ein phasensynchronisierender Schaltkreis zwischen den AC Ringelektroden und dem Teilchenzugang eingebaut wird oder indem eine passende Geometrie für das Fangsystem gefunden wird (ein System bei dem der Fangprozess eine weniger große Abhängigkeit von der Phase des alternativen Potentials zeigt).

In Anbetracht der Ziele dieser Arbeit wurde eine andere Art von Fangsystem entwickelt, die sogenannte Quadrupolfalle. Eine ähnliche theoretische Charakterisierung wie im Falle der elektrodynamischen Waage wurde vorgenommen und verschiedene spezifische Eigenschaften des Systems dargelegt. Eine der wichtigsten Eigenschaften ist die Fähigkeit (der Quadrupolssysteme im Allgemeinen) ein Phasenraum erhaltendes Abbild zu erzeugen: Zum Beispiel werden alle von einem Punkt ausgehenden Flugbahnen in einem Punkt fokussiert. Wenn man diese Fokussierungseigenschaft der Quadrupolfelder berücksichtigt, wird klar, dass kein weiterer phasensynchronisierender Schaltkreis gebraucht wird. Der ankommende Teilchenfluss wird in die Mitte des Systems fokussiert, und unter Berücksichtigung des DC-Potentials auf den Rohrelektroden erhält man ein stabiles „*Trapping*“ eines oder mehrerer Teilchen.

Kapitel 6 beschreibt die Experimentalaufbauten für die Untersuchung von einem oder von mehreren Teilchen. Die einzelnen Geräte, die in Kapitel 5 vorgeführt wurden, werden jetzt zusammengesetzt. Der erste Teil des Kapitels stellt die Methode und den experimentellen Aufbau für die Injektion von Feststoffteilchen vor. Um dem Nachteil der Phaseninjektion im Falle der elektrodynamischen Waage entgegenzukommen, wurde ein Programm entwickelt, das die Informationen (aufgenommen durch ein elektronisches Detektionssystem) von einer Teilchenwolke verarbeitet und das die Zahl der Teilchen reduziert, bis nur ein einziges übrig bleibt. Die Methode für die Ein-Teilchen-Untersuchung kann auch für mehrere Teilchen erweitert werden. Unter Verwendung des beschriebenen Systems werden die Teilchen aus einem Quadrupol in einen anderen bewegt und von einer Teilchenwolke in einen Teilchenstrom umgewandelt. Es wurde eine Linearität zwischen einem extern montierten Detektor und der Abbildung des Teilchenflusses durch ein Spektrometer auf einer CCD-Kamera festgestellt, welche für die gleichzeitige Detektion von mehreren Teilchen mittels Raman-Spektroskopie genutzt wurde. Für beide Methoden werden Raman-Ergebnisse gezeigt.

Eine Einschränkung bei der Anwendung der Raman-Spektroskopie besteht in den relativ langen Integrationszeiten, die für ein ausreichendes Signal-Rausch-Verhältnis gebraucht werden. Es gibt zwei Faktoren, die die Integrationszeit beeinflussen: (1) die einfallende Strahlung und die Detektorempfindlichkeit und (2) die Frequenz und die Intensität der Raman Banden. Durch Verwendung eines CCD-Detektors kann die gewünschte Detektorsensitivität erreicht werden. Der nächste Schritt

in der Systementwicklung ist die Verbesserung des Signal-Rausch-Verhältnisses. Um die Integrationszeit zu verkürzen, ist für zukünftige Arbeiten ein optisches System geplant, das optische Fasern und den Einbau eines FT-Raman-Moduls im sichtbaren Bereich einschließt.

Das Ziel dieser Arbeit war die Entwicklung und der Aufbau eines Geräts zur *on-line in-situ* Untersuchung eines einzelnen Teilchens mit Hilfe der Raman-Spektroskopie. Durch den vorgestellten experimentellen Aufbau und das entwickelte Steuerungsprogramm konnte das Ziel der Arbeit, die *in-situ* Untersuchung von Aerosolen bei normalem Luftdruck, erreicht werden. Die Raman-Spektroskopie wurde erfolgreich zur chemischen Charakterisierung von Aerosolen eingesetzt.

Appendix

Charging devices



a)

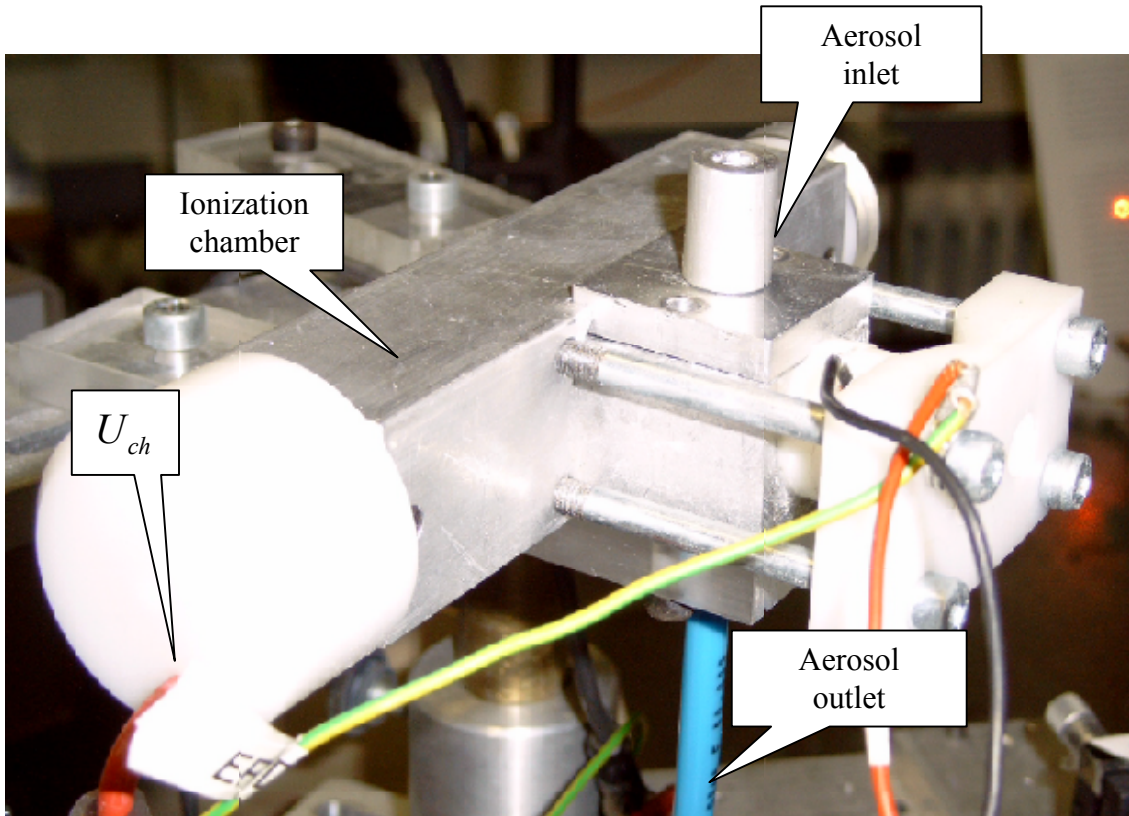


b)

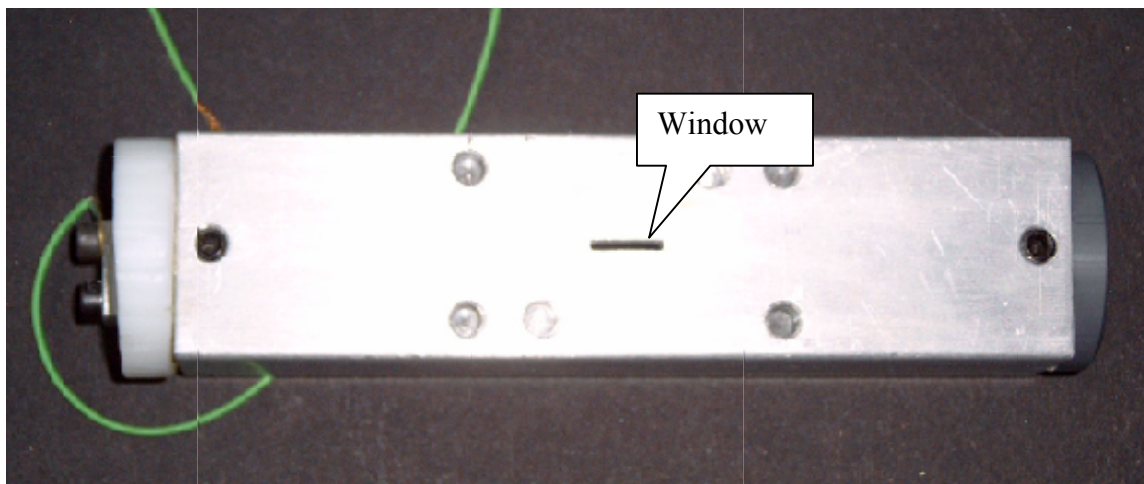
A.1. The Topas devices used for particle generation: a) atomizer, b) diluter.



A.2. The constructed aerodynamic lens.

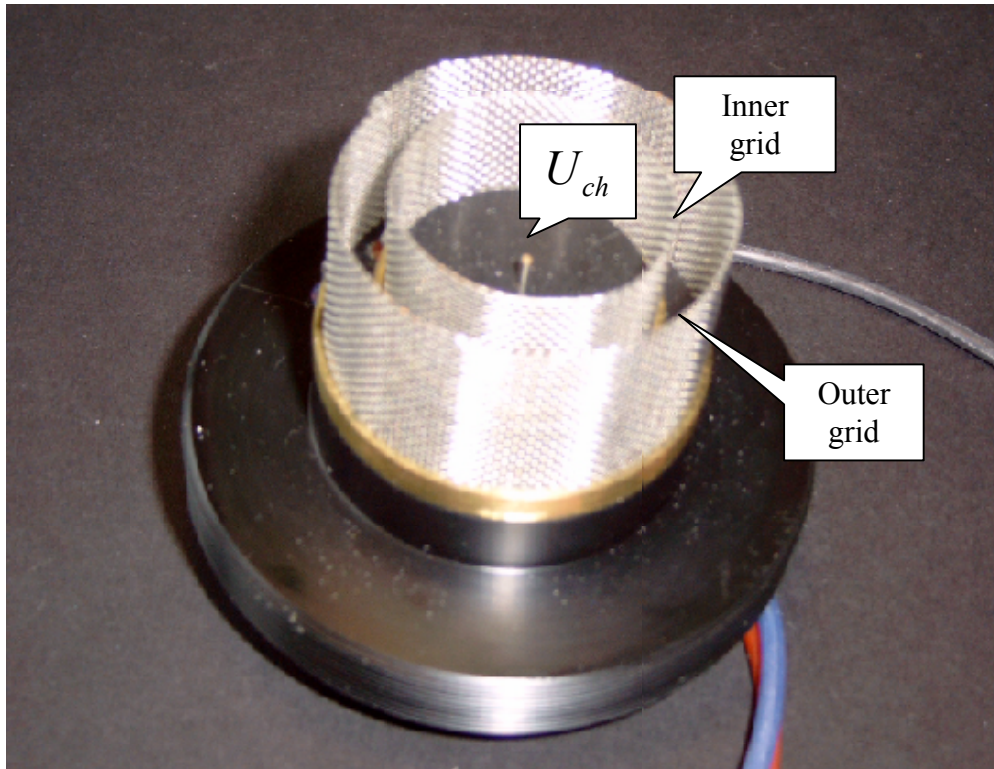


a)

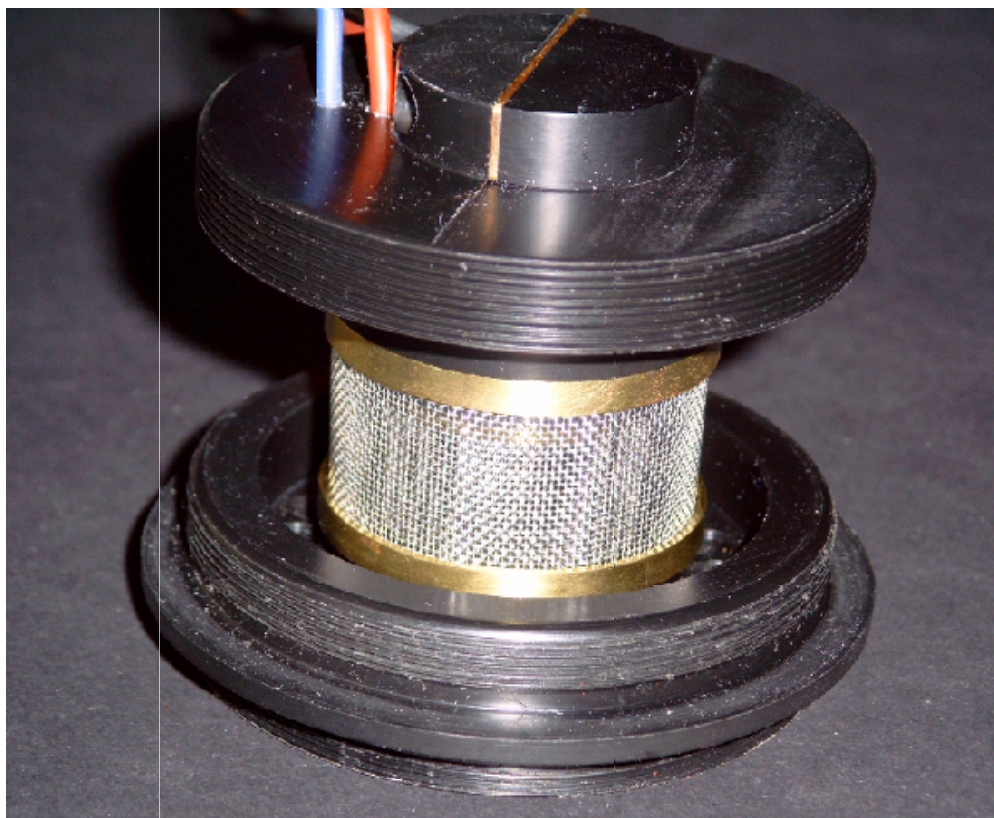


b)

A.3. The diffusion charger: a) general view, b) the ionization source (view from the extraction window).

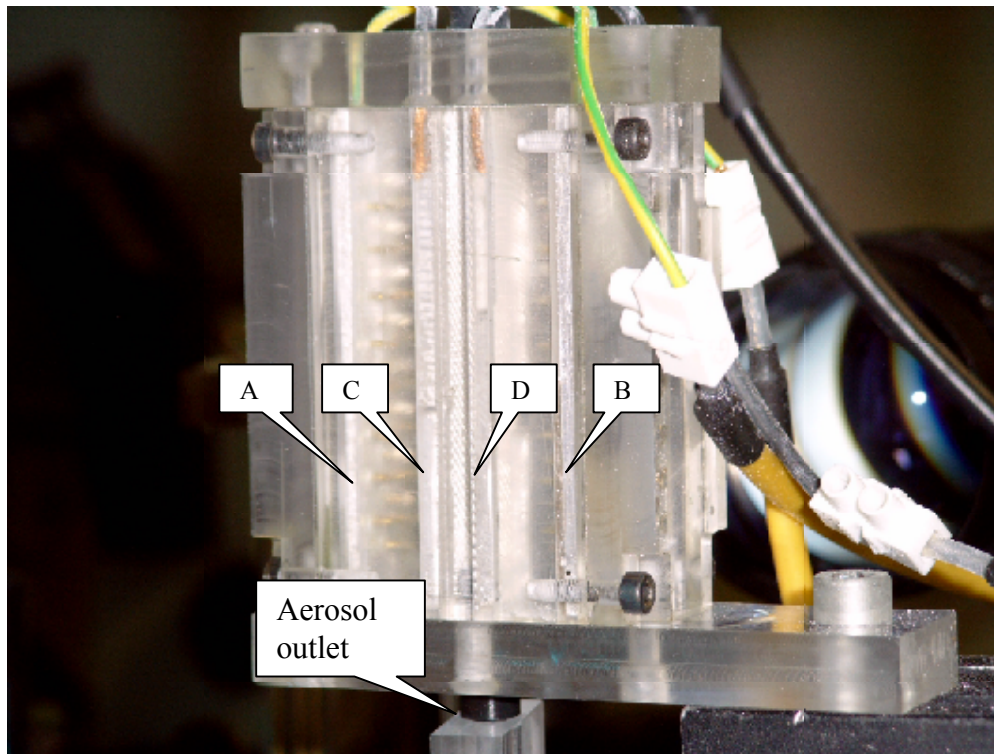


a)

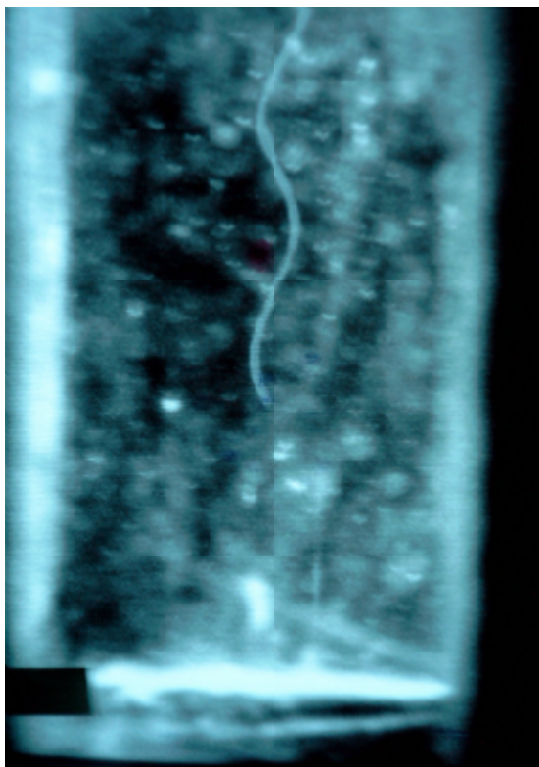


b)

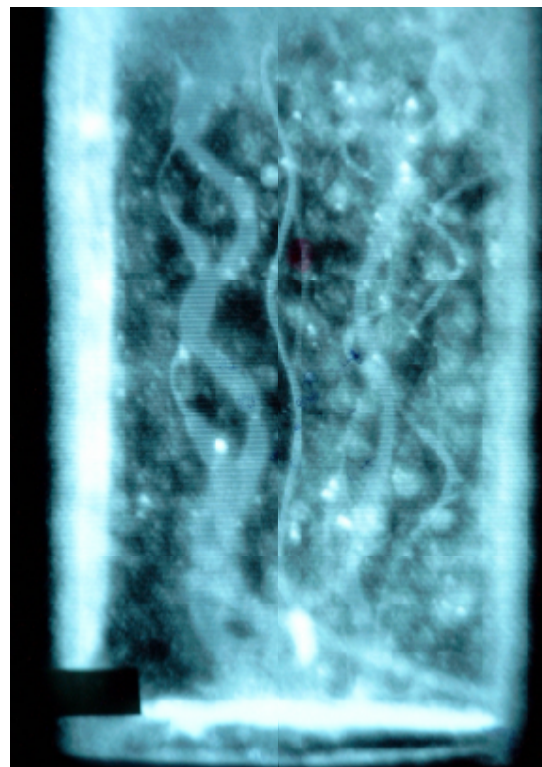
A.4. Field charger: a) open view (showing two cylindrical electrodes and the electric contact for the wolfram wire; the third electrode is mounted on the internal side of the cage), b) general view without the cage.



a)



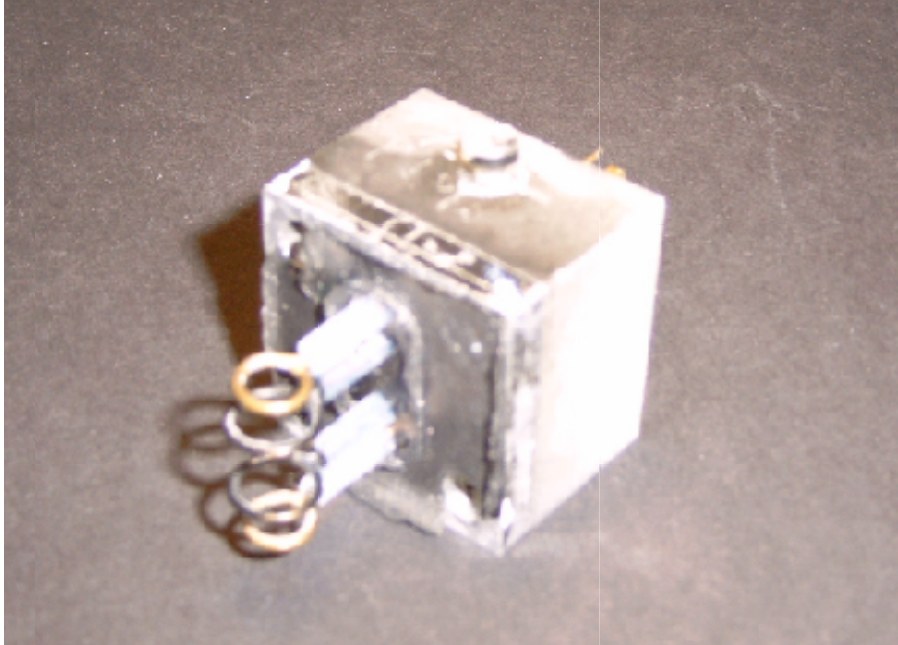
b)



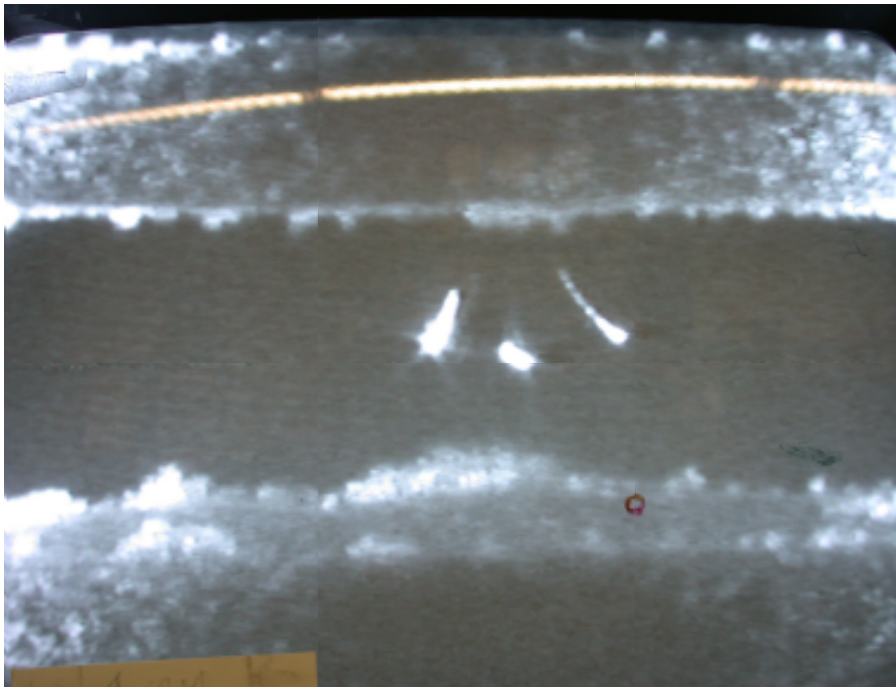
c)

A.5. The alternating electric field charger: a) general view, b) one particle passing through the charger; c) many particles. The quality of the pictures b) and c) is low because the image was recorded through the plastic wall of the charger having a thickness of 5 mm.

Trapping systems



a)



b)

B.1. a) The four ring electrodynamic balance; b) A two ring electrodynamic balance with plates electrodes.

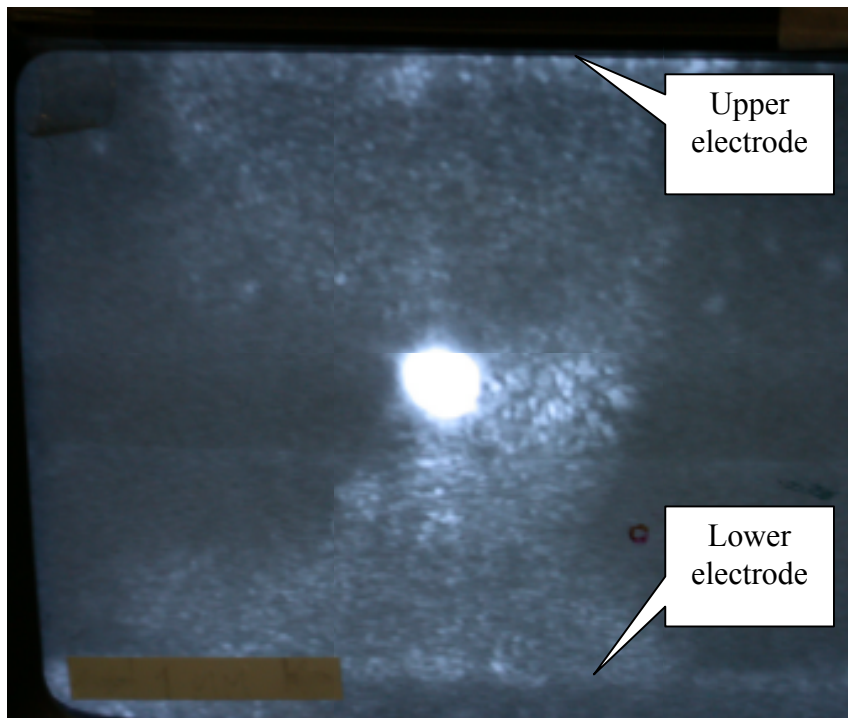
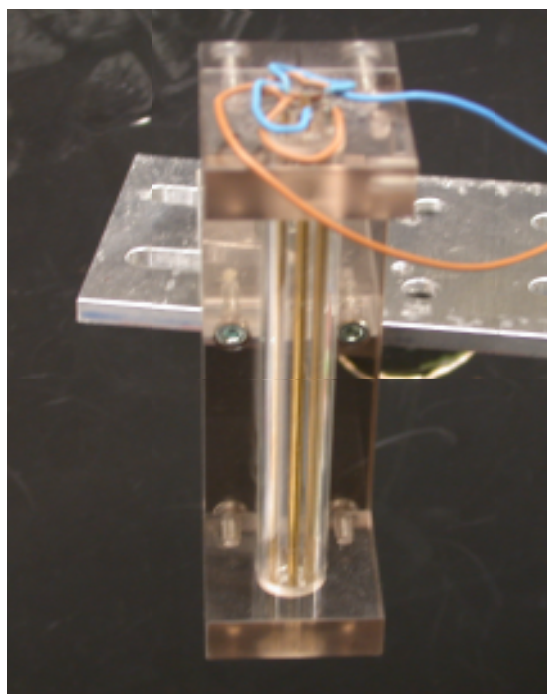
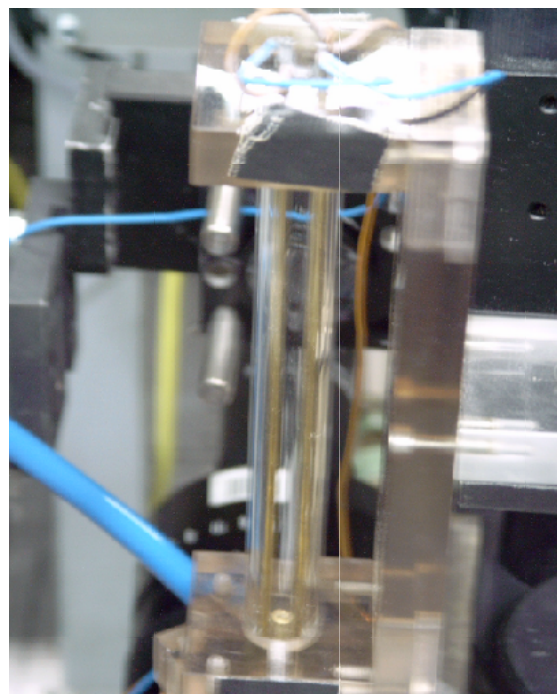


Fig. B.2. An illustration of a particle trapped between the ring and supporting rod connection; the electrode image does not show the same clarity as presented before in Fig. B.1b because the camera has been focused on the particle (which is out from the center).

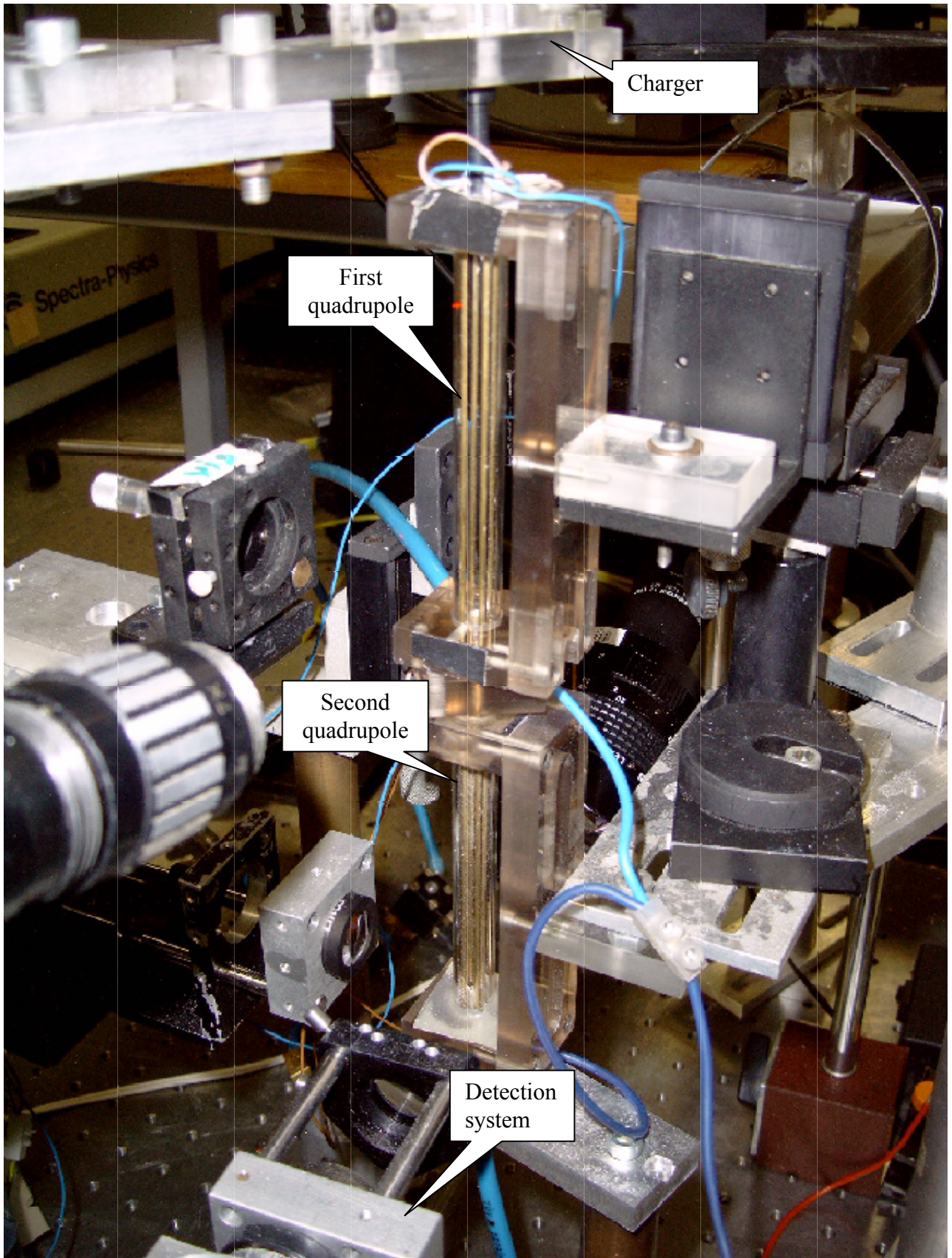


a)

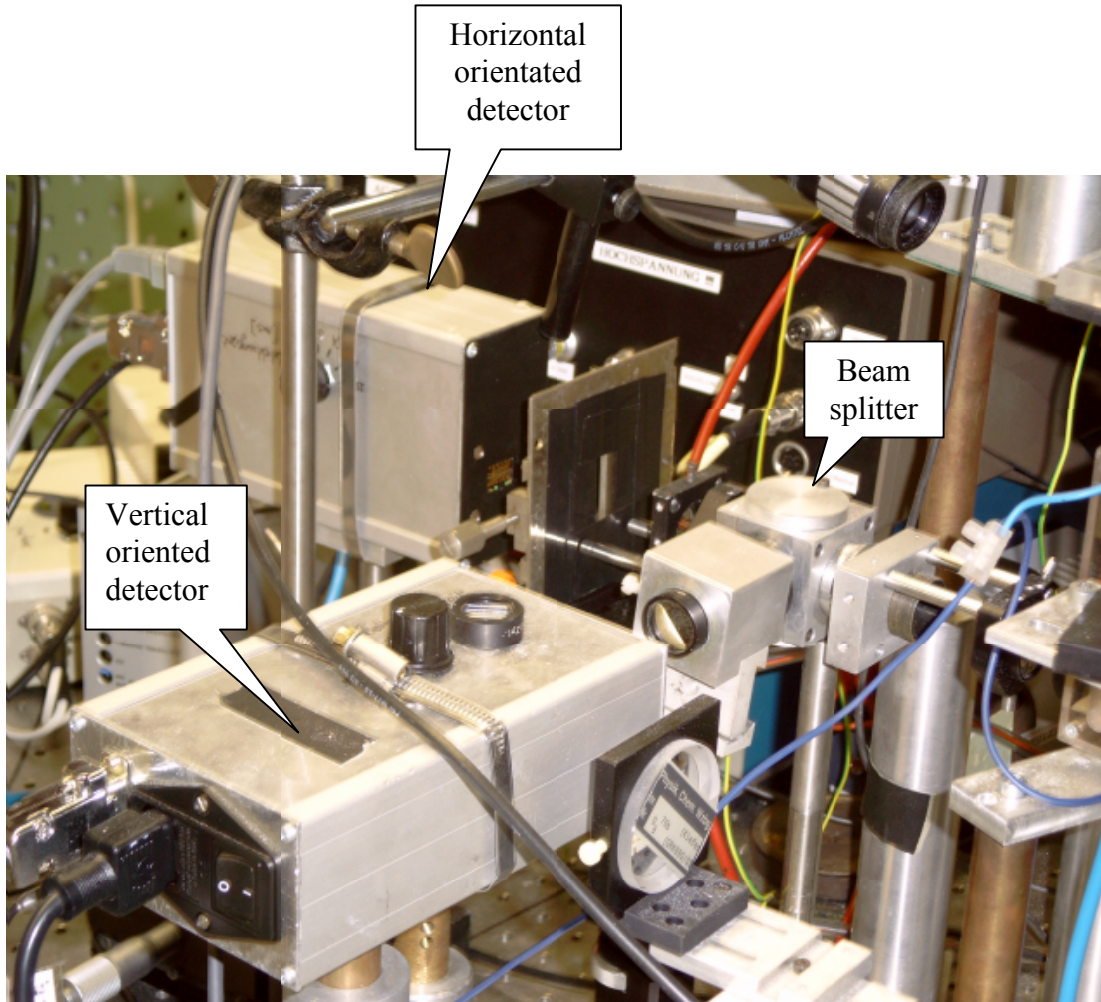


b)

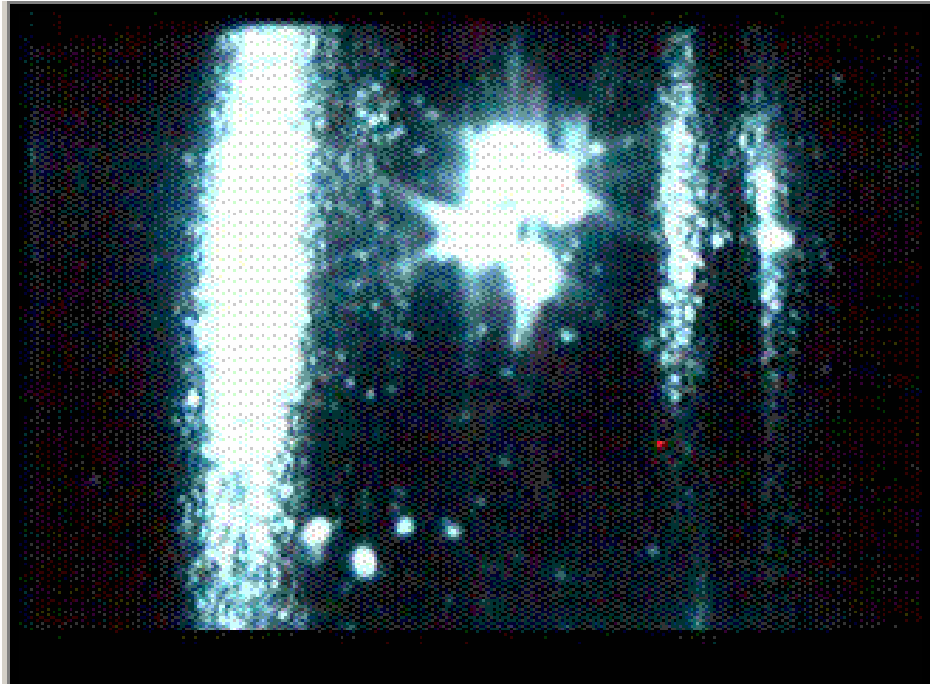
B.3. Trapping devices: a) hexapole system; b) quadrupole system.



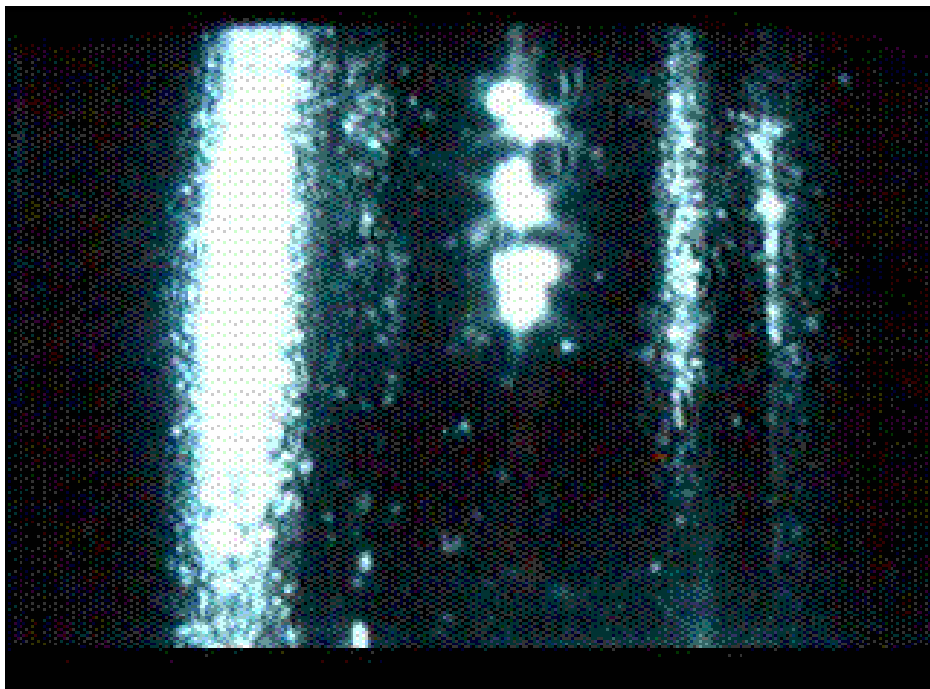
B.4. General idea of the set-up; the use of two identical quadrupole stages (the detection system not showed).



B.5. The detection system used for single particle investigation.

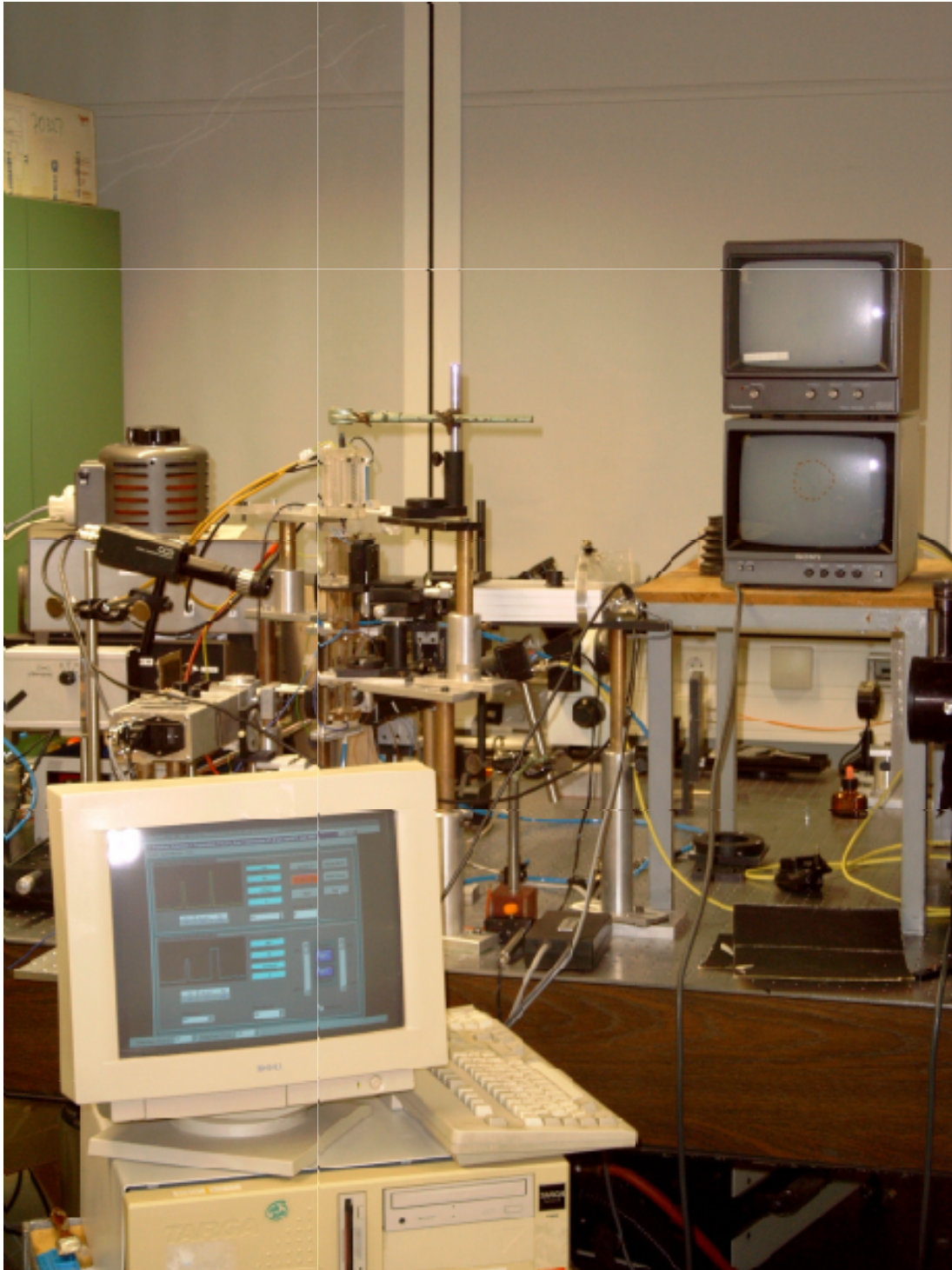


a)



b)

Fig. B.6. a) The image of a cloud (formed of four particles) trapped in the first quadrupole; b) The image of a particle stream transformed from a particle cloud corresponding to the second quadrupole.

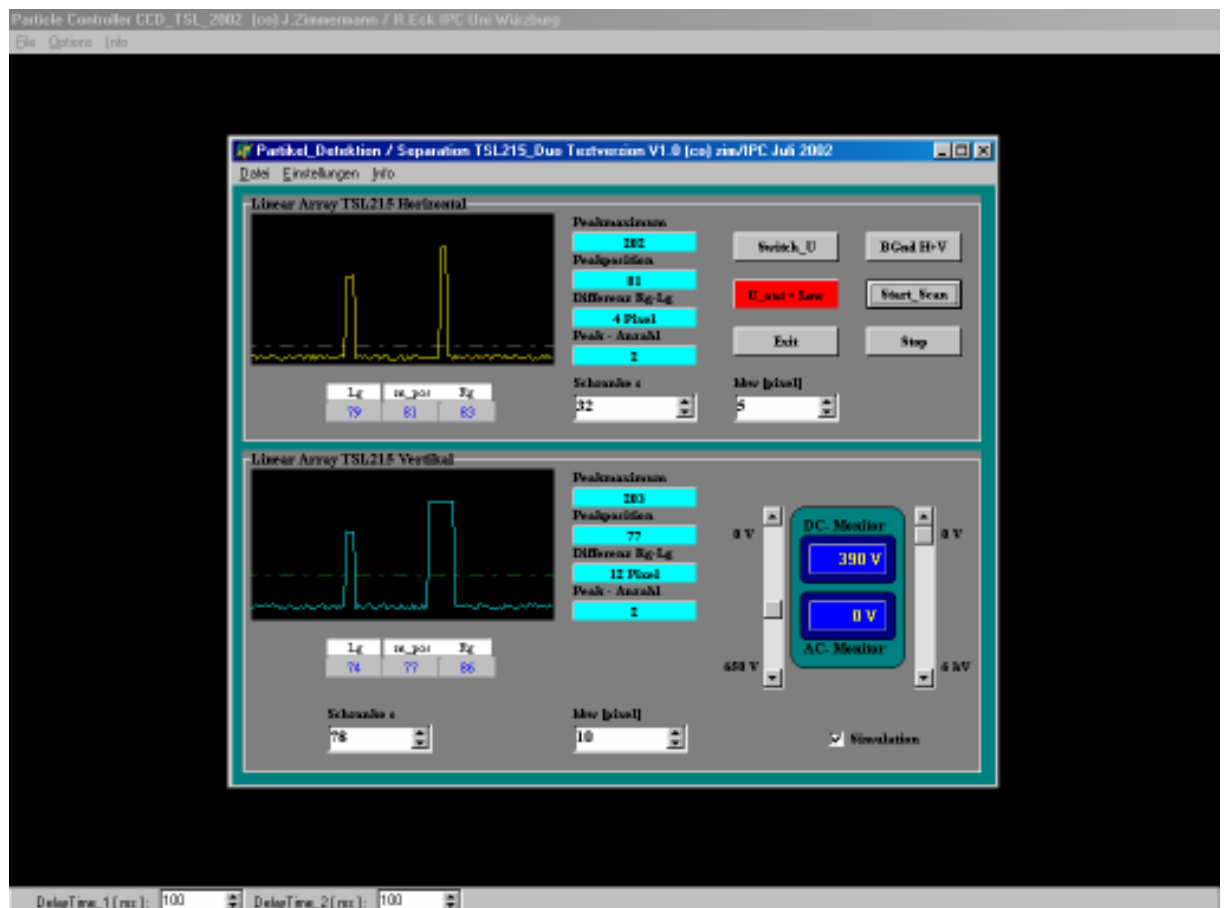


B.7. General view of the instrumentation.

Part_Scan program

Software – Sourcecode

Rechnergesteuerte optoelektronische Detektion und Separation von Mikropartikeln



Delphi / Objectpascal / Assembler XX86

```

program pardet_ccd_tsl;           // Mess- und Steuersoftware zur Partikeldetektion ( Ad Hoc Version )
                                // (co) J.Zimmermann IPC Uni Würzburg 2003

uses
  Forms,
  main in 'main.pas' {ccdtslmainfrm},
  adc_dac in 'adc_dac.pas',
  globvar in 'globvar.pas',
  scan_01 in 'scan_01.pas' {tslfrm},
  ccd_128_a in 'ccd_128_a.pas' {ccdfrm},
  shortinf in 'shortinf.pas' {Shortinfos};

{$R *.RES}

begin
  Application.Initialize;
  Application.CreateForm(Tccdtslmainfrm, ccdtslmainfrm);
  Application.CreateForm(Ttslfrm, tslfrm);
  Application.CreateForm(Tccdfrm, ccdfrm);
  Application.CreateForm(TShortinfos, Shortinfos);
  Application.Run;
end.

unit main;

interface

uses
  Windows, Messages, SysUtils, Classes, Graphics, Controls, Forms, Dialogs,
  Menus, StdCtrls, Spin, ExtCtrls;

type
  Tccdtslmainfrm = class(TForm)
    MainMenu1: TMainMenu;
    Beenden1: TMenuItem;
    Options1: TMenuItem;
    Beenden2: TMenuItem;
    Simulation1: TMenuItem;
    RealTimeAction1: TMenuItem;
    Info1: TMenuItem;
    About1: TMenuItem;
    ShortHelp1: TMenuItem;
    QuadruPol11: TMenuItem;
    QuadruPol21: TMenuItem;
    StartControlling1: TMenuItem;
    Panel1: TPanel;
    Label1: TLabel;
    SpinEdit1: TSpinEdit;
    Label2: TLabel;
    SpinEdit2: TSpinEdit;
    procedure Beenden2Click(Sender: TObject);
    procedure Simulation1Click(Sender: TObject);
    procedure RealTimeAction1Click(Sender: TObject);
    procedure About1Click(Sender: TObject);
    procedure FormCreate(Sender: TObject);
    procedure QuadruPol11Click(Sender: TObject);
    procedure QuadruPol21Click(Sender: TObject);
    procedure StartControlling1Click(Sender: TObject);
    procedure SpinEdit1Change(Sender: TObject);
    procedure SpinEdit2Change(Sender: TObject);
  private

```

```

    { Private-Deklarationen }
public
    { Public-Deklarationen }
end;

var
    ccdtslmainfrm: Tccdtslmainfrm;

implementation

uses globvar,ccd_128_a,scan_01, adc_dac;

{$R *.DFM}

procedure Tccdtslmainfrm.Beenden2Click(Sender: TObject);
begin
    // alle Dac's und Ports runterfahren, dann ..
    close;
end;

procedure Tccdtslmainfrm.Simulation1Click(Sender: TObject);
begin
    simulation1.checked:=not simulation1.checked;
    if simulation1.checked then
    begin
        ccdfrm.Messmodus1.checked:=false;
        tslfrm.checkbox1.checked:=true;
        realtimeaction1.checked:=false;
    end
    else
    begin
        ccdfrm.Messmodus1.checked:=true;
        tslfrm.checkbox1.checked:=false;
        realtimeaction1.checked:=true;
    end;
end;

procedure Tccdtslmainfrm.RealTimeAction1Click(Sender: TObject);
begin
    RealTimeAction1.checked:=not RealTimeAction1.checked;
    if RealTimeAction1.checked then
    begin
        ccdfrm.Messmodus1.checked:=true;
        tslfrm.checkbox1.checked:=false;
        simulation1.checked:=false;
    end
    else
    begin
        ccdfrm.Messmodus1.checked:=false;
        tslfrm.checkbox1.checked:=true;
        simulation1.checked:=true;
    end;
end;

procedure Tccdtslmainfrm.About1Click(Sender: TObject);
begin
    showmessage('Mess- u. Steuersoftware'+#13+
                'Particle Controller CCD_TSL'+#13+
                '(co) Jürgen Zimmermann'+#13+
                'IPC Uni Würzburg dez 2002');
end;

```

```

procedure Tccdtslmainfrm.FormCreate(Sender: TObject);
begin
  // diverse Startwerte für Ports u. DAC's vorgeben und dann ..
  dac_1(0); // DC Off
  dac_2(0);
  dac_3(0); // AC Off
  dac_4(255); // Flow On
  dt_1:=100; // 100 ms DelayTime_1 optionally prescaled for DC switching
  dt_2:=100; // 100 ms DelayTime_2 " " "
  panel1.width:=width-1;
end;

procedure Tccdtslmainfrm.QuadruPol11Click(Sender: TObject);
begin
  ccdfrm.showmodal; // Justage/Einstellmodus CCD2048
end;

procedure Tccdtslmainfrm.QuadruPol21Click(Sender: TObject);
begin
  tslfrm.showmodal; // Justage/Einstellmodus TSL215_Duo
end;

procedure Tccdtslmainfrm.StartControlling1Click(Sender: TObject); // PD_Control
var acw : word;
begin
  messagebeep(0);
  // ParticleWatching Quadrupol_1 ( CCD_LineCamera )
  ccdfrm.Show; // Open CCD_Window, CCD - Particle Watching bis ..
  ccdfrm.justierenclick(self); // ..bis Partikelposition/amplitude stabilisiert
  repeat
    application.processmessages
  until p_cnt=5; // Abbruchkriterium Particle Watching

  dac_4(0); // Gas Flow Off
  dac_1(0); // DC Off
  sleep(dt_1); // Delay simuliert Fotodiodenereignis
  dac_1(da_wert1); // DC On (DC-Wert wieder einstellen)
  sleep(dt_2); // Delaytime_2 vor der Partikelseparation

  // ParticleSeparation Quadrupol_2 ( Lineararrays TSL215 )
  tslfrm.Show; // Open TSL_Window
  tslfrm.button1click(self); // .. bis num = 1 ( Einzelnes Teilchen )
  repeat
    application.processmessages
  until tslfrm.timer1.enabled = false;

  showmessage('An dieser Stelle folgt die Ramanmessung ...');

  dac_4(255); // Flow On
  dac_3(0); // AC Off
  sleep(dt_1); // dt_1 ms Delay

  acw:=0;
  while acw < da_wert3 do
  begin
    inc(acw,1);
    sleep(1);
    dac_3(acw); // AC-Wert wieder hochfahren
  end; // while

```



```

// evtl. gesamten Controlling Process wiederholen ( bis ..?)

showmessage('One Particle Cycle Completed !!');
end;

procedure Tcdtslmainfrm.SpinEdit1Change(Sender: TObject);
begin
  try
    dt_1:=spinedit1.value;
  except;
  end;
end;

procedure Tcdtslmainfrm.SpinEdit2Change(Sender: TObject);
begin
  try
    dt_2:=spinedit2.value;
  except;
  end;
end;

end.

unit Scan_01;

interface

uses
  SysUtils, WinTypes, WinProcs, Messages, Classes, Graphics, Controls,
  Forms, Dialogs, ExtCtrls, StdCtrls, Spin, Menus;

type
  Ttslfrm = class(TForm)
    Timer1: TTimer;
    GroupBox1: TGroupBox;
    Image1: TImage;
    Label3: TLabel;
    Label4: TLabel;
    Label5: TLabel;
    Button1: TButton;
    Button2: TButton;
    Button3: TButton;
    Panel2: TPanel;
    Panel3: TPanel;
    Panel4: TPanel;
    GroupBox2: TGroupBox;
    Image2: TImage;
    Panel5: TPanel;
    Label6: TLabel;
    Panel6: TPanel;
    Label7: TLabel;
    SpinEdit1: TSpinEdit;
    Label8: TLabel;
    Panel1: TPanel;
    Label1: TLabel;
    Label2: TLabel;
    ScrollBar1: TScrollBar;
    Panel7: TPanel;
    Button4: TButton;
    Shape2: TShape;
  end;

```

```

Shape1: TShape;
MainMenu1: TMainMenu;
Datei1: TMenuItem;
Beenden1: TMenuItem;
Info1: TMenuItem;
About1: TMenuItem;
Label10: TLabel;
Panel8: TPanel;
Panel9: TPanel;
Panel10: TPanel;
Label12: TLabel;
Label13: TLabel;
Label14: TLabel;
Panel11: TPanel;
Label15: TLabel;
Einstellungen1: TMenuItem;
BackgroundAbzug1: TMenuItem;
Button5: TButton;
Panel12: TPanel;
Shape3: TShape;
Label16: TLabel;
ScrollBar2: TScrollBar;
Label17: TLabel;
Label18: TLabel;
Panel13: TPanel;
Label19: TLabel;
Panel14: TPanel;
Label20: TLabel;
Label21: TLabel;
Label22: TLabel;
Label23: TLabel;
Panel15: TPanel;
Panel16: TPanel;
Panel17: TPanel;
CheckBox1: TCheckBox;
SpinEdit4: TSpinEdit;
SpinEdit5: TSpinEdit;
Label24: TLabel;
Label25: TLabel;
SpinEdit2: TSpinEdit;
Label9: TLabel;
procedure ScrollBar1Change(Sender: TObject);
procedure Button1Click(Sender: TObject);
procedure Button3Click(Sender: TObject);
procedure Button2Click(Sender: TObject);
procedure Timer1Timer(Sender: TObject);
procedure FormCreate(Sender: TObject);
procedure Button4Click(Sender: TObject);
procedure SpinEdit1Change(Sender: TObject);
procedure Beenden1Click(Sender: TObject);
procedure About1Click(Sender: TObject);
procedure aprox_uq_fin(step : byte);
procedure aprox_peakmax(step : byte);
procedure aprox_ac_fin(step : byte);
procedure BackgroundAbzug1Click(Sender: TObject);
procedure Button5Click(Sender: TObject);
procedure ScrollBar2Change(Sender: TObject);
procedure SpinEdit4Change(Sender: TObject);
procedure SpinEdit5Change(Sender: TObject);
procedure SpinEdit2Change(Sender: TObject);
private

```

```

    { Private-Deklarationen }
public
    { Public-Deklarationen }
end;

var
    tslfrm: Ttslfrm;

implementation
uses globvar,adc_dac;

{$R *.DFM}

procedure Ttslfrm.aprox_uq_fin(step : byte); { aproximate dac -> uq_fin }
{ aprox. da_wert1 -> uq_fin stepwise }
begin
    if da_wert1 < uq_fin then
        begin
            da_wert1:=da_wert1 + step;
            scrollbar1.position:=da_wert1;
        end
    else sweep_uq:=true;
end; { aproximate uq_fin }

procedure Ttslfrm.aprox_peakmax(step : byte); { aproximate dac -> peakmax }
begin
    if ((pmaxpos<(mp_alt-2))or(pmaxpos>(mp_alt+2))) then
        begin
            da_wert1:=da_wert1 + step;
            scrollbar1.position:=da_wert1;
        end
    else sweep_uq:=true;
end; { aproximate peakmax }

procedure Ttslfrm.aprox_ac_fin(step : byte); { aproximate dac -> peakwidth }
begin
    if (da_wert3<ac_fin) then { akt. AC < voreigestelltem AC-Wert? }
        begin
            da_wert3:=da_wert3 + step;
            scrollbar2.position:=da_wert3;
        end
    else sweep_ac:=true;
end; { aproximate peak }

procedure Ttslfrm.ScrollBar1Change(Sender: TObject); // DC Voltage
var da_s : string;
    w : real;
begin
    da_wert1:=scrollbar1.position;
    w:=da_wert1/255*650;
    str(w:8:0,da_s);
    panel1.caption:=da_s+' V';
    dac_1(round(0.99*da_wert1));
end;

procedure Ttslfrm.Button1Click(Sender: TObject); { Button Start }
begin
    timer1.enabled:=true;
    start_flag:=true; { Merker Start Detection }
    sweep_uq:=false; { Sweep Flag DC zurücksetzen }
end;

```

```

sweep_ac:=false; { Sweep Flag AC zurücksetzen }
dec_dc_flag:=false;
dec_ac_flag:=false;
inc_dc_flag:=false;
inc_ac_flag:=false;
uq_fin:=da_wert1; { Quadrupolanfangswert = eingestellter Sollwert DC }
ac_fin:=da_wert3; { Quadrupolanfangswert = eingestellter Sollwert AC }
end;

```

```

procedure Ttslfrm.Button3Click(Sender: TObject);
begin
  timer1.enabled:=false;
end;

```

```

procedure Ttslfrm.Button2Click(Sender: TObject);
begin
  Beenden1click(self);
end;

```

```

procedure Ttslfrm.Timer1Timer(Sender: TObject); { Messen / Grafikplot }
var i,l,r : integer;

```

```

begin
  if checkbox1.checked then { Random Test Modus }
  begin
    for i:=0 to 127 do dat[i]:=random(10)+10;
    for i:=80 to 82 do dat[i]:=random(10)+200;
    for i:=40 to 43 do dat[i]:=random(4)+150;
    for i:=0 to 127 do dat1[i]:=random(10)+20;
    for i:=40 to 43 do dat1[i]:=random(4)+150;
    for i:=75 to 85 do dat1[i]:=random(4)+200;
  end
  else
  begin
    scan_128; { Horizontal Detection }
    scan_128_2; { Vertical Detection }
  end;

```

```

  if backgroundabzug1.checked then
  for i:=0 to 127 do
  begin
    if (dat[i]-bgnd[i])>=0 then dat[i]:=dat[i]-bgnd[i] else dat[i]:=0;
    if (dat1[i]-bgnd_2[i])>=0 then dat1[i]:=dat1[i]-bgnd_2[i] else dat1[i]:=0;
  end;

```

```

  { Hor. Detektor: Datenanalyse/ScreenPlot scan_128 / Array dat[] }
  max:=s_h;
  for i:=0 to 127 do if dat[i]>max then begin { search maximum }
    max:=dat[i]; { and maxposition }
    maxpos:=i;
  end; {for ..if ..}

```

```

  r:=127;l:=0;
  for i:=maxpos downto 0 do { left edge position in pixel }
  begin
    if dat[i]<=s_h then { at level s_h }
    begin
      l:=i;
      break;
    end; { if }
  end; { for }

```

```

for i:=maxpos to 127 do          { right edge position in pixel }
begin
  if dat[i]<=s_h then          { at level s_h }
  begin
    r:=i;
    break;
  end; { if }
end; { for }
hwb:=abs(r-maxpos)+abs(maxpos-1);    { peakwidth at level s_h }
panel4.caption:=inttostr(max);
panel3.caption:=inttostr(maxpos);
panel2.caption:=inttostr(hwb)+' Pixel';

num1:=0;
pmax1:=s_h;pmax2:=s_h;

if max > s_h then pnum:=1; { Peakmaximum > Schranke + Epsilon ? }

begin
  mp_alt1:=maxpos;
  panel16.caption:=inttostr(maxpos);
end; { if .. }

for i:=maxpos downto 0 do      { Suche Peakgrenze links }
  if dat[i] <= s_h then begin
    lg1:=i;
    panel17.caption:=inttostr(lg1);
    break;
  end;
for i:=maxpos to 127 do      { Suche Peakgrenze rechts }
  if dat[i] <= s_h then begin
    rg1:=i;
    panel15.caption:=inttostr(rg1);
    break;
  end;

{ Suche nach Peaks links von Peak_1 }
for i:=lg1 downto 0 do if dat[i]>pmax1 then pmax1:=dat[i];
if pmax1 > s_h then inc(num1); { Peakmaximum > Schranke + Epsilon ? }

with image1.canvas do        { screenplot scan data }
begin
  pen.color:=clblack;
  rectangle(0,0,image1.width,image1.height);
  pen.color:=clgray;
  pen.style:=psdashdot;
  moveto(0,128-s_h div 2);lineto(image1.width,128-s_h div 2);
  pen.color:=clyellow;
  pen.style:=pssolid;
  pen.color:=clyellow;
  moveto(0,128-dat[0]div 2);
  for i:=1 to 127 do lineto(i*2,128-dat[i]div 2);
end;
{ Peakstatistik, Anzahl aller Peaks > Schranke s }
pnum:=0;
for i:=0 to 127 do liste[i]:=dat[i]; { Datenfeld kopieren in Arbeitsfeld }
end_flag:=false;
repeat
  max:=s_h;
  for i:=0 to 127 do if liste[i] > max then begin
    max:=liste[i];

```

```

                                maxpos:=i;
                                end;
if max > s_h then
begin
  inc(pnum);
  end_flag:=false;
end
else end_flag:=true;
if not end_flag then
begin
  for i:=maxpos downto 0 do
  if liste[i]<=s_h then begin lg:=i;break; end; { linke Peakgrenze zu s }
  for i:=maxpos to 127 do
  if liste[i]<=s_h then begin rg:=i;break; end; { rechte Peakgrenze zu s }
  for i:=lg to rg do liste[i]:=0;          { Peak eliminieren }
  end;
until end_flag;
panel1.caption:=inttostr(pnum);

```

```

{ ----- }
{ Datenanalyse/ScreenPlot scan_128_2 / Array dat1[] vertical data }
{ ----- }

```

```

num:=0;
pmax:=s;pmax1:=s;pmax2:=s;
for i:=0 to 127 do if dat1[i]>pmax then begin
                                pmax:=dat1[i];
                                pmaxpos:=i;
                                end; {for ..if ..}

r:=127;l:=0;
for i:=pmaxpos downto 0 do          { left edge position in pixel }
begin
  if dat1[i]<=s then                { at level s }
  begin
    l:=i;
    break;
  end; { if }
end; { for }

for i:=pmaxpos to 127 do           { right edge position in pixel }
begin
  if dat1[i]<=s then                { at level s }
  begin
    r:=i;
    break;
  end; { if }
end; { for }

```

```

if pmax > s then num:=1; { Peakmaximum > Schranke + Epsilon ? }

```

```

panel5.caption:=inttostr(pmax);
panel6.caption:=inttostr(pmaxpos);
panel9.caption:=inttostr(pmaxpos);

```

```

for i:=pmaxpos downto 0 do        { Suche Peakgrenze links }
  if dat1[i] <= s then begin
    lg:=i;
    panel8.caption:=inttostr(lg);
    panel8.refresh;
  end;

```

```

        break;
    end;
for i:=pmaxpos to 127 do      { Suche Peakgrenze rechts }
    if dat1[i] <= s then begin
        rg:=i;
        panel10.caption:=inttostr(rg);
        panel10.refresh;
        break;
    end;
hwb:=abs(rg-lg);           { peakwidth at level s }
panel13.caption:=inttostr(hwb)+ ' Pixel';
panel13.refresh;
{ Suche nach Peaks links von Peak_1 }
for i:=lg downto 0 do if dat1[i]>pmax1 then pmax1:=dat1[i];
if pmax1 > s then inc(num); { Peakmaximum > Schranke ? }

{ Suche nach Peaks rechts von Peak_1 }
for i:=rg to 127 do if dat1[i]>pmax2 then pmax2:=dat1[i];
if pmax2 > s then inc(num); { Peakmaximum > Schranke ? }

{ Auswertung num = Anzahl Peaks = Anzahl Partikel }
{ ***** }

if (num>1)and checkbox1.checked then spinedit1.value:=spinedit1.value+2;{Test}

{ DC and AC criteria handling Vertical Detection }
if (num>1)or(hwb>=hb_v) then
begin
    scrollbar1.position:=scrollbar1.position-2;  { DC step down }
    scrollbar2.position:=scrollbar2.position -2;  { AC step down }
end;
{ reverse criteria }
if (num=1)and (hwb<hb_v) then aprox_uq_fin(2);  { DC backward to startval.}

{ AC criteria handling Horizontal Detection }
if (pnum>1)or(hwb_h>=hb_h) then
    scrollbar2.position:=scrollbar2.position -2;  { AC step down }

if(scrollbar1.position=0)and(hwb_h>=hb_h) then
    scrollbar2.position:=scrollbar2.position -2;  { AC step down }

{ reverse criteria }
if (pnum=1)and(hwb_h<hb_h) then aprox_ac_fin(2);  { AC backward to startval.}

if (pnum=1)and(num=1)and not sweep_uq then // zur Ramanmessung wenn alles OK
begin
    timer1.enabled:=false;
    close
end;

{ screenplot data }
with image2.canvas do
begin
    pen.color:=clblack;
    rectangle(0,0,image2.width,image2.height);
    pen.color:=clgreen;
    pen.style:=psdashdot;
    moveto(0,128-s div 2);lineto(image2.width,128-s div 2);

```

```

pen.color:=claquea;
pen.style:=pssolid;
moveto(0,128-dat1[0]div 2);
for i:=1 to 127 do lineto(i*2,128-dat1[i]div 2);
end;

{ Peakstatistik, Anzahl aller Peaks > Schranke s }
pnum1:=0;
for i:=0 to 127 do liste[i]:=dat1[i]; { Datenfeld kopieren in Arbeitsfeld }
end_flag:=false;
repeat
max:=s;
for i:=0 to 127 do if liste[i] > max then begin
max:=liste[i];
maxpos:=i;
end;

if max > s then
begin
inc(pnum1);
end_flag:=false;
end
else end_flag:=true;
if not end_flag then
begin
for i:=maxpos downto 0 do
if liste[i]<=s then begin lg:=i;break; end; { linke Peakgrenze zu s }
for i:=maxpos to 127 do
if liste[i]<=s then begin rg:=i;break; end; { rechte Peakgrenze zu s }
for i:=lg to rg do liste[i]:=0; { Peak eliminieren }
end;
until end_flag;
panel14.caption:=inttostr(pnum1);

```

```
end; { Timerproc. Messen/Grafikausgabe OnLine }
```

```

procedure Ttslfrm.FormCreate(Sender: TObject);
begin
flag_u:=false;
s:=32;
s_h:=32;
d_fakt:=0.5;
hb_h:=5;
hb_v:=10;
with image1.canvas do
begin
pen.color:=clblack;
brush.color:=clblack;
rectangle(0,0,image1.width,image1.height);
pen.color:=clgray;
pen.style:=psdashdot;
moveto(0,128-s_h div 2);lineto(image1.width,128-s_h div 2);
pen.color:=clyellow;
pen.style:=pssolid;
end;
with image2.canvas do
begin
pen.color:=clblack;
brush.color:=clblack;
rectangle(0,0,image2.width,image2.height);

```



```

    pen.color:=clgreen;
    pen.style:=psdashdot;
    moveto(0,128-s div 2);lineto(image2.width,128-s div 2);
    pen.color:=claqua;
    pen.style:=pssolid;
end;
end;

procedure Ttslfrm.Button4Click(Sender: TObject);
begin
    flag_u:=not flag_u;
    if flag_u then
    begin
        dac_4(255);
        panel7.caption:='U_out = High';
    end
    else
    begin
        dac_4(0);
        panel7.caption:='U_out = Low';
    end; { if .. }
end;

procedure Ttslfrm.SpinEdit1Change(Sender: TObject);
var i : integer;
begin
    try
        s:=spinedit1.value;
    except
    end;
    with image2.canvas do
    begin
        rectangle(0,0,image2.width,image2.height);
        pen.color:=clgreen;
        pen.style:=psdashdot;
        moveto(0,128-s div 2);lineto(image2.width,128-s div 2);
        pen.color:=claqua;
        pen.style:=pssolid;
        moveto(0,128-dat1[0]div 2);
        for i:=1 to 127 do lineto(i*2,128-dat1[i]div 2);
    end;
end;

procedure Ttslfrm.Beenden1Click(Sender: TObject);
begin
    dac_1(0);
    dac_2(0);
    dac_3(0);
    dac_4(0);
    close
end;

procedure Ttslfrm.About1Click(Sender: TObject);
begin
    showmessage('Mess- und Datenerfassungsprogramm'+#13+
        'Partikel_Detektion/Separation PDS_IPC'+#13+
        '(co) Jürgen Zimmermann IPC/DV-Systemtechnik'+#13+
        ' Uni Würzburg Juli 2002');
end;

```

```

procedure Ttslfrm.BackgroundAbzug1Click(Sender: TObject);
begin
  backgroundabzug1.checked:=not backgroundabzug1.checked;
end;

procedure Ttslfrm.Button5Click(Sender: TObject); { BkGnd-Messung }
var i : integer;
begin
  if checkbox1.checked then begin
    for i:=0 to 127 do bgnd[i]:=random(10)+32;
    for i:=0 to 127 do bgnd_2[i]:=random(10)+32;
  end
else
begin
  scan_128;
  scan_128_2;
  for i:=0 to 127 do bgnd[i]:=dat[i];
  for i:=0 to 127 do bgnd_2[i]:=dat1[i];
end;
with image1.canvas do
begin
  pen.color:=clblack;
  rectangle(0,0,image1.width,image1.height);
  pen.color:=clyellow;
  moveto(0,128-bgnd[0]div 2);
  for i:=1 to 127 do lineto(i*2,128-bgnd[i]div 2);
end;
with image2.canvas do
begin
  pen.color:=clblack;
  rectangle(0,0,image1.width,image1.height);
  pen.color:=clwhite;
  moveto(0,128-bgnd_2[0]div 2);
  for i:=1 to 127 do lineto(i*2,128-bgnd_2[i]div 2);
end;
end;

procedure Ttslfrm.ScrollBar2Change(Sender: TObject); // AC Voltage
var da_s : string;
    w : real;
begin
  da_wert3:=scrollbar2.position;
  w:=da_wert3/255*6000;
  str(w:8:0,da_s);
  panel12.caption:=da_s+' V';
  dac_3(round(0.999*da_wert3));
end;

procedure Ttslfrm.SpinEdit4Change(Sender: TObject);
begin
  try
    hb_h:=spinedit4.value;
  except
  end;
end;

procedure Ttslfrm.SpinEdit5Change(Sender: TObject);
begin
  try
    hb_v:=spinedit5.value;
  except

```

```

end;
end;

procedure Ttslfrm.SpinEdit2Change(Sender: TObject);
var i : integer;
begin
try
s_h:=spinedit2.value;
except
end;
with image1.canvas do
begin
rectangle(0,0,image1.width,image1.height);
pen.color:=clgray;
pen.style:=psdashdot;
moveto(0,128-s_h div 2);lineto(image1.width,128-s_h div 2);
pen.color:=claqua;
pen.style:=pssolid;
moveto(0,128-dat1[0]div 2);
for i:=1 to 127 do lineto(i*2,128-dat1[i]div 2);
end;
end;

end.

unit ccd_128_a; { Messprogramm CCD_Zeilenkamera 2048LH8 (co) zim PC/12/99 }
{ Version 1.0 ( Testversion ) last change : 05.01.2000 }
{ Erweiterungen : div. Anzeigemodi, Justagemode 11/1/2000 }
{ Neu : Peakdetektion und Auswertung des Backgroundlevels, }
{ Speicherung nur nach Abzug des Untergrundsignalanteils. }
{ last modification : 17.9.2001 zim }
{ modified/extended : jan/feb 2002 ( zim /PC/EL/DVsys ) }

interface

uses
Windows, Messages, SysUtils, Classes, Graphics, Controls, Forms, Dialogs,
ExtCtrls, StdCtrls, Spin, OleCtrls, Menus;

type
Tccdfm = class(TForm)
Label3: TLabel;
Label4: TLabel;
Label5: TLabel;
Label6: TLabel;
Label7: TLabel;
Label8: TLabel;
Label9: TLabel;
GroupBox1: TGroupBox;
Image1: TImage;
GroupBox2: TGroupBox;
GroupBox3: TGroupBox;
Timer1: TTimer;
SpinEdit2: TSpinEdit;
Label10: TLabel;
Panel2: TPanel;
Image2: TImage;
SpinEdit3: TSpinEdit;
Label11: TLabel;

```

```

Label12: TLabel;
Justieren: TButton;
Messmodus1: TCheckBox;
Subtractbackground1: TCheckBox;
Huellkurve1: TCheckBox;
PeakDetection1: TCheckBox;
procedure QuitClick(Sender: TObject);
procedure MessenClick(Sender: TObject);
procedure FormCreate(Sender: TObject);
procedure JustierenClick(Sender: TObject);
procedure Timer1Timer(Sender: TObject);
procedure Messmodus1Click(Sender: TObject);
procedure PeakDetection1Click(Sender: TObject);
procedure SpinEdit2Change(Sender: TObject);
procedure Background1Click(Sender: TObject);
procedure SubtractBackground1Click(Sender: TObject);
procedure SpinEdit3Change(Sender: TObject);
procedure About1Click(Sender: TObject);
procedure QuickManual1Click(Sender: TObject);
procedure Huellkurve1Click(Sender: TObject);

private
  { Private-Deklarationen }
public
  { Public-Deklarationen }
end;

var
  ccdfm: Tccdfm;
  zaehler,ref : integer;
  max,max_pos,sum,mw_bg : integer;
  inbyte : byte;
  just_flag : boolean;
  max_temp,pos_temp,e,p_cnt : integer;

implementation

uses shortinf, globvar, adc_dac;

{$R *.DFM}

procedure outportb(adr:word;b:byte); { schreibt 8 bit -> CCD_Port }
begin
  asm
    mov dx,adr
    mov al,b
    out dx,al
  end
end;

function inportb(adr : word) : byte; { liest 8 bit von Port_adr }
var erg : byte;
begin
  asm
    mov dx,adr
    in al,dx
    mov erg,al
  end;
  inportb:=erg;
end;

```

```

procedure epp_inp;           { schaltet CCD_Port auf LESEN }
begin
  outportb(base_2+2,$24);
end;

procedure epp_outp;         { schaltet CCD_Port auf SCHREIBEN }
begin
  outportb(base_2+2,$04);
end;

function test_irq : boolean; { Testet IRQ_CCD_Port = EndOfScan ? }
begin
  epp_inp;
  test_irq:= (inportb(base_2+1) and 64) = 64;  { Bit 6 gesetzt? }
end;

procedure set_dig_out(io:byte);

begin

end;

procedure Tccdfrm.QuitClick(Sender: TObject); { Programm beenden }
begin
  messagebeep(0);
  close
end;

procedure Tccdfrm.MessenClick(Sender: TObject); { CCD_Messung starten }
var i,r_pos : integer;
    r_amp : byte;
    p_farbe,b_farbe : Tcolor;
    dummy : char;
begin
  if messmodus1.Checked then
  begin
    for i:=0 to 127 do dat2[i]:=random(16)+3;
    r_pos:=random(5)+64;
    r_amp:=random(5)+100;
    for i:=r_pos-5 to r_pos+5 do dat2[i]:=r_amp;
  end
  else
  begin
    // scan TSL 215, get Data
    scan_128_3;
  end; // else
  if subtractbackground1.Checked then
    for i:=0 to 102 do if bgnd_3[i]<=dat2[i] then dat2[i]:=dat2[i]-bgnd_3[i]
                      else dat2[i]:=0;
  if hue11kurve1.checked then          { Screen Display inverse }
  begin
    p_farbe:=clyellow;
    b_farbe:=clblack;
  end
  else
  begin
    { Screen Display normal }
    p_farbe:=clblack;
    b_farbe:=clwhite
  end; { if }
  with image1.canvas do

```

```

begin
  brush.color:=b_farbe;
  pen.color:=b_farbe;
  rectangle(0,0,image1.width,image1.height);
  pen.color:=p_farbe;
  for i:=0 to 127 do
    if i mod 4 = 0 then          { X-Skalierung }
      if huellkurve1.checked then  { Hüllkurvendarstellung }
        begin
          moveto(i div 4,256);
          lineto(i div 4,256-dat2[i]);
        end
      else                        { Punktedarstellung }
        pixels[i div 4,256-dat2[i]]:=pen.color ;
      end;
  end; { with image1.canvas .. }

begin { Max-Suche, Flanken- und background- Detektion }
  max:=0;max_pos:=0;sum:=0;
  for i:=0 to 127 do if dat2[i]>max then begin { finde Peak-Maximum }
    max:=dat2[i];
    max_pos:=i;
  end; { if }

end; { calculate }
if peakdetection1.Checked and (max>=ref) then
begin
  if p_cnt=0 then
  begin // Wenn Peakamplitude und Peakposition
    max_temp:=max; // in 5 aufeinanderfolgenden Scans
    pos_temp:=max_pos; // innerhalb der Grenzen von e (Epsilon)
    p_cnt:=1; // liegen, dann ist Teilchenlage stabil !!
  end;
  if p_cnt>0 then
  begin
    if (max_temp>=max-e)and(max_temp<=max+e)and(p_cnt<5)and
      (pos_temp>=max_pos-e)and(pos_temp<=max_pos+e) then inc(p_cnt);

    if p_cnt = 5 then // Stabilitätskriterium erfüllt !!!
    begin
      //set_dig_out(255); // I/O-Pin setzen
      panel2.visible:=true;
      justierenclick(self); // schaltet Timer aus
      //p_cnt:=0;
      close; // CCD_Window schliessen !!
    end;
  end;
  else p_cnt:=0;
end; { Messen }

procedure Tccdfm.FormCreate(Sender: TObject); { Program_Inits }
var c : integer;
begin
  p_cnt:=0; // Peakdetection Counter
  e:=10; // Toleranzwert Epsilon
  just_flag:=false;
  with image1.canvas do
  begin
    brush.color:=clwhite;
    pen.color:=clwhite;
    rectangle(0,0,image1.width,image1.height);

```

```

    pen.color:=clblack;
end; { with ima... }
end; { Formcreate }

procedure Tccdfrm.JustierenClick(Sender: TObject);      { Justagemode/Timer }
begin
    messagebeep(0);
    if p_cnt<5 then panel2.Visible:=false;
    just_flag:=not just_flag;
    if just_flag then
        begin
            timer1.enabled:=true;
            justieren.caption:='STOP';
        end
    else
        begin
            timer1.enabled:=false;
            justieren.caption:='START';
        end
    end;

procedure Tccdfrm.Timer1Timer(Sender: TObject);
begin
    messenckick(self);
end;

procedure Tccdfrm.Messmodus1Click(Sender: TObject);
begin
    messmodus1.Checked:=not messmodus1.Checked;
end;

procedure Tccdfrm.PeakDetection1Click(Sender: TObject);
begin
    peakdetection1.Checked:=not peakdetection1.Checked;
end;

procedure Tccdfrm.SpinEdit2Change(Sender: TObject);
var c : integer;
begin
    val(spinedit2.text,e,c); // Toleranzgrenze Epsilon
end;

procedure Tccdfrm.Background1Click(Sender: TObject);
var i : integer;
    dummy : char;
begin
    if not messmodus1.Checked then
        begin
            for i:= 0 to 127 do bgnd_3[i]:=random(16)+64;
            end
        else scan_128_3;

    with image2.Canvas do
        begin
            rectangle(0,0,image2.Width,image2.Height);
            for i:=0 to 127 do
                if (i mod 16) = 0 then pixels[i div 16,64-(bgnd_3[i]div 4)]:= clblue;
            end;
        end;
end;

procedure Tccdfrm.SubtractBackground1Click(Sender: TObject);

```

```

begin
  subtractbackground1.Checked:=not subtractbackground1.Checked;
end;

procedure Tccdfrm.SpinEdit3Change(Sender: TObject);
var c : integer;
begin
  val(spinedit3.Text,ref,c);
end;

procedure Tccdfrm.About1Click(Sender: TObject);
begin
  showmessage('Mess- und Steuersoftware CCD_Particle_Detection'+#13+
    'für Labor 5, AK Prof. Kiefer / Dr. Popp / Jan. 2002'+#13+
    '(co) Jürgen Zimmermann / DV-Systemtechnik / PC');
end;

procedure Tccdfrm.QuickManual1Click(Sender: TObject);
begin
  Shortinfos.memo1.lines.loadfromfile('manual.txt');
  Shortinfos.show;
end;

procedure Tccdfrm.Huellkurve1Click(Sender: TObject);
begin
  huellkurve1.checked:=not huellkurve1.checked;
end;

end.

unit Globvar; { enthält alle globalen Variablen, Konstanten und }
              { Typvereinbarungen für Elasto - Messprogramm(e) }
              { (co) zim/eck PC/EL last date : 16.4.98 }
interface

var
  f_name : string;           { aktueller Dateiname }
  datei,datei1,datei2 : textfile; { seq. Messfiles }
  adw1,adw2,adw3,adw4 : integer; { ADC-Messwert-Variablen }
  bgnd : array[0..127] of byte; { Datenarray Background TSL_215 }
  bgnd_2 : array[0..127] of byte; { Datenarray Background TSL_215_2 }
  bgnd_3 : array[0..127] of byte; { Datenarray Background TSL_215_3 }
  x_dat : array[1..2000] of real; { Datenarray x-Werte (fs oder nm) }
  y_dat : array[1..2000] of integer; { Datenarray y-Werte }
  s_3903 : array[0..204] of integer; { Datenarray Fotodiodenarray S_3903 }
  dat : array[0..127] of byte; { Datenarray TSL_215, 128 Pixel Hor. }
  dat1 : array[0..127] of byte; { Datenarray TSL_215, 128 Pixel Ver. }
  dat2 : array[0..127] of byte; { Datenarray TSL_215, 128 Pixel Peak }
  liste : array[0..127] of byte;
  t_bel : word; { Belichtungszeit in sec für " " }
  t_ref : word; { Messintervall Feuchte/Temp. in sec }
  t_da : word; { Messintervall FD_Array in sec }
  p1,p2,pm,m,m2,p_diff,p1_h,df, { Peakpositionen Integralbereich V }
  p2_h,pm_h,m_h,p_diff_h : integer; { Peakpositionen Integralbereich H }
  cf : integer; { CTRL - Faktor }
  level : integer; { Diskriminatorschwelle Peakdetektoren }
  proz : integer; { proz. Teiler für U_dac }
  cnt,cnt_h : integer; { Peak Counter V + H }
  hwb,hwb_h : integer; { Halbwertsbreiten Single Peak }

```



```

hb_h,hb_v : byte;           { Kriterium Halbwertsbreite }
mw_d_array : word;         { Signalmittelwert aller Arraydioden }
n_mess : integer;         { Anzahl der verfahrenen Messpunkte }
sum_1,sum_2,              { temp. sum-var. für Akkumulationen }
sum_3,sum_4 : longint;
step : integer;
ro_time : word;
x_anf,x_end : integer;     { Anf./Endwerte x-Achse }
y_bereich : integer;      { y-Bereich }
y_fakt : real;             { y-Skalierungsfaktor }
akt_y : integer;          { Übergabevariable GrafMod }
TestFlag : boolean;       { Prüfflag für Testmodus }
rs_error : boolean;       { Fehlerflag für ComPorts }
save_flag : boolean;      { Prüfflag für Dateispeicherung }
breakflag : boolean;
ref_flag : boolean;
smoothflag : boolean;
end_flag : boolean;
flag_u : boolean;         { Toggleflag Polaritätswechsel U_out }
r,x,y,w : integer;
ac,dc1,dc2,freq : byte;   { Fallenparameter }
da_wert1,da_wert3 : byte;
max,maxpos : byte;        { Peakmax., Max.Position }
mp_alt,mp_alt1 : byte;    { Merker für 1. Peakmaximumposition }
s,s_h : byte;             { untere Schranke Peakdetektion V,H }
sweep_uq,sweep_ac : boolean;
start_flag : boolean;
u_quad_a,u_quad_e,
delta_uq,uq_fin,ac_fin : byte;
u_ret : integer;
d_fakt : real;
number_of_scans,nos_2 : cardinal;
max2 : integer;
mpos2 : integer;
num,num1 : byte;
pmax,pmaxpos : integer;
pmax1,pmax2 : integer;
lg1,rg1,lg,rg : byte;
pnum,pnum1 : byte;
osc_flag : boolean;
osc_cnr : byte;
dec_dc_flag,dec_ac_flag : boolean;
inc_dc_flag,inc_ac_flag : boolean;
dt_1,dt_2 : word; // div. Delay(s) in ms für die Ablaufsteuerung
const
  neudatei = 'neu_mess';
  pi = 3.1424;
  Mp_max = 2000; { Maximale Messpunktzahl }
  Delta_y = 100; { y-Bereich in Pixel }
  Adc_range = 4096; { ADC - Bereich unipolar (pos.) }
  x_vers = 250; { x-Achsenversatz für Grafikfenster }
  // base = 768; { Basisadresse ACL8112-LabKarte HEX 300 }
  base_1 = $0300; { ADCDAC-ISA_1 }
  base_2 = $0320; { ADCDAC-ISA_2 }

  procedure outportb(adr:word;b:byte);
  function inportb(adr : word) : byte;

implementation

procedure outportb(adr:word;b:byte); { schreibt 8 bit -> CCD_Port }

```

```

begin
  asm
    mov dx,adr
    mov al,b
    out dx,al
  end
end;

function inportb(adr : word) : byte; { liest 8 bit von Port_adr }
var erg : byte;
begin
  asm
    mov dx,adr
    in al,dx
    mov erg,al
  end;
  inportb:=erg;
end;

end.
unit Adc_dac; // Proc. and Functions for DAQ-Cards and Detector Handling
              // ADC, DAC, Timer/Counter - Handling

interface

// procedure getad(chan:byte);
procedure set_ctr2;
procedure start_ctr1_2(lbyte,hbyte:byte);
function get_ctr1:boolean;
procedure dac_pcl(dawert:integer);
// procedure d_array;
// procedure tsl_215(acc:integer);
// procedure tsl_1302(acc:integer);
procedure scan_128;
procedure scan_128_2;
procedure scan_128_3;
procedure dac_1(w : byte);
procedure dac_2(w : byte);
procedure dac_3(w : byte);
procedure dac_4(w : byte);
function adc1(k:byte):byte;
function adc2(k:byte):byte;
procedure warte(n:integer);
procedure verz_nop(n:word);

const base = 768;

implementation

uses globvar;

procedure warte(n:integer);
var lb,hb:byte;
begin
  lb:=n mod 256;
  hb:=n div 256;
  set_ctr2;
  start_ctr1_2(lb,hb);
  repeat
  until get_ctr1;

```

```

end;

procedure verz_nop(n:word);
var i:word;
begin
  for i:=1 to n do asm
    nop
  end; // asm
end;

procedure scan_128; { Messroutine Linear Sensor Array TSL215 }

var d_index,i,dummy : integer; { Testversion vom 5.7.2002 (co) zi/IPC }
    ii,j,k : integer;
    sum : longint;
    si_flag : boolean;
    diff_12 : integer;

    { Kanal 0 = Analogwert }
    { " 1 = SI }
    { " 2 = CLK }

begin
  asm cli end;
  sum:=0;

  { Array auslesen }
  repeat
    verz_nop(5);          { 50 nop-Zyklen warten }
  until adc1(1)>128;      { Warten auf SI - Signal = High }

  repeat
    verz_nop(5);          { 50 nop-Zyklen warten }
  until adc1(1)<128;      { Warten auf SI = LOW }

  for d_index:=1 to 128 do
  begin
    repeat
      verz_nop(5);          { 50 nop-Zyklen warten }
    until adc1(1)<128;      { Warten auf CLK = LOW }

    repeat
      verz_nop(5);          { 50 nop-Zyklen warten }
    until adc1(2)>128;      { Warten auf CLK = High }
    verz_nop(10);
    dat[d_index-1]:= adc1(0); { Diodenwert ins Array }

  end; { for d_index }

  for i:=63 to 127 do dat[i]:=round(dat[i]*0.85);

  asm sti end;
end; { scan_128 }

procedure scan_128_2; { Messroutine Linear Sensor Array TSL215 }

var d_index,i,dummy : integer; { Testversion vom 5.7.2002 (co) zi/IPC }

```

```

ii,j,k : integer;
sum : longint;
si_flag : boolean;
diff_12 : integer;

{ Kanal 0 = Analogwert }
{ " 1 = SI }
{ " 2 = CLK }

begin
asm cli end;
sum:=0;

{ Array auslesen }
repeat
verz_nop(5);          { 50 nop-Zyklen warten }
until adc2(1)>128;    { Warten auf SI - Signal = High }

repeat
verz_nop(5);          { 50 nop-Zyklen warten }
until adc2(1)<128;    { Warten auf SI = LOW }

for d_index:=1 to 128 do
begin
repeat
verz_nop(5);          { 50 nop-Zyklen warten }
until adc2(1)<128;    { Warten auf CLK = LOW }

repeat
verz_nop(5);          { 50 nop-Zyklen warten }
until adc2(2)>128;    { Warten auf CLK = High }
verz_nop(10);
dat1[d_index-1]:= adc2(0);  { Diodenwert ins Array }

end; { for d_index }

asm sti end;
end; { scan_128_2 }

procedure scan_128_3; { Modul Linear Sensor Array TSL215 for Peakdetection }

var d_index,i,dummy : integer; { Testversion vom 19.03.03 (co) zim/IPC }
ii,j,k : integer;
sum : longint;
si_flag : boolean;
diff_12 : integer;

{ Kanal 4 = Analogwert }
{ " 5 = SI }
{ " 6 = CLK }

begin
asm cli end;
sum:=0;

{ Array auslesen }
repeat
verz_nop(5);          { 50 nop-Zyklen warten }

```

```

until adc2(5)>128;          { Warten auf SI - Signal = High }

repeat
  verz_nop(5);             { 50 nop-Zyklen warten }
until adc2(5)<128;         { Warten auf SI = LOW }

for d_index:=1 to 128 do
begin
  repeat
    verz_nop(5);           { 50 nop-Zyklen warten }
    until adc2(6)<128;      { Warten auf CLK = LOW }

    repeat
      verz_nop(5);         { 50 nop-Zyklen warten }
      until adc2(6)>128;    { Warten auf CLK = High }
      verz_nop(10);
      dat2[d_index-1]:= adc2(4);  { Diodenwert ins Array }

    end; { for d_index }

  asm sti end;
end; { scan_128_3 }

procedure set_ctr2;

begin
  outputb(base+3,$b4);     { Counter 2 auf Pacermode 10110100 }
  outputb(base+2,208);     { Lowbyte mit dez. 208... }
  outputb(base+2,7);       { Highbyte mit 7 laden }
end; {set_ctr2}           { ergibt Teiler 2000 -> 1 ms }

procedure start_ctr1_2(lbyte,hbyte:byte); { PCL-Timer laden u. starten }

const ctl = $78;          { Timermodus 4 Software-Trigger }
begin
  outputb(base+3,ctl);     { Counter 1 auf Mode 4 setzen 01111000 }
  outputb(base+1,lbyte);   { Lowbyte laden }
  outputb(base+1,hbyte);   { Highbyte laden u. Timer starten ! }
end; {start_ctr1}

function get_ctr1 : boolean; { PCL-Timer-Abfrage auf Terminal-Stop }

var l_byte,h_byte : byte;

begin
  l_byte:=inportb(base+1); { Lowbyte Counter 1 lesen }
  h_byte:=inportb(base+1); { Highbyte Counter 1 lesen }
  if (l_byte=0) and (h_byte=0) then { Falls beide = 0 ... }
    get_ctr1:=true          { dann Ergebnis = WAHR ... }
  else
    get_ctr1:=false;        { sonst }
  end; {get_ctr1}

procedure dac_pcl(dawert:integer); { Analogausgabe PCL711 - Board }

var lowbyte,highbyte : byte;

begin

```

```

if dawert < 0 then dawert:=0;      { negative Werte unterbinden }
highbyte:= dawert div 256;      { Zerlegen des Ausgabewertes }
lowbyte := dawert mod 256;      { in High- und Lowbyte }
outportb(base + 4,lowbyte);     { und auf DAC-Port }
outportb(base + 5,highbyte);    { ausgeben . }
end; {dac_pcl}

```

```

procedure dac_1(w : byte); { w -> Karte_1 DAC_0 }
begin
  outportb(base_1+6,0);      { Bereich 0..2,5V }
  outportb(base_1+0,w);     { DAC_Out }
end;

```

```

procedure dac_2(w : byte); { w -> Karte_1 DAC_1 }
begin
  outportb(base_1+6,0);      { Bereich 0..2,5V }
  outportb(base_1+1,w);     { DAC_Out }
end;

```

```

procedure dac_3(w : byte); { w -> Karte_2 DAC_0 }
begin
  outportb(base_2+6,0);      { Bereich 0..2,5V }
  outportb(base_2+2,w);     { DAC_Out }
end;

```

```

procedure dac_4(w : byte); { w -> Karte_2 DAC_1 }
begin
  outportb(base_2+6,0);      { Bereich 0..2,5V }
  outportb(base_2+3,w);     { DAC_Out }
end;

```

```

function adc1(k:byte):byte; { k = ADC-Kanal 0..7 , Karte_1 }
var dummy : byte;
begin
  outportb(base_1+4,k);
  dummy:=inportb(base_1+4);
  verz_nop(10);
  adc1:=inportb(base_1+0);
end;

```

```

function adc2(k:byte):byte; { k = ADC-Kanal 0..7, Karte_2 }
var dummy : byte;
begin
  outportb(base_2+4,k);
  dummy:=inportb(base_2+4);
  verz_nop(10);
  adc2:=inportb(base_2+0);
end;

```

end.

unit shortinf;

interface

uses

Windows, Messages, SysUtils, Classes, Graphics, Controls, Forms,
Dialogs, StdCtrls;

```
type
  TShortinfos = class(TForm)
    Memo1: TMemo;
    Button1: TButton;
    procedure Button1Click(Sender: TObject);
  private
    { Private declarations }
  public
    { Public declarations }
  end;

var
  Shortinfos: TShortinfos;

implementation

{$R *.dfm}

procedure TShortinfos.Button1Click(Sender: TObject);
begin
  close
end;

end.
```


References

- (1) W. Hinds, *Aerosol Technology: Properties, behaviour and Measurement of Airborne Particles* (2nd edn.), John Wiley & Sons, New York, 1999.
- (2) J. H. Seinfeld and S. N. Pandis, *Atmospheric Chemistry and Physics: From Air Pollution to Climate Change*, John Wiley & Sons, New York, 1998.
- (3) C. A. P. Zevenhoven, *Particle Charging and Granular Bed Filtration for High Temperature Application*, Delf University Press, 1992.
- (4) R. B. Bird, W. E. Stewart, E. N. Lightfoot, *Transport Phenomena*, Chapter 3, 4 and 5, John Wiley, New York, 1960.
- (5) L. Landau, E. Lifshitz, *Fluid Mechanics*, Pergamon, London, 1959.
- (6) J. Happel, H. Brenner, *Low Reynolds number hydrodynamics*, Martinus Nijhoff Publ., 4th printing, 1986.
- (7) G. I. Surovtsova, V. I. Turubarov, , English translation in *J. Colloid USSR*, **48**(5) (1987) 962.
- (8) C. W. Oseen, *Hydrodynamic*, **82** (1927) 21.
- (9) J. Boussinesq, *C. R. Acad. Sci. Paris*, **100** (1885) 935.
- (10) A. B. Basset, *Phil. Trans. R. Soc. Lond.*, **179 A** (1888) 43.
- (11) C.-M. Tchen, *Mean value and correlation problems connected with the motion of small particles suspended in a turbulent fluid*, Delf Univ. of Technology, 1947.
- (12) M. R. Maxey, J. J. Riley, *Phys. Fluids*, **26** (1983) 883.
- (13) N. A. Fuchs, *The mechanics of aerosols*, Macmillan, New York, 1964.
- (14) S. Holler, S. Arnold, N. Wotherspoon, A. Korn, *Rev. Sci. Instrum.*, **66** (1995) 4389.
- (15) P. A. Lawless, *J. Aerosol Sci.*, **27** (1996) 191.
- (16) H. J. White, *Industrial Electrostatic Precipitation*, Addison-Wesley, Reading, MA, 1963.
- (17) S. Masuda, M. Washizu, A. Mizuno, K. Akutsu, *Proc. IEEE/IAS*, Toronto, Canada, (1978) 16.
- (18) C. A. P. Zevenhoven, R. D. J. Wierenga, B. Scarlett, H. Yamamoto, *J. Electrostat.*, **32** (1994) 133.

- (19) A. Jaworek, A. Krupa, *J. Electostat.*, **23** (1989) 361.
- (20) H. H. Pauthenier, M. Moreau-Hanot, *J. Phys. Radium*, (1932) 3.
- (21) M. Lackowski, *J. Electrostat.*, **51-52** (2001) 225.
- (22) J. Chiseki and T. Manabu, *J. Imaging Sci. Technol.*, **40**(5) (1996) 436.
- (23) R. C. Brown, *J. Aerosol Sci.*, **28**(8) (1997) 1373.
- (24) A.P. Weber, L. Xu and G. Kasper, *J. Aerosol Sci.*, **31** 1 (2000) 1015.
- (25) J. B. Gajewski, *J. Electrostat.*, **15** (1984) 81.
- (26) P. H. W. Vencoulen, J. C. M. Morijnissen, B. Scarlett, *J. Aerosol Sci.*, **26** (1995) 797.
- (27) H. Umhauer, *J. Aerosol Sci.*, **14**(6) (1983) 175
- (28) A. Ashkin, *Appl. Phys. Lett.*, **24**(4) (1970) 156.
- (29) A. Ashkin, J. M. Dziedzic, *Appl. Phys. Lett.*, **24** (1974) 586.
- (30) W. Kiefer, *Microbeam Analysis*, San Francisco Press Inc., San Francisco (1987) 137.
- (31) W. Kiefer, *Croatica Chemica Acta*, **61** (1987) 473.
- (32) E. J. Davis, *Aerosol Sci. and Technol.*, **2** (1987) 121.
- (33) E. J. Davis, *Surf. And Coll. Sci.*, **14** (1987) 1.
- (34) E. J. Davis, *Langmuir*, **1** (1985) 379.
- (35) H. Fletcher, *Phys. Rev.*, **4** (1914) 440.
- (36) F. T. Gucker, J. J. Egan, *J. Colloid Interface Sci.*, **16** (1961) 68.
- (37) P. J. Wyatt, D. T. Philips, *J. Colloid Interface Sci.*, **39** (1972) 125.
- (38) E. J. Davis, A. K. Ray, *J. Colloid Interface Sci.*, **75** (1980) 566.
- (39) E. J. Davis, A. K. Ray, *J. Phys. Chem.*, **67** (1977) 414.
- (40) W. Paul, M. Raether, *Z. Phys.*, **142** (1955) 262.
- (41) W. Paul, O. Osberghaus, E. Fischer, *Forschungsber. Nr. 415* (1958).
- (42) R. F. Wuerker, H. Shelton, R. V. Langmuir, *J. Appl. Phys.*, **30** (1959) 342.
- (43) H. Straubel, *Z. Aerosolforschung und Therapie*, **4** (1955) 385.
- (44) H. Straubel, *Z. Elektrochem.*, **60** (1956) 1033.
- (45) E. Straubel, H. Straubel, *J. Aerosol Sci.*, **13** (1982) 220.
- (46) E. Straubel, H. Straubel, *J. Aerosol Sci.*, **15** (1984) 301.
- (47) T. G. O. Berg, T. A. Gaucker, *Am. J. of Phys.*, **37**(10) (1969) 1013.
- (48) H. H. Blau, D. J. McCleese, D. Watson, *Appl. Opt.*, **9** (1970) 2522.

- (49) E. J. Davis, E. Chorbajian, *Ind. Eng. Chem. Fundam.*, **13** (1974) 272.
- (50) G. O. Rubel, *J. Colloid Interface Sci.*, **81** (1981) 188.
- (51) G. O. Rubel, J. W. Gentry, *J. Aerosol Sci.*, **15** (1984) 661.
- (52) T. L. Ward, Ph. D. Thesis, University of Washington, Seattle (1989).
- (53) S. Arnold, L. M. Follan, *Rev. Sci. Instrum.*, **58**(9) (1987) 1732.
- (54) A. K. Ray, B. Devakottai, A. Souyri, J. L. Huckaby, *Langmuir*, **7** (1991) 525.
- (55) P. H. Dawson, *Quadrupole Mass Spectrometry and Its Applications*, New York: American Institute of Physics, 1995.
- (56) R. March, R. Hughes, *Quadrupole Storage Mass Spectrometry*, John Wiley & Sons, New York, 1989.
- (57) M. Abramowitz, I. A. Stegun, Ch. 21 in *Handbook of Mathematical Functions with Formulas, Graphs, and mathematical Tables*, 9th Ed., New York: Dover (1972) 751.
- (58) J. Meixner, F. W. Schäfke, *Mathieusche Funktionen und Sphäroidfunktionen*, Berlin: Springer-Verlag, 1954.
- (59) G. Mie, *Ann. Phys.*, **25** (1908) 377.
- (60) M. Kerker, *The scattering of light and other electromagnetic radiation*, Ac. Press Inc., Florida, 1969.
- (61) M. Born and E. Wolf, *Principles of Optics: Electromagnetic Theory of Propagation, Interference and Diffraction of Light*, 6th ed., Pergamon Press, New York, 1980.
- (62) A. Smekal, *Naturwissenschaften*, **11** (1923) 873.
- (63) C. V. Raman, *Indian J. Phys.*, **2** (1928) 387.
- (64) C. V. Raman, K. S. Krishnan, *Nature*, **121** (1928) 501.
- (65) G. Landsberg, L. Mandelstam, *Naturwiss.*, **15** (1928) 772.
- (66) I. R. Lewis, H. G. M. Edwards, *Handbook of Raman Spectroscopy*, Marcel Dekker Inc., New York (2001).
- (67) M. D. Morris, ch. 6 in *Applied Laser Spectroscopy*, VCH Publications Inc., New York (1992) 227.
- (68) J. Popp, W. Kiefer, *Fundamentals of Raman Spectroscopy, Encyclopedia of Analytical Chemistry*, Wiley, New York (in press).
- (69) G. Schweiger, *J. Aerosol Sci.*, **21**(4) (1990) 483.

- (70) M. F. Buehler, *Raman Spectroscopy of Levitated Microparticles*, PhD Thesis, Univ. of Washington, Washington, 1991.
- (71) A. H. Lefebvre, *Atomization and Sprays*, Taylor Francis, New York, 1989.
- (72) L. P. Bayvel, Z. Orzechowski, *Liquid Atomization*, Taylor Francis, Washington DC, 1993.
- (73) Topas GmbH, *Atomizer Aerosol Generator ATM 220*, Instruction Manual, Dresden, 1999.
- (74) Y.-S. Cheng, B. T. Chen, Aerosol Sampler Calibration, in *Air Sampling Instruments*, 5th ed., ACGIH, Cincinnati, 1995.
- (75) W. K. Murphy, S. W. Sears, S. W., *J. Appl. Phys.*, **85** (1964) 1986.
- (76) W. D. Davis, *Environ. Sci. Technol.*, **11** (1977) 587.
- (77) J. T. Jayne, L. D. Leard, X. Zhang, P. Davidovits, K. A. Smith, C. E. Kolb, D. R. Wornsnop, *Aerosol Sci. Tech.*, **33** (2000) 49.
- (78) P. Liu, P. J. Ziemann, D. B. Kittelson, P. H. McMurry, *Aerosol Sci. and Tech.*, **22** (1995) 293.
- (79) M. F. Hamilton, D. T. Blackstock, *Nonlinear Acoustic*, Acad. Press, 1998.
- (80) R. E. Apfel, W. T. Shi, *J. Acoustic Soc. Am.*, **99** (1996) 1977.
- (81) J. M. Anderson, R. S. Budwig, K. S. Line, J. G. Frankel, *Use of Acoustic Radiation Pressure to Concentrate Small Particles in an air Flow*, IEEE Ultrasonics Symposium, 2002.
- (82) G. Kaduchak, D. N. Sinha, *Cylindrical Acoustic Levitator / Concentrator*, US 6 467 350, The Regent Univ. of California, Los Alamos, 2002.
- (83) N. G. Bernigau, R. M. Vanck, *Einrichtung zur messung von Aerosolparametern*. DE 40 08 348, Int. Cl. G01N15/10. Deutsches Patentamt, München, 1991.
- (84) U. Sievert, *Entwicklung eines unipolaren Aerosolaufladers mit hoher Dynamik zur Bestimmung der Partikelgrößenverteilung am strömenden Aerosol*, Dissertation, Gesamthochschule Duisburg (1998).
- (85) P. Büscher, *Entwicklung und Modellierung eines unipolaren Diffusions- und Feldaufladers für Partikel in Aerosolen*, Dissertation, Gesamthochschule Duisburg (1995).
- (86) P. Büscher, A. Schmidt-Ott, *J. Aerosol Sci.*, **23**(1) (1992) 5385.

- (87) P. Büscher, A. Schmidt-Ott, *J. Aerosol Sci.*, **21**(1) (1990) 567.
- (88) B. Y. U. Liu, D. Y. H. Pui, *J. Aerosol Sci.*, **6** (1975) 249.
- (89) G. K. Batchelor *An Introduction to Fluid Dynamics*, Cambridge Univ. Press, Cambridge, 1967.
- (90) C. A. P. Zevenhoven, *J. Electrostat.*, **46** (1999) 1.
- (91) G. W. Penny, R. D. Lynch, *AIEE Trans. Pt. 1 Communication and Electronics*, **9** (1957) 249.
- (92) K. Adamiak, A. Krupa, A. Jaworek, *Institution of Physics Conference Series*, New York, No. **143** (1995) 275.
- (93) K. Adamiak, *IEEE Industrial Application Society*, Annual Conference, Denver, (1994) 1527.
- (94) M. Lackowski, *J. Electrostatics*, **51-52** (2001) 225.
- (95) H. Singer, H. Steinbigler H., P. Weiss, *IEEE PES*, Winter Meeting, New York, 1974.
- (96) C. S. Sloane, A. A. Elmoursi, *IEEE Industry Applications Meeting*, Part. **II** (1987) 1568.
- (97) E. J. Davis, *J. Surf. And Coll. Sci.*, **14** (1985) 1.
- (98) S. K. Loyalka, P. Tekasakul, R. V. Tompson, R. C. Wander, *J. Aerosol Sci.*, **26** (1995) 445.
- (99) Müller von A., *Ann. der Physik*, **6** (1960) 206.
- (100) E. J. Davis, M. F. Buehler, T. L. Ward, *Rev. Sci. Instrum.*, **61** (1990) 1281.
- (101) W. H. Hartung, C. T. Avedisian, *Proc. R. Soc. London*, **437 A** (1992) 237.
- (102) E. J. Davis, M. A. Bridges, *J. Aerosol Sci.*, **25** (1994) 1179.
- (103) R. B. Lebedev, I. P. Skal'Skaya, Ya. S. Uflyand, *Problems in Mathematical Physics*, Pergamon Press, Oxford, 1966.
- (104) J. A. Richards, *SIAM J. Appl. Math.*, **30** (1976) 240.
- (105) N. W. McLachlan, *Theory and Applications of the Mathieu Functions*, Oxford Press, London, 1959.
- (106) A. Gunderson, *SIAM J. Appl. Math.*, **26** (1976) 345.
- (107) C. Taylor, N. Narendra, *SIAM J. Appl. Math.*, **17** (1969) 343.

- (108) R. H. Frickel, R. E. Shaffer, J. B. Stamatoff, *Chambers for the Electrodynamic Containment of Charged Aerosol Particles*, Report No. ARCSL-TR-77041, Chemical System Laboratory, Maryland, 1978.
- (109) M. Fang, K. Wang, *Phys. Lett.*, **197 A** (1995) 135.
- (110) E. Mathieu, *J. Math. Pure Appl.*, **13** (1868) 137.
- (111) P. H. Dawson, *Quadrupole Mass Spectrometry and Its Applications*, Elsevier, Amsterdam, 1979.
- (112) R. H. March, *J. Mass Spec.*, **32** (1997) 351.
- (113) N. Lermer, M. D. Barnes, C.-Y. Kung, W. B. Whitten, J. M. Ramsey, *Anal. Chem.*, **69** (1997) 2215.
- (114) D. Gerlich, *Inhomogeneous RF fields: A Versatile Tool for the Study of Processes with Slow Ions*, PhD Thesis, Univ. Freiburg (1992).
- (115) P. H. Dawson, *Quadrupole Mass Spectrometry*, Elsevier, Amsterdam, 1976.
- (116) P. E. Miller, M. B. Denton, *J. Mass Spectrom. Ion Processes*, **72** (1986) 223.
- (117) J. H. Seinfeld, S. N. Pandis, *Atmospheric Chemistry and Physics: From Air Pollution to Climate Change*, John Wiley & Sons, New York, 1998.
- (118) M. V. Johnson, *J. of Mass Spectrom.* **35** (2000) 585.
- (119) R. Thurn, W. Kiefer, *J. Raman Spectrosc.*, **15** (1984) 411.
- (120) R. Thurn and W. Kiefer, *Appl. Spectrosc.*, **38** (1984) 78.
- (121) C. J. H. Brenan, I. W. Hunter, *Appl. Spectrosc.*, **49** (1995) 1086.

Acknowledgements

This work involved the cooperation and assistance of many people that I would like to thank for their support.

I would like to thank Prof. Dr. Wolfgang Kiefer for providing me the chance to perform my thesis in his laboratories. The possibility to visit numerous international conferences, and to enlarge my physics knowledge provided an exciting environment for elaboration of my thesis.

I am very grateful to my advisor, Prof. Dr. Jürgen Popp, for his patient supervision through my PhD program. Not only that he always trust and encouraged me in doing research, but he also provided a crucial advice that helped me through "problems". We had fruitful discussions that held me on the right track. Without his help this thesis would not have been possible.

A special gratitude goes to Dr. Markus Lankers, Dr. Oliver Vallet, Dr. Peter Günther the business managers of the APSys company. Through their effort an extra financial support for developing my experiments was possible. I would also like to thank Dr. Michael Schmitt for his help regarding the correction of the thesis.

I would like to thank Wolfgang Liebler, Thomas Schreckling, Ralf Kohrmann, Peter Lang and Gerhard Bömmel in the mechanic workshop, and Rainer Eck and Jürgen Zimmerman in the electronics workshop for their excellent technical support. The high quality equipment built under their attention helped me in the realization of my purposes.

I also thank my ex-colleagues Dr. Monica Bolboaca, Dr. Lucian Baia, Dr. Victor Roman and Dr. Oliver Sbanski for several professional and personal discussions. I will not forget the night work sheared with Joachim Koster in the beginning of this work. I am grateful to Nicu Tarcea for sharing his vast skills in computers and technology with me.

I thank my parents and my brother for their everlasting encouragement and support.

In closing, I would like to thank my wife Cristina and my son Daniel, their support can not be expressed in words.

Lebenslauf

Zur Person

Claudiu Dorin Dem
Diplom Physiker
geboren am 8.09.1975 in Oradea, Rumänien
rumänische Staatsbürgerschaft
verheiratet, 1 Kind

Studium

- Seit 10/1999 Promotionsstudium am Institut für Physikalische Chemie II der Universität Würzburg bei Prof. Dr. W. Kiefer
Thema: „Design and Construction of a Device for Light Scattering Studies on Airborne Particles”
- 10/1998-06/1999 Studium der Physik (Master of Science) an der Universität Babes-Bolyai, Cluj-Napoca, Rumänien
Titel der Arbeit: „Raman Untersuchungen an Boron-Vanadium Gläsern“
Abschluß: Diplom - Master of Science
- 10/1993-06/1998 Studium Technische Physik und Lehramt Physik an der Universität Babes-Bolyai, Cluj-Napoca, Rumänien
Titel der Diplomarbeit: „Charakterisierung auf eine CCP-RF Plasma mit kleiner Leistung“
Abschluß: Diplom

Schule

- 09/1989-06/1993 Lyzeum für Eisenbahn in Oradea, Rumänien
Ausbildung als Techniker für dieselelektrische Lokomotiven
Abschluss: Abitur

Berufstätigkeit

- seit 01/2000 Wissenschaftlicher Mitarbeiter an der Universität Würzburg
10/1999-12/1999 Wissenschaftliche Hilfskraft an der Universität Würzburg
09/1998-01/1999 Physiklehrer in Oradea